Revista ALCONPAT

Message from the Editor in Chief

JOURNAL OF THE LATIN-AMERICAN ASSOCIATION OF QUALITY CONTROL, PATHOLOGY AND RECOVERY OF CONSTRUCTION

http://www.revistaalconpat.org

With great satisfaction, we present the third issue of the tenth year of the ALCONPAT Journal.

The objective of the Journal is to publish contributions of basic and applied research directly associated with the solution of problems related with quality control, pathology and recovery of constructions being welcomed studio cases in these areas.

This edition of V10N3 starts with a work from **Mexico**, where Laura Vaca Arciga and colleagues show the use of silicon-based (NS) and functionalized (NF) nanoparticles as an emerging preventive surface treatment (ST) in reinforced concrete specimens. The specimens were manufactured with a water/cement (w/c) ratio of 0.65 and subjected to a previous aging period through exposure to CO_2. Subsequently, of the different variants of the treatment applied by spraying (using a dispersion of 0.1% of nanoparticles in water) and afterwards, the carbonation was added. The results of carbonation depth and contact angle indicate that there is an influence between the degree of aging and the efficiency of each treatment.

In the second work, from **Brazil**, Guido Lessa Ribeiro Filho and colleagues discuss the impact of varying the dry paint film thickness (DFT) on the underpaint corrosion of steel plates obtained from the floor of an offshore oil platform is evaluated. The specimens were all prepared using the same material and paint scheme, and the DFT and exposure conditions in a salt spray chamber were varied and compared with the results obtained in a real situation. The results indicated that corrosion initiated at sites where the paint was damaged, may be more important than corrosion through the undamaged paint due to permeation, even in cases where the DFT is thin. In specimens whose substrates were previously damaged, there were pathological manifestations of osmotic blistering. The underpaint corrosion that occurred after the paint was damaged in the field occurred at an intensity like that observed for the tested specimens.

In the third article, from **Brazil**, Emerson Felipe Felix and colleagues present the modeling and analysis of the corrosion effects due to carbonation on reinforced concrete elements through a numerical model based on the Finite Element Method. In order to minimize corrosion damage, tools are required to understand the pathological manifestation on the mechanical behavior of reinforced concrete. It was found that depending on the reinforcement corrosion stage, the state of stress and deformation of the concrete element is compromised. Besides, results show the efficiency of the developed model and its applicability to the simulation of the mechanical behavior of reinforced concrete structures subjected to uniform corrosion.

The fourth work, by Arnulfo Luévanos Rojas and his colleagues from **Mexico**, shows an analytical model for the design of corner combined footings subjected to an axial load and two orthogonal flexural moments by each column that takes into account the real pressure on the ground below of the footing, and the methodology is based on the principle that the integration of the shear force is the moment. The current design considers the maximum pressure at all contact points. This model is verified by equilibrium of shear forces, and moments. The application of the model is presented by means of a numerical example. Therefore, the proposed model is the most appropriate, because it generates better quality control in the resources used.

The fifth work in this edition was written by Ricardo Boni and Paulo Helene, from **Brazil**. This paper presents a case study about the challenges and good building practices involved in the execution of structural reinforced concrete pile caps over steel piles. The structural reinforcements were carried out in a project with 3 residential towers of approximately 30 floors each, located on the seafront. As a result, it was observed that mix design to define the type and characteristics of concrete, prototype event, particularities of the construction site, executive procedures employed, as well as the systematic monitoring and control of concreting events and other constructive stages was determinant to promote the safety and quality of reinforcement services in accordance with the assumptions and design requirements.

The sixth work, from **Bolivia** (Marina Pacara Copa and colleagues), discusses the time range to optimize and understand infrared thermography results when used on damage detection for flexible pavement. A monitoring activity was performed during 14 continuous hours (5:00 a.m. to 7:00 p.m.) for four study areas in a centrally located avenue in Cochabamba City, Bolivia. This activity evidenced an effective time range to take thermographic images from 11:00 a.m. to 4:00 p.m. Damage visualization by differential colorimetry in thermograms at different times was also verified. This test enables locating areas where a detailed inspection may be performed. As a limitation, its sensibility to changes under environmental conditions is evident.

In the seventh work, from Brazil, Wildson Wellington Silva and Eliana Cristina Barreto Monteiro identify the pathological manifestations and the strains of the air-conditioned apparatus of reinforced concrete in the buildings, given the large number of partial collapses in totals buildings. The data was collected by 3D software and consolidated on the ground. Of the 61 buildings analyzed, 48% are window type, which, in a situation of degradation and collapse, may fall to the ground with an impact of the order of tons. In coastal regions, accelerated effects of corrosion of reinforcements are increased, such as high humidity, contamination by motor vehicles and the marina region. It is concluded that these are not suitable for structures, which, together with the low quality and accelerating effects of corrosion of the armor, must not be able to recover.

The last article that closes this issue is written by Luciani Somensi Lorenzi and colleagues from Brazil. They say that the ABNT NBR 15575: 2013 tests are part of the knowledge of the civil construction sector, but the heat shock and thermal shock test is innovative and does not have a consolidated history. The purpose of this research is to make a critical analysis and present proposals. The results showed

that the experiment is quite inaccurate in the description of the procedure and equipment. Adjustments and innovations to provide more reliable results were provided. However, no proposals were made regarding visual inspection and the number of cycles. It is concluded that the lack of information on the test has direct responsibility for the results and that the suggested proposals have the potential to be incorporated.

In this issue, three articles were published because of their originality and contributions. They were distinguished at the CONPAT 2019 Congress with the awards A (Pathology of construction) and B (Repair of construction), which were featured in the work of Laura Vaca et al (Mexico), Ricardo Boni and Paulo Helene (Brazil), and Mariana Pacara et al (Bolivia). These papers have undergone additional evaluation by the Revista Alconpat, a process coordinated by the Co-Editor in Chief of the RA (Dr. Francisco Alonso Farrera).

We are confident that the articles in this issue will constitute an important reference for those readers involved with questions related with science and technology of concrete. We thank the authors for participating in this issue, and for their willingness and effort to present high quality articles and meet the established timelines.

On behalf of the Editorial Board

Pedro Castro Borges

Editor in Chief
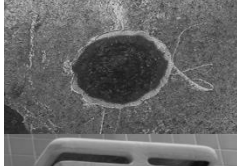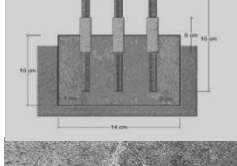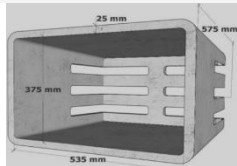
Revista ALC ONPAT

CONTENT

Use of nano-SiO₂ as a preventive maintenance surface treatment in concrete aged by carbonation

L. Vaca-Arciga[1] , D. Cruz-Moreno [1] , G. Fajardo-San Miguel [1]* ,
R. Orozco-Cruz[2] , F. Tienda[1]
* Contact author: gerardo.fajardosn@uanl.edu.mx

ABSTRACT

This study aims to evaluate the use of silicon base (NS) and functionalized (NF) nanoparticles as emerging preventive surface treatment (ST) in reinforced concrete specimens. The specimens were fabricated with a water/cement (w/c) of 0.65 and subjected to a previous aging period through exposure to CO_2. Subsequently, two different variants of the treatment were applied by spraying (using a 0.1% dispersion of nanoparticles in water) and then re-applied to carbonation. The carbonation depth and contact angle results indicate that there is an influence between the degree of aging and the efficiency of each treatment.

Keywords: surface treatment; prevention; Nano SiO₂; concrete; carbonation.

[1] Universidad Autónoma de Nuevo León, Facultad de Ingeniería Civil, (FIC-UANL), San Nicolás de los Garza, Nuevo León, México.

[2] Universidad Veracruzana, Instituto de Ingeniería, Unidad Anticorrosión, Boca del Río, Veracruz, México.

Contribution of each author

In this work, author L. Vaca-Arciga contributed with conceptualization, investigation, methodology, data collection and writing of original draft. Author D. Cruz-Moreno contributed with discussion of results, validation, writing - review and editing. Author G. Fajardo-San Miguel contributed with the original idea, supervision, resources, funding acquisition, writing - review and editing. Author R. Orozco-Cruz contributed with investigation and formal analysis. Author F. Tienda contributed with investigation, methodology and data collection.

Discussions and subsequent corrections to the publication

Any dispute, including the replies of the authors, will be published in the second issue of 2021 provided that the information is received before the closing of the first issue of 2021.

Uso de nano-SiO₂ como tratamiento superficial de mantenimiento preventivo en concreto envejecido por carbonatación

RESUMEN

Este estudio, tiene como objetivo evaluar el uso de nanopartículas base silicio (NS) y funcionalizadas (NF) como tratamiento superficial (ST) preventivo emergente en especímenes de concreto reforzado. Los especímenes fueron fabricados con una relación agua/cemento (a/c) de 0.65 y sometidos a un periodo de envejecimiento previo mediante la exposición a CO_2. Posteriormente, dos diferentes variantes del tratamiento fueron aplicadas mediante aspersión (usando una dispersión de 0.1% de nanopartículas en agua) y después fueron sometidas nuevamente a carbonatación. Los resultados de profundidad de carbonatación y ángulo de contacto indican que existe una influencia entre el grado de envejecimiento y la eficiencia de cada tratamiento.
Palabras clave: tratamiento superficial; prevención; Nano SiO_2; concreto, carbonatación.

Uso de nano-SiO₂ como tratamento de superfície como manutenção preventiva em concreto envelhecido por carbonatação

RESUMO

Este estudo tem como objetivo avaliar a utilização de nanopartículas à base de silício (NS) e funcionalizadas (NF) como tratamento preventivo de superfície (ST) emergente em corpos de prova de concreto armado. As amostras foram fabricadas com uma relação água/cimento (a/c) de 0,65 e submetidas a um período de envelhecimento prévio por exposição ao CO_2. Posteriormente, duas variantes diferentes do tratamento foram aplicadas por pulverização (utilizando uma dispersão de 0,1% de nanopartículas em água) e, em seguida, submetidas à carbonatação novamente. Os resultados de profundidade de carbonatação e ângulo de contato indicam que existe uma influência entre o grau de envelhecimento e a eficiência de cada tratamento.
Palavras-chave: tratamento da superfície; prevenção; Nano SiO2; concreto, carbonatação.

1. INTRODUCTION

In the construction industry, reinforced concrete has become the most used material worldwide, due to its low cost, ease and speed of manufacture, not to mention the combination of the high compressive strengths provided by concrete and the mechanical properties of steel that make it the ideal composite material for structural applications (Aguirre and Mejía de Gutiérrez, 2013). Deterioration in reinforced concrete structures (RCS) caused by corrosion of reinforcing steel has been the subject of study in recent decades. Some specialists (Hernández-Castañeda and Mendoza-Escobedo, 2006; Polder, Peelen and Courage, 2012; Angst, 2018) consider it the greatest challenge facing science and technology worldwide in the construction industry. The importance falls from the technical, economic and social concerns that causes the durability of the RCS, mainly when the reinforcing steel is exposed to aggressive environments. This is the case of exposure to chlorides, either from the raw material of concrete or by penetration from the surrounding environment or due to the carbonation of the concrete, which is another cause of corrosion of the reinforcement of these structures.

More than 50% of the RCS in service have deterioration problems due to the high permeability or low concrete quality. Direct losses due to costly maintenance work, and mainly repair work on structures worldwide, have been economically higher, especially in first world countries (Alhozaimy *et al.*, 2012). Currently, annual expenses are generated between 18 to 21 billion USD in rehabilitations or repairs to RCS due to corrosion of reinforcing steel (Beushausen and Bester, 2016). Reinforcing steel is protected against the corrosion process by the alkalinity of the concrete, which is the result of the cement hydration process. The pH decreases when the physical-chemical carbonation process occurs. Carbonation occurs by the reaction between CO_2 and $Ca(OH)_2$ producing $CaCO_3$ (1). As a result, $CaCO_3$ precipitates by reducing the pH in concrete, significantly decreasing the durability of reinforced concrete and its useful life.

$$Ca\,(OH)_2 + \ CO_2 \ \rightarrow CaCO_3 + \ H_2O \qquad\qquad (1)$$
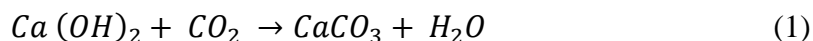
The application of surface treatments (ST) in particular has been extensively investigated in the last decades (Pigino *et al.*, 2012; Pan *et al.*, 2017; Vivar *et al.*, 2017; Hou *et al.*, 2018). They are economical and effective methods to improve the concrete quality of the surface area and to protect RCS if compared with other methods (i.e.: decreasing the w/c ratio and using pozzolan additions, increasing coating thickness, etc.)

Most ST can reduce water permeability in concrete, specifically hydrophobic impregnation, which has been achieved with the use of silanes and siloxanes, that prevents the ingress of water without hydrostatic pressure. To retard the advance of carbonation, silicate-based treatment has a more effective protection than silane and siloxane; these hardly prevent the entry of CO_2 (Li, 2017).

Nowadays, the use of nanomaterials as products for indirect protection (on concrete) of steel has been extensively studied, demonstrating in some cases that they are able to improve the performance of construction materials. Particularly in concrete, the development of smart properties that have the ability to self-clean, antimicrobial, hydrophobic, super hydrophobic, as well as the increase in mechanical properties. (Sobolev *et al.*, 2008; Jalal *et al.*, 2012; Kupwade-patil and Cardenas, 2013; Fajardo *et al.*, 2015)

Use of silicon based nanoparticles at early ages has promoted an increase in the electrical resistivity of the cementitious matrix, a decrease in the degree of CO_2 penetration and a decrease in permeability. (Cruz-Moreno *et al.*, 2017). While the use of functionalized nanoparticles, such as functionalized silica nanoparticles, have allowed the development of surfaces with super hydrophobic, self-cleaning and bactericidal properties (Zhi *et al.*, 2017; Cruz-Moreno, 2019)

The influence of the use of ST to protect the degradation of aged concretes has been studied,

providing hydrophobic and consolidating properties (Shen *et al.*, 2019). For long-term results, accelerated aging tests were performed. A decrease in carbonation progression and stable hydrophobicity was found and despite a progressive decrease in its performance over time, the residual effect usually provides a better service life for concrete (Christodoulou *et al.*, 2013; Creasey *et al.*, 2017).

The objective of this research is to analyze the effect and performance that causes the application of functionalized (NF) and non-functionalized (NS) silica nanoparticles on concrete surfaces with a certain degree of aging. On one hand, NF will provide a hydrophobic effect and, on the other, NS will provide a pore-blocking effect. The application of NS and NF is superficially by means of low-pressure spraying. This work focused on evaluating the use of silica-based nanoparticles (NS) and functionalized silica-based nanoparticles (NF) as a surface treatment for preventive maintenance methods in the deterioration of RCS in environments rich in CO_2.

2. PROCEDURE

The following paragraphs will explain the experimental development of the design, manufacture of specimens, obtaining the nanoparticles and ending with the aging by CO_2, in order to study the effect generated by the NS and NF nanoparticles as external agents in a treatment for superficial preventive maintenance in concrete. This study was divided into different stages, in order to gain a better understanding of the behavior and effects of nanoparticles in aged concrete.

2.1 Production of silicon-based nanoparticles (NS y NF)

Silicon nanoparticles (NS and NF) were obtained through sol-gel synthesis, following the procedure detailed in (Cruz-Moreno, 2015, 2019), a summary of its synthesis process is described below.

TEOS tetraethyl orthosilicate was used as a precursor of silica, ethyl alcohol as a solvent, deionized water, ammonium hydroxide as a catalyst and for the functionalization of the NS, 1,1,3,3-tetramethyldisiloxane was used as a surface modifier and nitric acid as dehydrating agent.

The procedure for the synthesis consisted of placing the ethyl alcohol with vigorous stirring at 70°C. Once this temperature was reached, the TEOS was incorporated and the stirring and temperature were maintained for 30 min. Then, the ammonium hydroxide was added, allowing it to react for an additional 30 min. Subsequently, the water was slowly added and allowed to react for an additional 60 min. Then, dropwise, excess ammonium hydroxide was added until a clear gel was formed. After 24 hours, it was placed in an oven at 110 °C for an additional 24 hours, in order to evaporate the largest amount of excess solvent and water.

To obtain the NF, it was carried out during the NS sol-gel synthesis process, where the functionalization was followed through from the addition of the distilled water and until the end of the reaction time of 60 min. Thereafter, 1,1,3,3-tetramethyldisiloxane was slowly incorporated and allowed to react for 120 min for its subsequent dehydration and surface modification when nitric acid was incorporated into the reaction. Afterwards, the ammonium hydroxide was carefully added dropwise, leaving to react for 24 h, at the end of the time it was placed in the oven at 110 °C for 24 h.

2.2 Fabrication of the specimens

Specimens were made with Ordinary Portland Cement (known as CPO 40, in accordance with NMX-C-414-ONNCCE), the proportion was designed according to the ACI 211 standard, using a water/cement ratio of 0.65, which is usual in the construction industry, see Table 1.

Table 1. Proposed concrete mixture (ACI 211, PCA).

w/c	Cement kg/m^3	Gravel kg/m^3	Sand kg/m^3	Water kg/m^3	Compressive Strength MPa	Porosity accessible to water (%)
0.65	330	756	918	215	32	11.25

For tests of compressive strength and porosity accessible to water, cylindrical specimens of lengths of 10 cm in diameter by 20 cm in length were produced. Concrete specimens were made in accordance with ASTM C39/C39M. Subsequently they followed a standard curing period (as indicated in ASTM C-231) to be later tested.

According to the Portland Cement Association (known as PCA), one of the minimum requirements for compressive strength recommended to provide protection to the concrete element in different exposure environments is 25 MPa, this indicates that the mixture complies with the protection recommendation, while the porosity accessible to water is 11.25%, indicating that the Cl$^-$ ingress will be high.

The carbonation monitoring was carried out on concrete prisms with dimensions of 10 cm x 10 cm x 30 cm. Curing was carried out with continuous water spray at 20 ° C and 100% relative humidity, where they remained for 28 days.

2.3 Aging by exposure to CO_2

At the end of the curing of the specimens, they were exposed to a CO_2-rich environment until carbonation depths that represent different aging conditions were obtained, prior to the application of the NS and NF treatment. For this, three different carbonation depths were selected as initial aging. Taking into account that the average RCS coverage is 20 mm, 0%, 25% and 50% carbonation were considered on the specimens. In other words, the first series is one that has a carbonation depth of 0 mm, the second series 5 mm and the third series 10 mm. The exposure conditions were: an atmosphere of 8% CO_2 in air, 60% ± 10% RH, at 30 °C.

2.4 Application of treatments with NS and NF

A dispersion was prepared with a dose of 0.1% of nanoparticles with respect to the volume of water. Magnetic stirring was used at 60 ° C for a period of 1 h, to facilitate the dispersion of the NS, avoiding precipitation and the crush. For the use of the NF, only magnetic stirring was necessary without the use of temperature. Two surface treatments were applied to each aging stage: a) dispersion with NS and b) dispersion with NF. All treatments are referenced with a control series without treatment (as named here, REF). Before application, all specimens had a preparation, which consisted of cleaning the surface to remove dust, grease or stains. Dispersions were prepared for each treatment, and by means of an atomizer, the solution was sprayed homogeneously over the entire surface of the specimen, leaving a rest of 30 min for the application of a second layer. At the end of the application, the specimens were kept for 14 days under laboratory conditions to promote the reaction between the NS and the cementitious matrix. (Fajardo *et al.*, 2015; Cruz-Moreno, 2019). After this time, all the specimens were re-exposed to CO_2-using the conditions described in section 2.3- to promote the advancement of carbonation.

3. METHODS

3.1 Compressive Strength
The compressive strength test was performed on 100 x 200 mm cylindrical specimens as indicated by ASTM C 39 using a hydraulic press. The mix was designed according to the ACI 211 standard for a strength of 30 MPa.

3.2 Contact angle (AC)
With the objective of evaluating the hydrophobic effect that NF confers on accelerated aging exposures, the hydrophobicity generated on the concrete surface was determined. This was done by measuring the contact angle at different aging ages following the ASTM D 5725 standard in a KRÜSS Drop Shape Analyzer model DSA25 at 23 °C. Table 2 shows the classification of the surfaces according to the angle θ obtained.

Table 2. Classification of the surfaces according to the observable angles θ maximum and minimum.

Hydrophilic	Hydrophobic	Super hydrophobic
$\theta_{min}^{max} < 90°$	$\theta_{min}^{max} \dfrac{< 150°}{> 90°}$	$\theta_{min}^{max} < 150°$

Measurements of five drops of water for injection (2µl) were taken per specimen and an image was immediately taken. Then, it was analyzed with the help of the ADVANCE V 1.9.2.3 software and the contact angle between the liquid and the surface was determined. The same specimens were used to determine the carbonation advance after making the phenolphthalein measurements. The evaluated part was on the surface where the treatments were applied, and it was measured at the same re-exposure ages, as can be seen in Figure 1.
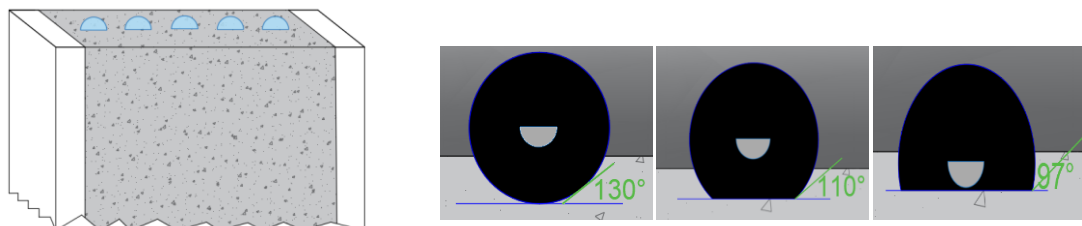
Figure 1. Interpretation of the way in which AC measurements were performed on the re-exposed specimens

3.3 Measurement of depth of carbonation
For the measurement of the depth of carbonation, phenolphthalein was used as a conventional indicator. The pink color it gives is an indicator of a concrete in good condition, that is, it still does not have carbonation problems. Figure 2 illustrates the carbonation advance for the concrete sample with and without treatments. For the measurements, the Image J program and a graduated ruler were used as a reference scale, 10 measurements were made per carbonate side of the specimen, having 3 specimens per treatment.
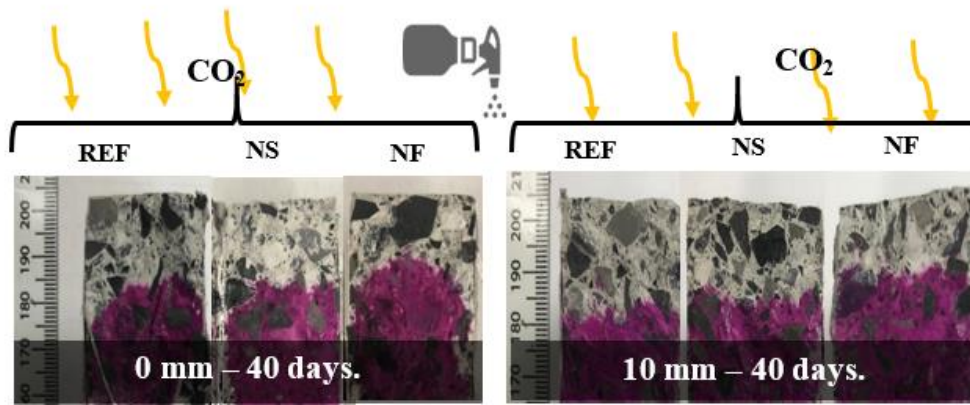
Figure 2. Advance of carbonation in samples of 0 and 10 mm of initial carbonation at 40 days of re-exposure, measured with Phenolphthalein.

4. RESULTS

4.1 Contact angle

In the Figure 3, the results of the REF and NF specimens are shown, in which the contact angle was monitored in order to know the behavior of the development of hydrophobicity on the concrete surface. Measurements were made on specimens without prior aging for more than 1000 h after application of the treatment. It can be seen that the REF sample had a practically constant behavior, with an average contact angle of 26.9°. On the other hand, the samples with NF treatment had a uniform behavior from 96 h after application, reaching a maximum angle of 123.7°. According to these results, after 24 h the surface changed from being hydrophilic to hydrophobic; and around 96 h, the NF has a stable AC in the concrete.
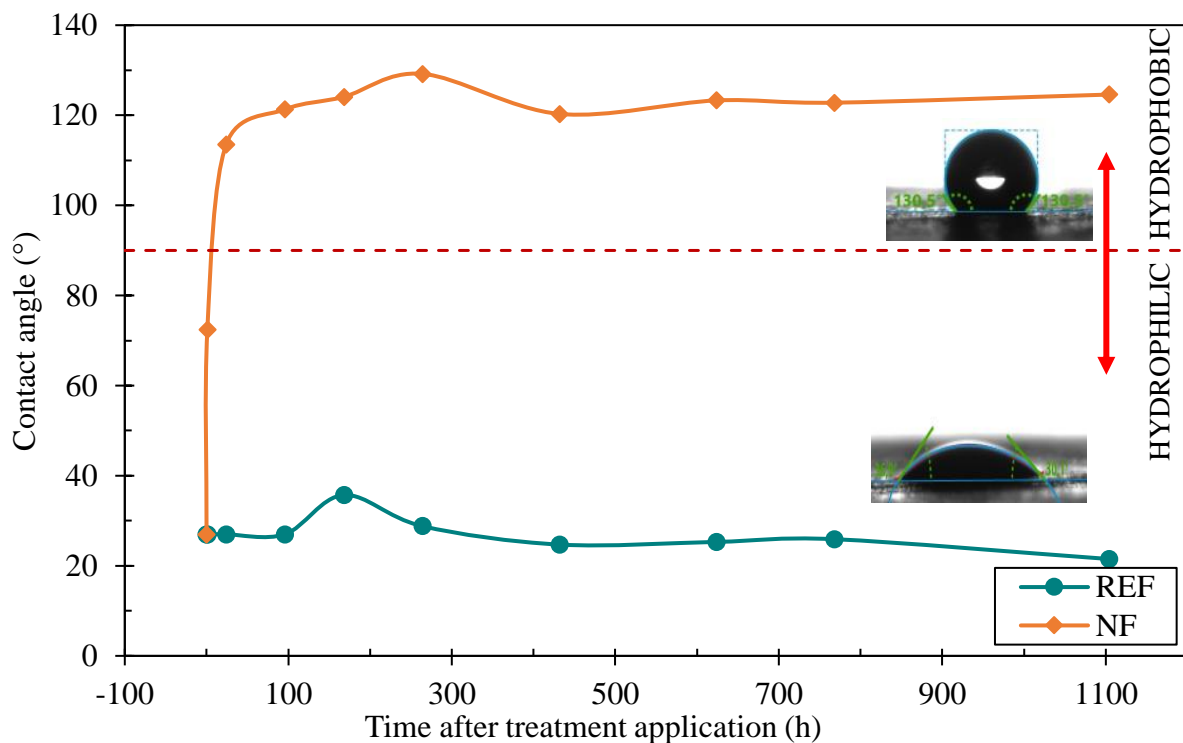
Figure 3. Contact angle behavior in samples with NF treatments hours after application.

In the Figure 4, the follow-up of the CA is presented, in the treated specimens and with the preselected initial ages, at different re-exposure ages to CO$_2$. As expected, the NS specimens had a similar behavior than the reference, since this treatment of silicon-based nanoparticles did not provide a hydrophobic effect.

The AC in the NF-treated specimens is practically constant, indicating that hydrophobicity is maintained during the exposure time, regardless of the degree of initial aging. In Figure 4.A, the NF presents the highest AC compared to the other series, being in ranges between 120-130°. This preservation of the angle can be attributed to the fact that the surface modification of the concrete due to the carbonation process did not affect the behavior of the CH$_3$ radicals, mainly responsible for the hydrophobicity of the surface.

In Figure 4.B and 4.C, the results obtained from specimens with an aging of 5 mm and 10 mm carbonation are presented. In both cases, it can be verified that the AC remained in a range between 115 and 120°, but without showing a clear trend. Based on the above, it can be concluded that aging caused by exposure to a CO$_2$ environment does not affect contact angle behavior, and therefore the development of hydrophobicity.
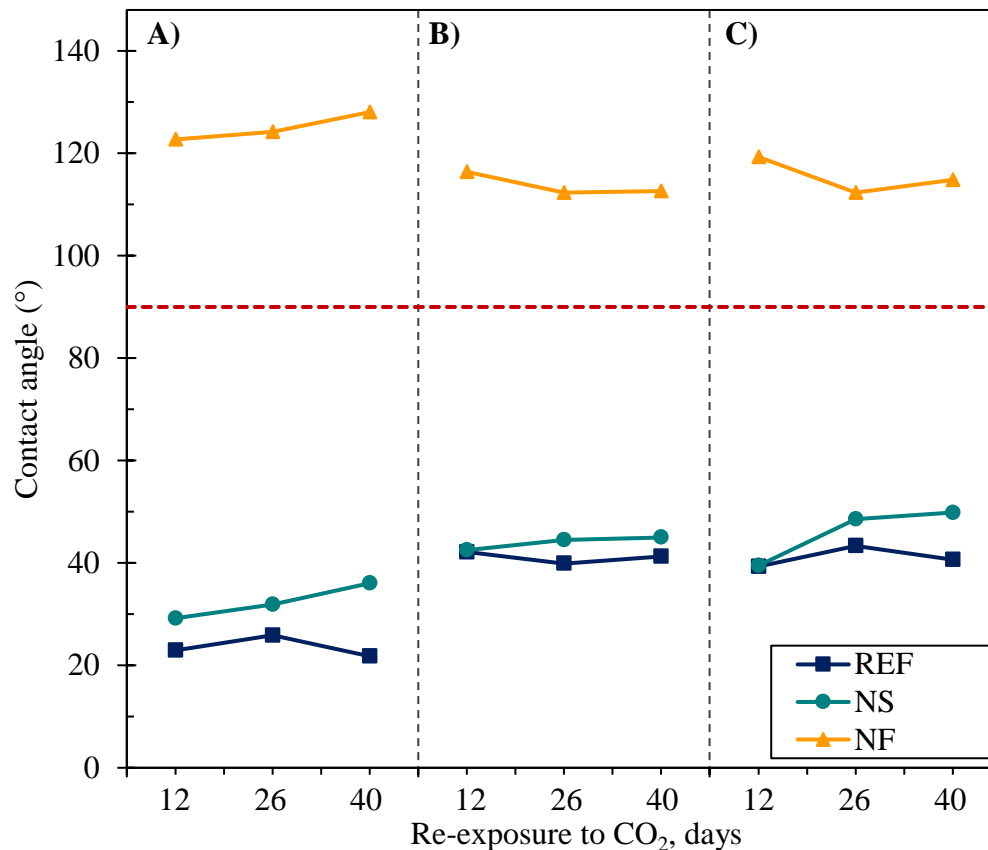
Figure 4. Variation of the contact angle of specimens with an initial aging of A) 0mm, B) 5mm and C) 10 mm of carbonation, after re-exposure to carbonation

4.2 Carbonation depth

In Figure 5, the results of the carbonation progress of the NS and NF surface treatments are presented, including the series without treatment (REF). It can be observed how the untreated series tends to have a greater carbonation depth compared to the treated samples, regardless of the degree of aging.

Specifically, in Figure 5.A, towards the end of the test period, a 36% decrease in the carbonation depth is observed in the NS-treated specimens, compared to the REF samples. While the treatment with NF obtained a 22% reduction. This is attributed to the formation of hydrated compounds as a result of the reaction of the nanoparticles with $Ca(OH)_2$, obtaining a greater amount of gels that leads to reduced permeability. These results are in agreement with the literature, where the use of NS generates a barrier effect that improves the resistance of aggressive agents[4] [6]. The treatment with NF produces a hydrophobic effect on the surface of the concrete, which gives it the ability to yield the passage of gases such as CO_2 insider, but stopping the entry of water through the repulsion of molecules of OH, for example, which are necessary to generate the reactions of the carbonation process.
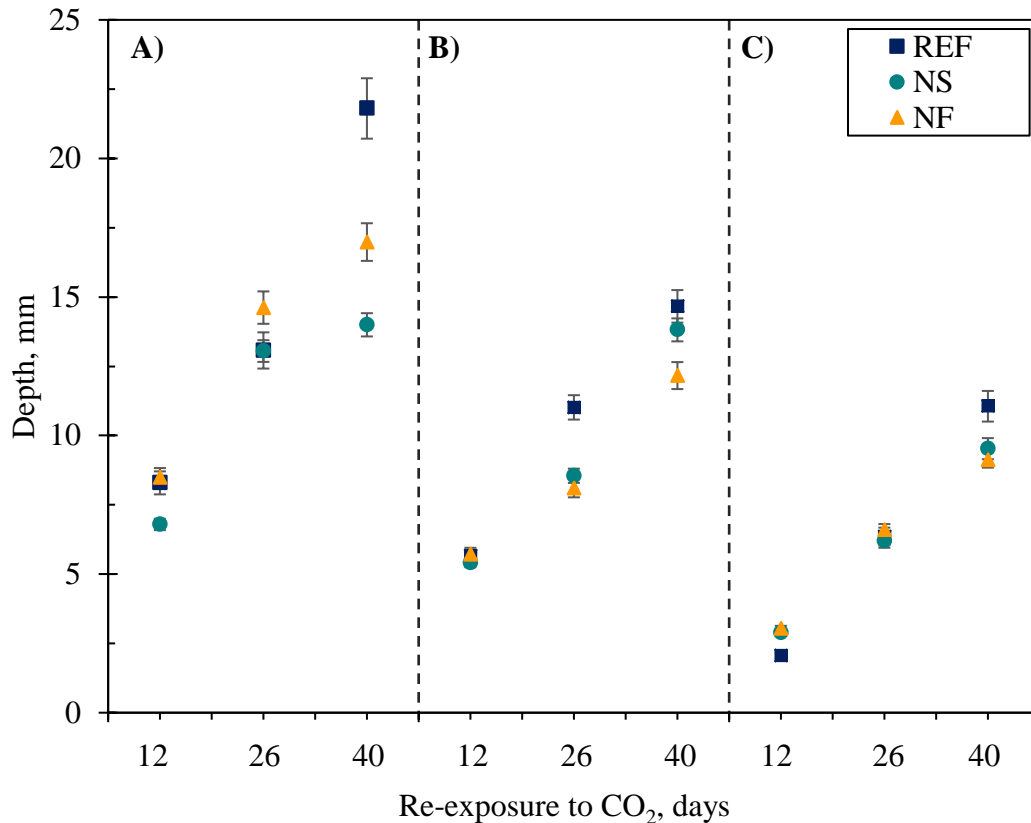
Figure 5. Depth of carbonation in specimens with A) 0 mm B) 5 mm and C) 10 mm carbonation prior to application of the treatment.

In Table 1, the values of the reduction of the carbonation advance of the specimens with the different treatments, obtained at the end of the re-exposure period, are presented. The reduction percentage (% Red) was obtained using the equation (2) established by Fajardo et al. (Fajardo *et al.*, 2015).

$$\%Red = (1 - (X_{TRAT}/X_{REF})) * 100 \ldots \qquad (2)$$

Where:
%Red= reduction in carbonation depth (vs. REF)
X_{TRAT}= carbonation depth of the treated samples (mm)
X_{REF}= carbonation depth of the untreated samples (mm)

Table 3. Percentage of reduction of carbonation vs REF of specimens treated with NS and NF; exposed to an aggressive environment with 8% CO_2 at 40 days.

Initial carbonation	%RED	
	NS	NF
0 mm	36	22
5 mm	4	13
10 mm	7	7

According to the results obtained in Table 3, all the treatments used presented a greater reduction percentage in the concrete with an initial aging of 0 mm, compared to the 5 and 10 mm aging series. It can be clearly observed that the degree of aging had an effect on the performance of the treatments. These results are similar to those found in the literature, with the difference that the application of surface treatments was carried out at early ages, even during the first days after manufacturing. For example, Franzoni (Franzoni, Pigino and Pistolesi, 2013) found that the use of nano silica has a carbonation penetration reduction effect of around 14-47%. For his part, Ibrahim (Ibrahim *et al.*, 1999) found that surface treatments based on silanes/siloxanes showed a reduction of around 20% in carbonation penetration.

The results obtained here allow to conclude that the degree of aging of the concrete reduces the performance of the treatments in the face of re-exposed to CO_2. In this way, the importance of performing an evaluation and diagnosis of the structure to be able to make a treatment selection is noticed. For structures subjected to industrial or industrial urban environments, treatment with NS and NF nanoparticles could be a feasible option when applied at early ages.

5. CONCLUSIONS

- NF treatment achieved greater hydrophobicity and stability after 96 hours of application.
- In no aging specimens (i.e., 0-mm of carbonation), the loss of AC can be attributed to a possible modification that generates carbonation between the CH_3 radicals, managing to lose hydrophobicity. The effect of the initial aging of 5 and 10 mm did not affect the hydrophobicity on the surface by using NF treatment.
- As for CO_2 accelerated aging, it is observed that NS treatment did not show expected results, since the NS have the $Ca(OH)_2$ limiting that is consumed in the carbonation process.

6. ACKNOWLEDGEMENTS

7. REFERENCES

Aguirre, A. M. and Mejía de Gutiérrez, R. (2013) "*Durabilidad del hormigón armado expuesto a condiciones agresivas*", Materiales de Construcción, 63(309), pp. 7–38. doi: https://doi.org/10.3989/mc.2013.00313.

Alhozaimy, A., Hussain, R. R., Al-Zaid, R., Al-Negheimish, A. (2012) "*Investigation of severe corrosion observed at intersection points of steel rebar mesh in reinforced concrete construction*", Construction and Building Materials. 37, pp. 67–81. doi: https://doi.org/10.1016/j.conbuildmat.2012.07.011.

Angst, U. M. (2018) "*Challenges and opportunities in corrosion of steel in concrete*", Materials and Structures. Springer Netherlands, 51(4). doi: https://doi.org/10.1617/s11527-017-1131-6.

Beushausen, H. and Bester, N. (2016) "*The influence of curing on restrained shrinkage cracking of bonded concrete overlays*", Cement and Concrete Research. Elsevier Ltd, 87, pp. 87–96. doi: https://doi.org/10.1016/j.cemconres.2016.05.007.

Christodoulou, C., Goodier, C. I., Austin, S. A., Webb, J., Glass, G. K. (2013) "*Long-term performance of surface impregnation of reinforced concrete structures with silane*", Construction and Building Materials. Elsevier Ltd, 48, pp. 708–716. doi: https://doi.org/10.1016/j.conbuildmat.2013.07.038.

Creasey, R., Andrews, J. P., Ekolu, S. O., Kruger, D. (2017) "*Long-term 20-year performance of surface coating repairs applied to façades of reinforced concrete buildings*", Case Studies in Construction Materials, 7, pp. 348–360. doi: https://doi.org/10.1016/j.cscm.2017.11.001 .

Cruz Moreno, D. M., Fajardo San Miguel, G. D. J., Flores Vivián, I., Cruz López, A., & Valdez Tamez, P. L. (2017). *Tratamiento superficial con nanopartículas base silicio inducido durante el curado: Efecto en la durabilidad de materiales base cemento portland.* Revista ALCONPAT, 7(3), 274 - 285. https://doi.org/10.21041/ra.v7i3.239

Cruz-Moreno, D. M. A. (2015) *Mejoramiento del efecto barrera en materiales endurecidos de cemento portland mediante una aplicación innovadora de nano-partículas de silicio.* Tesis de Maestría en Ciencias con Orientación en Materiales de Construcción, Universidad Autónoma de Nuevo León. Disponible en: http://eprints.uanl.mx/id/eprint/4554.

Cruz-Moreno, D. M. A. (2019) *Superficies multifuncionales en materiales de construcción base cemento portland obtenidas durante el curado con nanopartículas funcionalizadas*, Tesis de Doctorado en Ingeniería con Orientación en Materiales de Construcción. Universidad Autónoma de Nuevo León. Disponible en: http://eprints.uanl.mx/id/eprint/18517.

Fajardo, G., Cruz-Lópeza, A., Cruz-Moreno, D., Valdeza, P., Torres, G., Zanella, R. (2015), "*Innovative application of silicon nanoparticles (SN): Improvement of the barrier effect in hardened Portland cement-based materials*", Construction and Building Materials. Elsevier Ltd, 76, pp. 158–167. doi: https://doi.org/10.1016/j.conbuildmat.2014.11.054.

Franzoni, E., Pigino, B. and Pistolesi, C. (2013) "*Ethyl silicate for surface protection of concrete: Performance in comparison with other inorganic surface treatments*", Cement and Concrete Composites, 44, pp. 69–76. doi: https://doi.org/10.1016/j.cemconcomp.2013.05.008.

Hernández-Castañeda, O. and Mendoza-Escobedo, C. J. (2006) '*Durabilidad e infraestructura: retos e impacto socioeconómico*', Ingeniería Investigación y Tecnología, 7(1), pp. 57–70. doi: http://dx.doi.org/10.22201/fi.25940732e.2006.07n1.005.

Hou, P., Li, R., Li, Q., Lu, N., Wang, K., Liu, M., Cheng, X. and Shah, S. (2018) '*Novel superhydrophobic cement-based materials achieved by construction of hierarchical surface structure with FAS/SiO2 hybrid nanocomposites*', Engineered Science Materials & Manufacturing. doi: https://doi.org/10.30919/esmm5f125.

Ibrahim, M., Al-Gahtani, A. S., Maslehuddin, M. and Dakhil, F. H. (1999), "*Use of surface treatment materials to improve concrete durability*", Journal of Materials in Civil Engineering, Vol. 11, Issue 1. doi: https://doi.org/10.1061/(ASCE)0899-1561(1999)11:1(36)

Jalal, M., Mansouri, E., Sharifipour, M. and Pouladkhan, A. R. (2012), "*Mechanical, rheological, durability and microstructural properties of high performance self-compacting concrete containing SiO_2 micro and nanoparticles*", Materials and Design. Elsevier Ltd, 34, pp. 389–400. doi: https://doi.org/10.1016/j.matdes.2011.08.037.

Kupwade-patil, K. and Cardenas, H. E. (2013), "*Electrokinetic nanoparticle treatment for corrosion remediation on simulated reinforced bridge deck* ", Journal of Nanoparticle Research, 15 (1952). doi: https://doi.org/10.1007/s11051-013-1952-3.

Pan, X., Shi, Z., Shi, C., Ling, T.-C. and Li, N. (2017a) '*A review on concrete surface treatment Part I: Types and mechanisms*', Construction and Building Materials. Elsevier Ltd, 132, pp. 578–590. doi: https://doi.org/10.1016/j.conbuildmat.2016.12.025.

Pan, X., Shi, Z., Shi, C., Ling, T.-C. and Li, N. (2017b) '*A review on surface treatment for concrete – Part 2: Performance*', Construction and Building Materials. Elsevier Ltd, 133, pp. 81–90. doi: https://doi.org/10.1016/j.conbuildmat.2016.11.128.

Pigino, B., Leemann, A., Franzonia, E. and Lura, P. (2012) '*Ethyl silicate for surface treatment of concrete – Part II: Characteristics and performance*', Cement and Concrete Composites. Elsevier Ltd, 34(3), pp. 313–321. doi: https://doi.org/10.1016/j.cemconcomp.2011.11.021.

Polder, R. B., Peelen, W. H. A. and Courage, W. M. G. (2012) '*Non-traditional assessment and maintenance methods for aging concrete structures - Technical and non-technical issues*', Materials and Corrosion, 63(12), pp. 1147–1153. doi: https://doi.org/10.1002/maco.201206725.

Shen, L., Jiang, H., Wang, T., Chen, K. and Zhang, H. (2019) '*Progress in Organic Coatings Performance of silane -based surface treatments for protecting degraded historic concrete*', Progress in Organic Coatings. Elsevier, 129, pp. 209–216. doi: https://doi.org/10.1016/j.porgcoat.2019.01.016.

Sobolev, K., Flores, I., Hermosillo, R. and Torres-Martínez, L. M (2008), *Nanomaterials and Nanotechnology for High-Performance Cement Composites*, Symposium Paper, International Concrete Abstracts Portal, American Concrete Institute: ACI Special Publication, 254, pp. 93–120. URL: http://citeseerx.ist.psu.edu/viewdoc/download?doi=10.1.1.452.2354&rep=rep1&type=pdf.

Vivar Mora, L., Naik, S., Paul, S., Dawson, R., Neville, A. and Barker, R. (2017) *Influence of silica nanoparticles on corrosion resistance of sol-gel based coatings on mild steel*, Surface and Coatings Technology. Elsevier B.V., 324, pp. 368–375. doi: https://doi.org/10.1016/j.surfcoat.2017.05.063

Zhi, J.-H. Zhang, L.-Z., Yan, Y. and Zhu, J. (2017), *Mechanical durability of superhydrophobic surfaces: The role of surface modification technologies*, Applied Surface Science. Elsevier B.V., 392, pp. 286–296. doi: https://doi.org/10.1016/j.apsusc.2016.09.049.

The importance of underpaint corrosion caused by damage to paint on steel structures

G. L. Ribeiro Filho[1]* (iD), R. A. J. Ribas[2] (iD), G. D. Paula[2] (iD)

*Contact author: guidolessa@yahoo.com.br
DOI: https://doi.org/10.21041/ra.v10i3.257

ABSTRACT

The impact of varying the dry paint film thickness (DFT) on the underpaint corrosion of steel plates obtained from the floor of an offshore oil platform is evaluated. The specimens were all prepared using the same material and paint scheme, and the DFT and exposure conditions in a salt spray chamber were varied and compared with the results obtained in a real situation. The results indicated that corrosion initiated at sites where the paint was damaged, may be more important than corrosion through the undamaged paint due to permeation, even in cases where the DFT is thin. In specimens whose substrates were previously damaged, there were pathological manifestations of osmotic blistering. The underpaint corrosion that occurred after the paint was damaged in the field occurred at an intensity like that observed for the tested specimens.

Keywords: structures; steel; film; painting; corrosion.

_____

[1] Federal Institute of Education, Science and Technology of Minas Gerais (IFMG), Belo Horizonte, Brazil.
[2] Mining School, Federal University of Ouro Preto (UFOP), Ouro Preto, Brazil.

Responsible Associate Editor for this paper: Paulo Helene

Contribution of each author
The author G. L. Ribeiro Filho contributed with the original idea, coordination of experiments, data collection, analysis and discussion of results and writing of the work. The author R. A. J. Ribas contributed with the guidance of the author, analysis and discussion of the results and writing of the work. The author G. D. Paula contributed to the coorientation of the work.

Discussions and subsequent corrections to the publication
Any dispute, including the replies of the authors, will be published in the second issue of 2021 provided that the information is received before the closing of the first issue of 2021.

Importância da corrosão subpelicular por descontinuidade da película de pintura em estruturas de aço

RESUMO

O trabalho avaliou impacto da variação da espessura da película seca de pintura (EPS) na corrosão subpelicular em chapas de aço do piso de uma plataforma de petróleo. Foram preparados corpos de prova (CPs) com material e esquema de pintura do projeto, com variação das EPS, exposição em câmara de névoa salina (salt spray) e comparados com situação real. Os resultados indicaram que corrosões iniciadas em danos à película podem ganhar maior importância que corrosões por permeabilidade através da película, mesmo as com baixa EPS, porém contínua. Em CPs com prévia contaminação do substrato, observaram-se manifestações patológicas de empolamento por osmose. A corrosão subpelicular a partir do rompimento da película em campo ocorreu numa intensidade semelhante aos CPs ensaiados.
Palavras-chave: estruturas; aço; película; pintura; corrosão.

La importancia de la corrosión subpelicular por discontinuidad de la película de pintura en estructuras de acero

RESUMEN

El trabajo evaluó el impacto de la variación del grosor de la película de pintura seca (GPS) sobre la corrosión subpelicular en láminas de acero del piso de una plataforma petrolera. Se prepararon cupones de prueba (CP) con el esquema de pintura y material del proyecto, con variación de GPS, exposición en una cámara de niebla salina y comparación con la situación real de campo. Los resultados indicaron que la corrosión iniciada en el daño de la película puede ganar mayor importancia que la corrosión por permeación a través de aquella, inclusive en los lugares de GPS bajo, aunque sea continuo. En los CPs con contaminación previa del sustrato, hubo manifestaciones patológicas de ampollas osmóticas. La corrosión subpelicular de la ruptura de la película de campo se produjo a una intensidad similar a la de los CPs probados.
Palabras clave: estructuras; acero; película; pintura; corrosión.

1. INTRODUCTION

Corrosion is a spontaneous process in which metals deteriorate, resulting in chemical and/or electrochemical changes that tend to bring the metals back to their original state, which releases the energy applied in the metallurgy process. The corroded metal in a lower energy state returns to the most primitive state of the metal and loses the properties it acquired during the metallurgy process, such as its mechanical strength, elasticity, ductility, aesthetics and other characteristics, which vary according to the type of alloy. The product resulting from the corrosion process is the ore itself, i.e., oxides, hydroxides, carbonates, sulfides, sulfates, silicates, etc. (Silva, 1981; Ramanathan, 1988; Gentil, 2007; Nunes and Lobo, 2007).

A relevant engineering factor of the corrosion process is the speed with which corrosion occurs. By assuming that every metal can be used in any medium as long as the corrosion rate is compatible with the application, the economic viability of less noble metals can be ensured for certain uses. Thus, steel can be widely used in structures if proper anticorrosion protection is applied through painting, coating, galvanization, and metallization, among other processes (Silva, 1981).

Atmospheric corrosion occurs basically by the electrochemical mechanism. This mechanism is most frequently observed in nature and is characterized by the presence of liquid water and temperatures below the dew point (usually room temperature) and occurs due to the formation of electrochemical corrosion cells or batteries. Thus, it is understood that electrons move from one area of the metallic material to another by means of an aqueous solution capable of conducting electricity, i.e., salts or ions must exist in the liquid water (electrolytes), causing oxidation reactions at one site and reduction reactions at another site (Nunes and Lobo, 2007). The water molecules are polar and aggregates to the metal ions of the metal that contact the electrolyte, forming ions (aggregates of this metal without its valence electrons), and this reaction results in the dissolution of the metal; that is, corrosion is a destructive chemical reaction that occurs between the metal or metal alloy and the environment (Wolynec, 2003; Jones, 1996).For corrosion to occur, the substrate must contact the electrolyte; hence, metal corrosion protection is important.

In general, industrial, naval and civil structures use paint as a form of protection, which, when properly applied, offers good protection at a reasonable cost. The contact between the electrolyte and the substrate, which is capable of initiating the corrosion process, may occur due to the paint permeability (caused by failures in the paint due to the painting process, such as thin coatings or a high porosity), corrosive agents in the medium attacking the paint (caused by an incorrect choice of paint type) or paint damaged mechanically, which causes most of the corrosion observed in the studied offshore platform. The damaged paint eliminates the barrier protection and allows the corrosive agent to contact the substrate; in addition, paint damage causes the loss of protection by the corrosion inhibitors that may be present in the paint formulation (Chawla and Gupta, 1995).

According to Chawla and Gupta (1995), paint resists the passage of corrosive agents and reduces the ionic movement that permeates the corrosive agents; however, the resistance offered is not good enough to inhibit corrosion.

The paint type and dry film thickness (DFT) must be compatible with the corrosive agents present in the medium, and a thickness of 250 μm is recommended for highly aggressive atmospheres, as is the case for petroleum platforms installed in marine environments (Nunes and Lobo, 2007).

In this context, the objective of this study was to evaluate the impact of varying the DFT on underpaint corrosion in steel plates obtained from the floor of an offshore oil platform.

2. METHODOLOGY

In this methodology, the underpaint corrosion of the specimens was compared with that observed for the case study of an oil platform. The specimens, with dimensions of 150 mm x 100 mm x 6.3 mm, were prepared from floor plates used to construct the platform (steel NV-A36), and the paint scheme provided in the painting procedure with some thickness variations was used (Figure 1). These specimens had damaged paint (carvings) and were subjected to a salt spray test for 1550 h to evaluate the effects of the DFT on underpaint corrosion.

2.1 Preparation of the specimens
Six groups of specimens were prepared, where groups 1 to 5 were composed of four specimens each (named A, B, C and D), and group 6 was composed of only two specimens (named A and B). All specimens were previously washed with clean water. The specimens from groups 1 and 2 were previously subjected to St3 and Sa2½ surface preparation methods, respectively, according to standard ISO 8501-1 (ISO, 2007) and standard NBR 10443 (ABNT, 2008), respectively, and were then subjected to a small thickness coating system. Groups 3 and 4 were subjected to St3 and Sa2½ surface preparation methods, respectively, and a complete paint system was used to apply the paint to the atmospheric zone[1] (Table 1); according to the painting procedure used for the project, which expects a DFT between 445 μm and 600 μm, the DFT was measured for each layer. Prior to painting, the roughness of all specimens was measured after the Sa2½ preparation method was performed to verify if the DFT requirement of 50 μm to 100 μm, as predicted in the painting procedure of the project, was met (Figure 2).
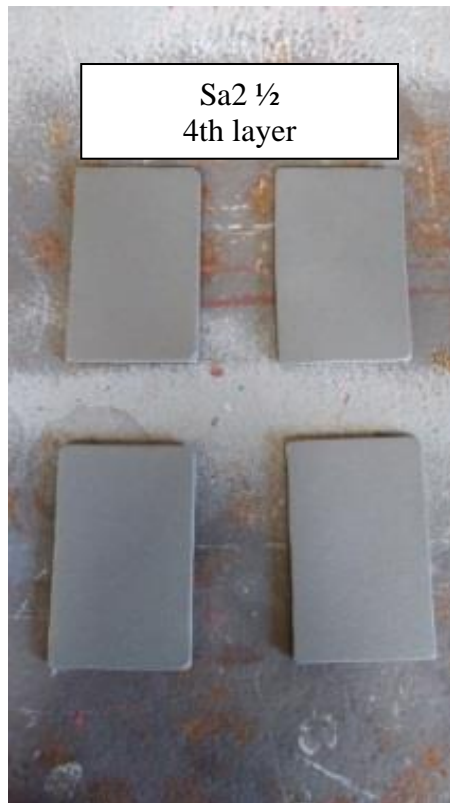
Figure 1 Plates prepared with a Sa2½ abrasive jet (Ribeiro Filho, 2018)

Figure 2 Roughness meter used to measure the roughness of a St3 standard plate (Ribeiro Filho, 2018)

[1] Atmospheric zone – Elements of the platform that are located above sea level.

Table 1. Painting scheme used for the atmospheric zone

SURFACE TREATMENT			
Operation temperature	**Preparation treatment**	**Soluble salts in water**	**Roughness profile**
Up to 80°C	Sa2½	<5 µg/cm^2	50 µm to 100 µm

PAINT APPLICATION							
Number of coatings	**Paint**	**DFT^2 (µm)**		**Color**	**Method of application**	**Paint interval**	
		Minimum	**Maximum**			**Minimum**	**Maximum**
1	N-2680 Epoxy without solvents^3	135	180	Red	Roll / brush without air gun	12 h	120 h
2	N-2680 Epoxy without solvents	135	180	Light gray	Roll / brush without air gun	12 h	120 h
3	N-2680 Epoxy without solvents	135	180	Light gray	Roll / brush without air gun	12 h	120 h
4	N-2677 Polyurethane^4	40	60	According to local	Roll / brush spray gun	-	-

The surfaces of the specimens that received the St3 treatment were treated according to the standard ISO 8501-1 (ISO, 2007); the surfaces of the specimens that received the Sa2½ treatment were treated according to the standard NBR 15239 (ABNT, 2005). After each paint coating, the DFT was measured according to the standard NBR 10443 (ABNT, 2008), and the results of the preparation method are presented in Table 2. Figures 3 and 4 show images of the paint and the DFT measurement.

Table 2. Preparation of the test specimens

Group	1	2	3	NaCl 4	Salt test 5	N-2680 6	7	N-2680 8	9	N-2680 10	11	N-2677 12	13	Mean DFT 14
1	B	St3	42 µm*	no	<5 µg/cm^2	x	136 µm	-	-	-	-	x	31 µm	167 µm
2	B	Sa2½	72 µm	no	<5 µg/cm^2	x	119 µm	-	-	-	-	x	55 µm	174 µm
3	B	St3	N/A	no	<5 µg/cm^2	x	138 µm	x	115 µm	x	229 µm	x	69 µm	551 µm
4	B	Sa2½	68 µm	no	<5 µg/cm^2	x	154 µm	x	149 µm	x	203 µm	x	72 µm	578 µm
5	A	Sa2½	65 µm	yes	19 µg/cm^2	x	110 µm	-	-	-	-	x	60 µm	170 µm
6	D	St3	N/A	no	<5 µg/cm^2	x	210 µm	-	-	-	-	x	73 µm	283 µm

^{2} DFT – Dry Film Thickness.
^{3} N-2680 – Bio-compound paint (A – epoxy resin/ B – curing agent: polyamine) – Petrobras standard used for paints.
^{4} N-2677 – Polyurethane Acrylic Aliphatic Paint (A – acrylic resin / B – curing agent: polyisocyanate aliphatic) – Petrobras standard used for paints.

The importance of underpaint corrosion caused by damage to paint on steel structures
Ribeiro Filho, G. L., Ribas, R. A. J., Paula, G. D.

Index of the columns in Table 2
Column 1 - Degree in which the plate was corroded before preparation, according to the photographic standard of ISO 8501-1 (ISO, 2007).
Column 2 - Surface preparation treatment according to the standard ISO 8501-1 (ISO, 2007), which was applied by a rotating mechanical tool with 24 grit sanding discs, according to standard BR 15239 (ABNT, 2005) for the St3 treatment and standard N-9 (PETROBRAS, 2006) for the Sa2½ treatment.
Column 3 - Result of the roughness test according to standard SP-0287 (NACE, 2016).
Column 4 - Was NaCl contamination performed prior to painting?
Column 5 - Result of the salt test of the contaminated surfaces, according to ISO 8502-6 (ISO, 2006).
Column 6 - The first coat of the N-2680 paint was applied.
Column 7 - The DFT of the first coat of the N-2680 paint.
Column 8 - The second coat of the N-2680 paint was applied.
Column 9 - The DFT of the second coat of the N-2680 paint.
Column 10 - The third coat of the N-2680 paint was applied.
Column 11 - The DFT of the third coat of the N-2680 paint.
Column 12 - The final coat of the N-2677 paint was applied.
Column 13 - The DFT of the final paint coating.
Column 14 - The total DFT.

*For surface treatment St3, a roughness test is not applicable; however, a roughness measurement was performed for group 1 to verify the effectiveness of the treatment.
Notes:
- Groups 1, 3 and 6 received the St3 surface treatment;
- Groups 2, 4 and 5 received the Sa2½ surface treatment;
- A thin DFT layer was applied to groups 1, 2 and 6;
- Groups 3 and 4 underwent the complete paint scheme – the minimum DFT was 445 μm (3x135 μm + 40 μm), and the maximum DFT was 600 μm (3x180 μm + 60 μm).

(PU) polyurethane
Color code N6.5 (grey)

Group 1
1A, 1B – rounded edges
1C, 1D 1E – normal edges

219

Figure 3. Finishing the paint (Ribeiro Filho, 2018).
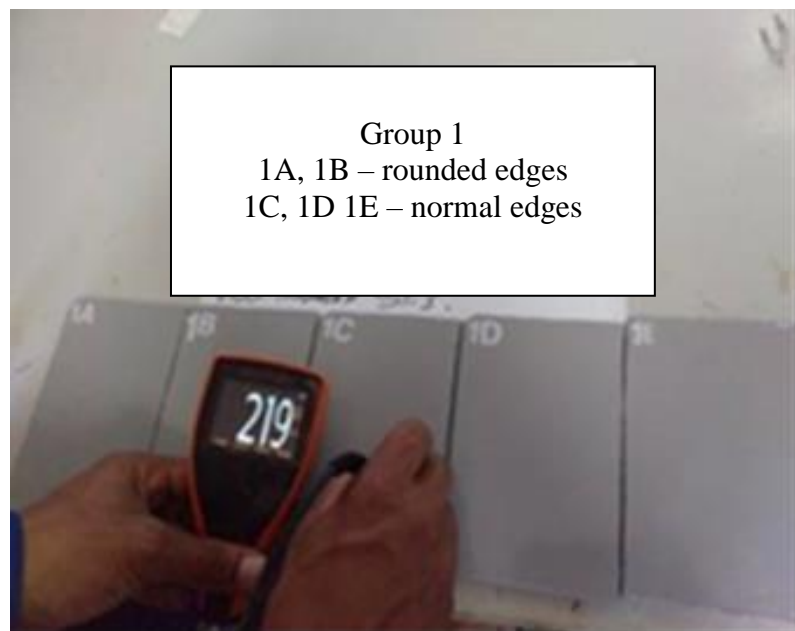
Figure 4. Measuring the total DFT (Ribeiro Filho, 2018).

The importance of underpaint corrosion caused by damage to paint on steel structures
Ribeiro Filho, G. L., Ribas, R. A. J., Paula, G. D.

291

Unlike groups 1, 2, 3 and 4, in which a corrosion grade B plate was used, a corrosion grade A plate was used in group 5, which was contaminated with sodium chloride after the preparation treatment was applied with the Sa2½ standard abrasive jet, and subsequently, thin paint layers were applied. After contamination, the salinity on the surface of the specimens was measured to be 19 µg/cm^2, which was verified according to the standards ISO 8502-6 (ISO, 2006) (salt test) and ISO 8502-9 (ISO, 1998) and was higher than the maximum limit for structures located in the atmospheric zone, which, in this case, cannot exceed 5 µg/cm^2.

The presence of sodium chloride at the beginning of and during the corrosion process is decisive regarding the exposure to weathering. (Sosa et al., 2018).

For group 6, only two specimens were prepared using corrosion grade D plates to verify the corrosion behavior in a specific situation of thin thickness on the convex surface, i.e., the paint on the weld points on the surface of the plate.

After painting, the paint layers were carved to simulate experimental damage/defects in the paint applied to the specimens from all groups; some of the carvings were longitudinal, and some were puncture carvings with 5 mm diameters, as shown in Figure 5.

2.2 Salt spray chamber

All specimens were subjected to a salt spray chamber (Figure 6) with a 5% sodium chloride (NaCl) saline mist, in which the mist was uniformly sprayed at a controlled temperature, according to ISO 9227 (ISO, 2012), NBR-8094 (ABNT, 1983) and B117-16 (ASTM, 2001). The temperature was maintained within the interval of 35 ± 2°C, and the specimens remained in the salt spray chamber for 1550 h.

Figure 5. Specimens with experimentally damaged paint (Ribeiro Filho, 2018).

Figure 6. Specimens in the salt chamber before exposure to the mist (Ribeiro Filho, 2018).

2.3 Penetrant liquid test

After removing the specimens from the saline chamber (Figure 7), the specimens were washed with clean running water at room temperature (<40°C) to remove the salt deposits and immediately dried. Subsequently, the specimens were subjected to a penetrant liquid (PL) test, according to the standard NBR 9583 (ABNT, 1997), and the points of higher corrosion incidence were determined (Figures 8 and 9).

These points were selected, and the specimens were cross-sectioned at those points (Figure 10). The cross-sections were observed under an LBM-044 microscope/stereoscope to measure the extent of the underpaint corrosion.
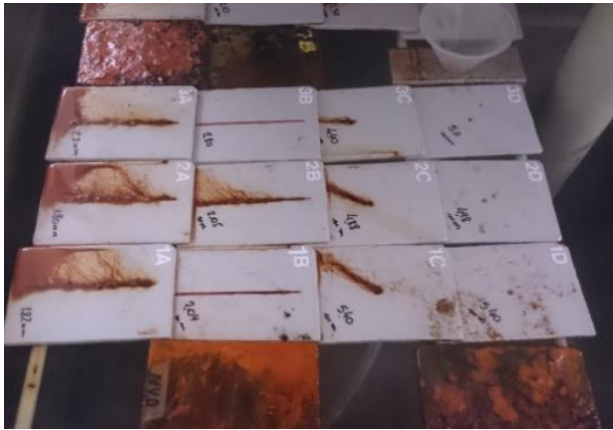
Figure 7. Specimens after the 1550 h exposure (Ribeiro Filho, 2018).

Figure 8. PL test awaiting development (Ribeiro Filho, 2018).

Figure 9. Specimen awaiting development (Ribeiro Filho, 2018).
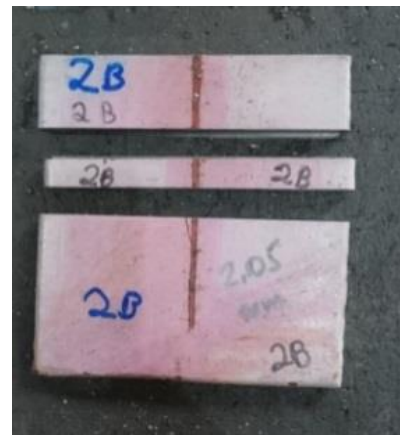
Figure 10. Specimen sectioned for microscopy observation (Ribeiro Filho, 2018).

3. RESULTS

Three underpaint corrosion measurements were performed for each section, and the results are shown in Table 3.

Table 3. Underpaint corrosion measurements of the specimens

Group	Specimen	Degree of corrosion	Surface treatment	DFT (μm)	Damage to the paint before the salt spray test				Corrosion extent (mm)			
					Damage created	Width of the damage (mm)	Ø of the damage (mm)	Depth of the damage	Measurement 1	Measurement 2	Measurement 3	Mean
1	1A	B	St3	167	longitudinal	2	-	reached the substrate	1.120	0.705	0.890	**0.91**
	1B	B			longitudinal	2	-	preserved bottom paint layer	0.000	0.000	0.000	**0.00**

Group	Specimen	Degree of corrosion	Surface treatment	DFT (µm)	Damage to the paint before the salt spray test				Corrosion extent (mm)			
					Damage created	Width of the damage (mm)	Ø of the damage (mm)	Depth of the damage	Measurement 1	Measurement 2	Measurement 3	Mean
	1C	B			puncture	-	5	reached the substrate	0.963	1.582	2.120	**1.56**
	1D	B			puncture	-	5	preserved bottom paint layer	0.000	0.000	0.000	**0.00**
2	2A	B	Sa2½	174	longitudinal	2	-	reached the substrate	0.888	1.060	0.390	**0.78**
	2B	B			longitudinal	2	-	preserved bottom paint layer	0.000	0.000	**1.010**	**0.34**
	2C	B			puncture	-	5	reached the substrate	0.550	1.711	1.084	**1.12**
	2D	B			puncture	-	5	preserved bottom paint layer	0.000	0.000	0.000	**0.00**
3	3A	B	St3	551	longitudinal	2	-	reached the substrate	1.034	1.19	1.175	**1.13**
	3B	B			longitudinal	2	-	preserved bottom paint layer	0.000	0.000	0.000	**0.00**
	3C	B			puncture	-	5	reached the plate (substrate)	1.273	1.041	0.880	**1.06**
	3D	B			puncture	-	5	preserved bottom paint layer	0.000	0.000	0.000	**0.00**
4	4A	B	Sa2½	578	longitudinal	2	-	reached the substrate	1.038	1.170	0.585	**0.93**
	4B	B			longitudinal	2	-	preserved bottom paint layer	0.000	0.000	0.000	**0.00**
	4C	B			puncture	-	5	reached the substrate	0.000	0.930	1.160	**0.70**
	4D	B			puncture	-	5	preserved bottom paint layer	0.000	**0.223**	0.000	**0.07**
5	5A	A	Sa2½	170	longitudinal	2	-	reached the substrate	1.195	0.950	0.490	**0.88**
	5B	A			longitudinal	2	-	preserved bottom paint layer	0.000	0.000	**0.780**	**0.26**
	5C	A			puncture	-	5	reached the substrate	1.049	1.238	1.120	**1.14**
	5D	A			puncture	-	5	preserved bottom paint layer	0.000	0.000	0.000	**0.00**
6	6A	D	St3	283	puncture	-	5	reached the substrate	-	-	-	**0.81**
	6B	D			puncture	-	-	preserved bottom paint layer	-	-	-	**0.00**

3.1 Analysis of the results

The results showed that no corrosion occurred, or it reached very low levels in cases where there was at least a continuous bottom paint layer; this happened even when the surface was prepared with the St3 preparation treatment and the paint was thin (Table 3). In turn, in all cases where the paint layer was discontinuous and the substrate was exposed to the medium, the corrosion advanced

The importance of underpaint corrosion caused by damage to paint on steel structures
Ribeiro Filho, G. L., Ribas, R. A. J., Paula, G. D.

under the paint, almost identically, by approximately 1 mm for the 1550 h exposure, i.e., a rate on the order of 6.5 x 10⁻⁴ mm/h.

Tables 4, 5 and 6, which were obtained from Table 3, show that a mean corrosion extent of 0.96 mm was obtained for groups 3 and 4 (complete paint system), and a mean corrosion extent of 1.03 mm was obtained for groups 1, 2 and 6[5] (thin thickness) (Tables 4 and 5). Even in the case of group 5, in which the paint was thin and the surface was contaminated with NaCl, the mean corrosion extent (1.01 mm) was close to that obtained for the other groups (Table 6), which can be attributed to the low degree of corrosion penetration under the paint (despite contamination) and the use of a corrosion grade A plate. This was the only group that exhibited blistering[6], with sparse bubbles on the surface of the plate, which is probably due to the osmosis caused by the paint under saline contamination conditions.

Table 4. Corrosion of the specimen - Thin paint coatings

Group	Specimen	Corrosion degree	Treatment of the surface	DFT (µm)	Damage to the paint coating before the *salt spray* test				Corrosion extent (mm)				Mean corrosion extent (mm) for specimens with a thin DFT
					Damage created	Width of the damage (mm)	Ø of the damage (mm)	Depth of the damage	Measurement 1	Measurement 2	Measurement 3	Mean	
1	1A	B	St3	167	longitudinal	2	-	reached the substrate	1.120	0.705	0.890	0.91	1.03
	1B	B			longitudinal	2	-	preserved the bottom paint layer - paint intact	0.000	0.000	0.000	0.00	
	1C	B			puncture	-	5	reached the substrate	0.963	1.582	2.120	1.56	
	1D	B			puncture	-	5	preserved the bottom paint layer - paint intact	0.000	0.000	0.000	0.00	
2	2A	B	Sa2 ½	174	longitudinal	2	-	reached the substrate	0.888	1.060	0.390	0.779	
	2B	B			longitudinal	2	-	preserved the bottom paint layer - paint intact	0.000	0.000	1.010	0.337	
	2C	B			puncture	-	5	reached the substrate	0.550	1.711	1.084	1.115	
	2D	B			puncture	-	5	preserved the bottom paint layer - paint intact	0.000	0.000	0.000	0.000	
6	6A	B	St3	283	puncture	-	5	reached the substrate	-	-	-	0.81	

[5]Group 6 was considered together with the systems receiving the thin thicknesses due to its proximity to the minimum DFT desired for highly aggressive environments (250 µm).

[6]Blistering – Pathology of the paint known as blistering, or bubbles, which appear as semi-spherical protrusions in the paint and vary in size and intensity. The inside of the bubbles may or may not contain a liquid.

Table 5. Corrosion in specimen with complete system – Thick paint coating

Group	Specimen	Degree of corrosion	Surface treatment	DFT (µm)	Damage to the paint film before the salt spray test				Corrosion extent (mm)				Mean corrosion extent (mm) for specimens with a thick DFT
					Damage created	Width of the damage (mm)	Ø of the damage (mm)	Depth of the damage	Measurement 1	Measurement 2	Measurement 3	Mean	
3	3A	B	St3	551	longitudinal	2	-	reached the substrate	1.034	1.190	1.175	1.13	0.96
	3C	B			puncture	-	5	reached the substrate	1.273	1.041	0.880	1.06	
4	4A	B	Sa2 ½	578	longitudinal	2	-	reached the substrate	1.038	1.170	0.585	0.93	
	4C	B			puncture	-	5	reached the substrate	0.000	0.930	1.160	0.70	

Table 6. Corrosion in specimen with incomplete system and NaCl contamination

Group	Specimen	Degree of corrosion	Surface treatment	DFT (µm)	Damage to the paint film before the salt spray test				Corrosion extent (mm)				Mean (mm) for specimens with a thin thickness and NaCl
					Damage created	Width of damage (mm)	Ø of the damage (mm)	Depth of the damage	Measurement 1	Measurement 2	Measurement 3	Mean	
5	5A	A	Sa2 ½	170	longitudinal	2	-	reached the substrate	1.195	0.950	0.490	0.88	1.01
	5B	A			longitudinal	2	-	preserved the bottom layer - paint intact	0.000	0.000	0.780	0.26	
	5C	A			puncture	-	5	reached the substrate	1.049	1.238	1.120	1.14	

For example, the observations made using a microscope, as illustrated in Figures 11 and 12, showed that in cases where the paint damage reached the substrate, corrosion occurred in both of the complete paint schemes (specimen 4A) and the thin-thickness scheme (specimen 2A), both of which used surface preparation treatment Sa2½, which offers greater adherence.

In contrast, specimen 1B (Figure 13), which was prepared with a thin DFT and received previous paint damage but had the bottom paint layer preserved, exhibited corrosion after 1550 h. For similar cases, there was an exception only for specimens 2B, 4D and 5B, where reduced corrosion was observed, and this occurred only in one of the three measurements shown in bold in Table 3. It was therefore concluded that when the surface preparation treatment (the standard St3 or Sa2½ treatment) is well performed, the electrolyte tends to access the substrate by the discontinuous paint if the paint exhibits a low permeability and porosity and receives a low peak exposure, as was the case for the specimens prepared for this study, and the resulting corrosion rate is similar for all the cases presented, even when the paint thicknesses are significantly different for the considered exposure time (1550 h).

Figure 14 shows the image of specimen 6A, in which the paint thickness on a welded point varied significantly. However, due to its integrity, the anticorrosion protection of the system was preserved, even with a film thickness of 283 μm.
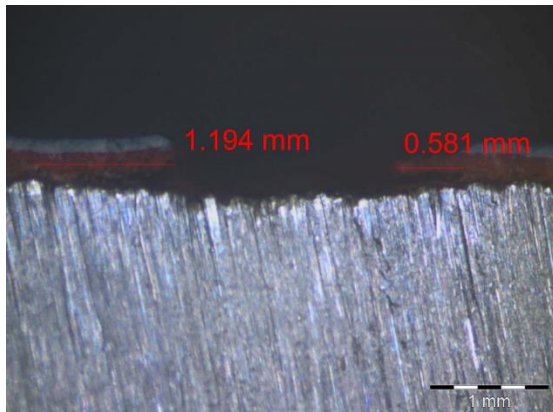
Figure 11. Underpaint corrosion measurement performed on specimen 2A (Ribeiro Filho, 2018).
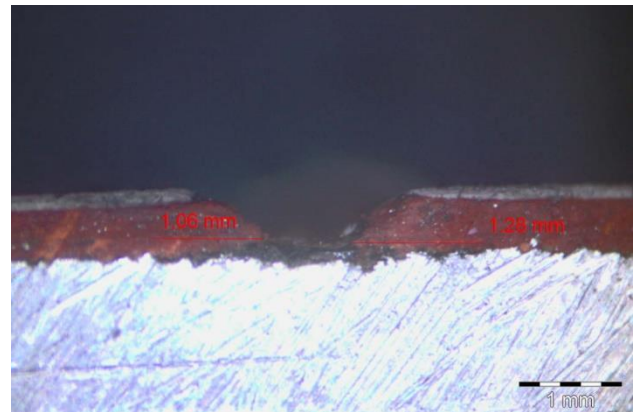
Figure 12. Underpaint corrosion measurement performed on specimen 4A (Ribeiro Filho 2018).
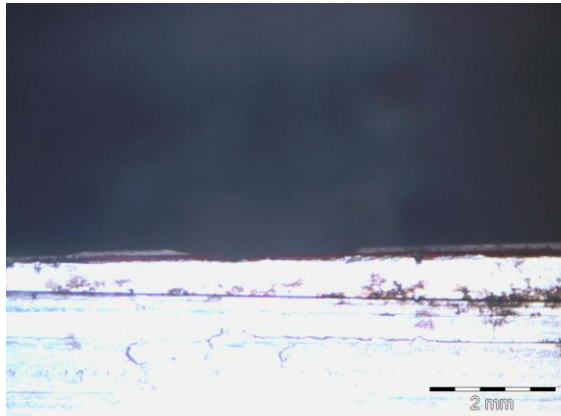
Figure 13. Underpaint corrosion measurement performed on specimen 1B (Ribeiro Filho, 2018).
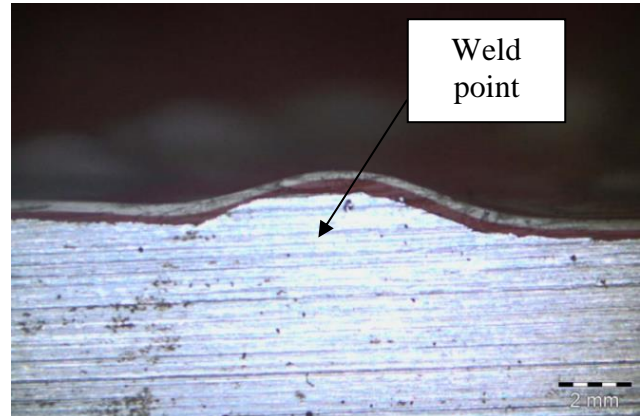
Figure 14. Cross section of specimen 6A (Ribeiro Filho, 2018).

3.2 Analyzing an example obtained from the field survey
To compare the results obtained in the laboratory with those of a real platform situation, a surface with intact paint, except for a single isolated region of mechanical damage throughout the film, was identified during the field visit. By radially removing the paint from this central point, the limits of corrosion exhibited a circumferential configuration, denoting that equal corrosion occurred in all directions, which can be verified by the existence of sandblasting steel without corrosion, exhibiting a Sa2½ pattern from the limits of the corrosion edge, which reached a radius of 21 mm (Figures 15 and 16).

Figure 15. Mechanical damage to the field paint (Ribeiro Filho, 2018).

Figure 16. Edge of the corroded area and the area without corrosion (Ribeiro Filho, 2018).

Considering that the exact date of the damage or the beginning of the exposure is not known and that, in the worst scenario, the damage occurred on the day of the platform shutdown, which represents a period of approximately three years (3x8760 h), the mean corrosion rate was $8x10^{-4}$ mm/h, which is considered close to the value found in the laboratory ($6.5x10^{-4}$ mm/h).

4. CONCLUSIONS

The results showed that once the substrate is exposed, the paint damage has a great impact on the underpaint corrosion.

The groups of specimens that were prepared with thin paint layers or whose paint was damaged without damaging the first coat maintained their ability to impart anticorrosion protection to the substrate, and the results were similar to those obtained for a specimen obtained in a field survey on the platform.

An exception was only observed for the group in which saline contamination was introduced into the substrate, which, in this case, showed that corrosion was favored by osmosis in the form of blistering.

Performing with the complete system without pathological manifestations, as well as preserving the quality and integrity of the paint, can ensure adequate anticorrosion protection. However, analyzing the results shows that the paint integrity had a decisive influence on the anticorrosion protection ability of the paint. In addition, considering the exposure time of 1550 h and the paint layers exhibiting no other pathological manifestations (porosity, corrosion attack, etc.), the paint integrity was also more important than the DFT. In situations where at least the first coat of paint was undamaged, the substrate was protected against corrosion when exposed to a salt chamber for 1550 h, even for the groups with thin paint thicknesses (<250 μm). When the damage reached the substrate, the rate of underpaint corrosion was similar in all cases.

5. ACKNOWLEDGMENTS

6. REFERENCES

Associação Brasileira de Normas Técnicas. (1983). *NBR 8094: Material metálico revestido e não revestido – Corrosão por exposição à névoa salina.* Rio de Janeiro.
Associação Brasileira de Normas Técnicas. (1997). *NBR 9583. Implantes para cirurgia - Ensaio não-destrutivo - Inspeção por líquido penetrante de implantes cirúrgico metálicos.* Rio de Janeiro.
Associação Brasileira de Normas Técnicas. (2005). *NBR 15239: Tratamento de superfícies de aço com ferramentas manuais e mecânicas.* Rio de Janeiro.
Associação Brasileira de Normas Técnicas. (2008). *NBR 10443: Tintas e vernizes – Determinação da espessura da película seca sobre superfícies rugosas – Método de ensaio.* Rio de Janeiro.
ASTM International. (2001). *B117-16: Standard Practice for Operating Salt Spray (Fog) Apparatus.* West Conshohocken, PA.
Chawla S. L, Gupta K. K. (1995), *"Materials selection for corrosion control"*, Materials Park, OH, ASM International.
Gentil, V. (2007), *"Corrosão",* 5. ed., LTC Livros Técnicos e Científicos Editora S.A., Rio de Janeiro.
ISO (1998). *ISO 8502-9: Preparation of steel substrates before application of paints and related products – Tests for the assessment of surface cleanliness – Part 9: Field method for the conductometric determination of water-soluble salts*. Geneva, Switzerland.
ISO (2006). *ISO 8502-6: Preparation of steel substrates before application of paints and related products – Tests for the assessment of surface cleanliness – Part 6: Extraction of soluble contaminants for analysis – The Bresle method*. Geneva, Switzerland. DOI: https://dx.doi.org/10.31030/9727591
ISO (2007). *ISO 8501-1: Preparation of steel substrates before application of paints and related products – Visual assessment of surface cleanliness –* Part 1: Rust grades and preparation grades of uncoated steel substrates and of steel substrates after overall removal of previous coatings. Geneva, Switzerland. DOI: https://dx.doi.org/10.31030/9871577
ISO (2012). *ISO 9227: Corrosion tests in artificial atmospheres – Salt spray tests*. 3rd ed. Geneva, Switzerland.
Jones, D. A. (1996), *"Principles and prevention of corrosion"*, 2nd ed., Prentice-Hall Inc, New York, University of Nevada, Nevada.
Nunes, L. D. P., Lobo, A. C. O. (2007), "*Pintura industrial na proteção anticorrosiva*", 3. ed., COPPE/UFRJ, Rio de Janeiro.
Ramanathan, L. V. (1988), "*Corrosão e seu controle*", Editora Hemus, Rio de Janeiro.
Ribeiro Filho, G. L. (2018), *"Estudo de patologias de pintura e corrosão atmosférica em plataforma de petróleo"*, Dissertação de Mestrado, Universidade Federal de Ouro Preto.
Silva, P. F. D. (1981), "*Introdução à corrosão e proteção de superfícies metálicas*", Imprensa Universitária da UFMG, Belo Horizonte.
Sosa, M. R., Pérez, T., Moo-Yam, V. M. J., Chávez, E. and Pérez-Quiroz, J. T. (2018), "*Análise da interface concreto-aço em corpos de prova expostos à intempérie e imersos em água do mar natural*", Revista ALCONPAT, 8 (1), pp. 16 – 29, DOI: http://dx.doi.org/10.21041/ra.v8i1.203
Wolynec S. (2003), *"Técnicas Eletroquímicas em Corrosão"*, Editora da Universidade de São Paulo, São Paulo.

Revista ALCONPAT

Development and analysis of a numerical model of the reinforced concrete expansion due to uniform corrosion

E. F. Felix[1]* [ID], R. Carrazedo[1] [ID], E. Possan[2] [ID], E. S. Ramos[1] [ID]

*Contact author: emerson.felipe.felix@gmail.com

ABSTRACT

This paper presents the modeling and analysis of the corrosion effects due to carbonation on reinforced concrete elements through a numerical model based on the Finite Element Method. In order to minimize corrosion damage, tools are required to understand the pathological manifestation on the mechanical behavior of reinforced concrete. It was found that depending on the reinforcement corrosion stage, the state of stress and deformation of the concrete element is compromised. Besides, results show the efficiency of the developed model and its applicability to the simulation of the mechanical behavior of reinforced concrete structures subjected to uniform corrosion.

Keywords: reinforced concrete; corrosion; numerical modeling; finite element method.

[1] University of São Paulo at São Carlos School of Engineering, Brasil.

[2] Universidade Federal da Integração Latino-Americana (UNILA), Brasil.

Responsible Associate Editor for this paper: Andrés Antonio Torres Acosta

Contribution of each author

In this work, E. F. Félix contributed with the activities of conceptualization, software development, modeling, results and discussion, writing and preparation of the original text; R. Carrazedo contributed with the funding acquisition, conceptualization, supervision, results and discussion, writing-reviewing and editing; E. Possan contributed with the supervision, writing and revision; and E. S. Ramos contributed with the activities of modeling, results and discussion.

Discussions and subsequent corrections to the publication

Any dispute, including the replies of the authors, will be published in the second issue of 2021 provided that the information is received before the closing of the first issue of 2021.

Desenvolvimento e análise de um modelo numérico da expansão do concreto armado sujeito à corrosão uniforme

RESUMO

Este trabalho apresenta a modelagem e análise dos efeitos da corrosão por carbonatação em elementos de concreto armado através de um modelo numérico baseado no Método dos Elementos Finitos. A fim de controlar e minimizar os danos associados à corrosão faz-se necessário deter ferramentas e conhecimento suficientes para entender os efeitos desta manifestação patológica sobre o comportamento mecânico do concreto armado. Diante dos resultados obtidos, constatou-se que a depender do nível de corrosão das armaduras, o elemento de concreto tem seu estado de tensão e deformação comprometido. Ademais, os resultados apontam a eficiência do modelo desenvolvido e a sua aplicabilidade frente à simulação do comportamento mecânico de estruturas de concreto armado sujeitas à corrosão uniforme.
Palavras-chave: concreto armado; corrosão; modelagem numérica; método dos elementos finitos.

Desarrollo y análisis de un modelo numérico de la expansión del hormigón armado por la corrosión uniforme

RESUMEN

Este trabajo presenta la modelización y análisis de los efectos de la corrosión por carbonatación en elementos de concreto reforzado a través de un modelo numérico basado en el Método de los Elementos Finitos. Para controlar y minimizar el daño asociado a la corrosión se hace necesario disponer de herramientas y conocimientos suficientes para comprender los efectos de esta manifestación patológica sobre el comportamiento mecánico del concreto reforzado. Ante los resultados obtenidos, se constató que, dependiendo del nivel de corrosión de las armaduras, el elemento de concreto tiene su estado de tensión y deformación alterado. Además, los resultados indican la eficiencia del modelo desarrollado y su aplicabilidad frente a la simulación del comportamiento mecánico del concreto reforzado con corrosión uniforme.
Palabras clave: concreto reforzado; corrosión; modelización numérica; método de los elementos finitos.

1. INTRODUCTION

The degradation of reinforced concrete structures due to the reinforcement corrosion is difficult to measure owned to the complexity of the physicochemical phenomenon and the multiple parameters involved (Mehta and Monteiro, 2014). From the mechanics of materials and structures point of view, the main effect of corrosion on reinforcement is loss of steel mass and, consequently, transformation of steel into corrosion products, or rust, as is commonly known. The volume of corrosion products is greater than steel, generating tensile stresses that leads to cracking and spalling concrete over time.

In general, concrete provide conditions to protect the reinforcement against corrosion, owning to the high alkalinity of the pore solution of concrete (pH between 12 and 13). However, this protection is lost as concrete is subjected to the different aggressive agents present in the atmosphere, i.e. chloride (Cl^-) and carbon dioxide (CO_2) ions (Gentil, 2011).

Depending on the concentration of the aggressive agent present in the atmosphere, the corrosive process can be classified as uniform or localized. Localized or pitting corrosion occurs when chloride ions cause an increase in the electrical conductivity of the concrete and attack the passivating layer that protects the reinforcement. In this case, corrosion is highly localized by pitting resulting in relatively minor mass loss, justifying the term "localized" used in its classification (Ribeiro et al., 2015).

The corrosive process is said to be uniform or by carbonation when the CO_2 content present in the atmosphere is predominant to that of chloride ions. Diffusion of CO_2 decreases the pH of the cement matrix (from approximately 13 or 12 to 9), which eliminates the passivation layer that surrounds the reinforcement, making it prone to corrosion (Mehta and Monteiro, 2014).

Usually, uniform corrosion is seen in low-quality concrete structures, where the concrete cover is insufficient to ensure protection, or in severe aggressive environments (Ribeiro et al., 2015). In these cases, corrosion leads to the formation of rust at the interface of steel and concrete, and these products occupy 3 to 10 more volume than initially (Helene,1986).

According to Andrade et al. (1993) and Ribeiro et al. (2015), the formation and development of corrosion products due to uniform corrosion depend on several environmental factors (ambient temperature, relative humidity, degree of environmental aggressiveness, CO_2, exposure content, among others), or on constructive factors (type of cement, water / cement ratio, type of steel, concrete cover, among others).

With the formation of corrosion products, internal stresses are developed at the interface between steel and concrete. As stresses increase, surpassing concrete tensile strength, micro cracks appear in the concrete matrix which increases in size and thickness as the pathological manifestation progress, spreading throughout the structural element until it spalls the concrete cover, affecting the durability and reducing the service life of the structure. The degradation process is presented in Figure 1.
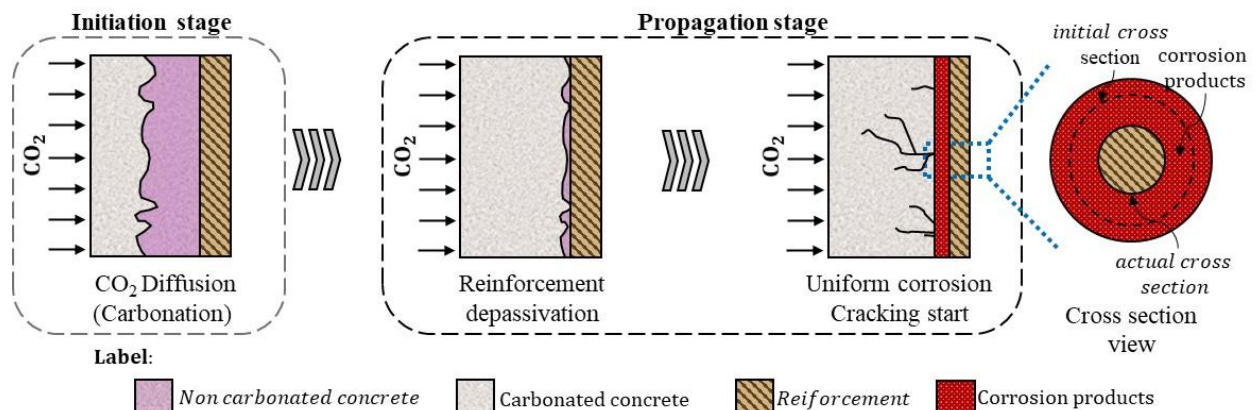

Figure 1. Corrosion development in concrete.

Development and analysis of a numerical model of the reinforced concrete expansion due uniform corrosion
Felix, E. F., Carrazedo, R., Possan, E., Ramos, E. S.

In order to minimize the effects of corrosion it is necessary to understand the initiation and propagation stages of the corrosive process, enabling the reduction of its incidence and, in advanced cases, the repair and / or restoration of the structures in order to increase their useful life, and reducing risks to its users.

Several experimental assessments have been carried out for the study of corrosion and its effects on the mechanical behavior of reinforced concrete, such as Molina et al. (1993), Almusallam (2001), Graeff (2007) and Zhu (2014), which resulted in relevant findings in the subject. However, three important limitations are pointed out by the researchers: (i) the difficulty of studying separately the different factors that influence the corrosion process; (ii) high costs and (iii) time required for experimental testing.

Several numerical tools were developed with the advancement in technology, for example, the Boundary Element Method (BEM), the Finite Element Method (FEM), Artificial Neural Networks (ANN), among others, leading to creative ways to solve some numerical problems, since these tools may help out to overcome those limits.

Hansen and Saouma (1999), Maruya et al. (2003) and Bhargava et al. (2005) used several numerical tools for an automated resolution of mathematical equations related to the corrosion mechanisms and to analyze the effects of corrosion and its propagation process.

Similar procedures were adopted by Isgor and Razaqpur (2006), Xu et al. (2009), Du and Jin (2014), Ožbolt et al. (2014) and Paul and Zijl (2016), solving the corrosion chemical and mechanical problem in reinforced concrete structures by FEM.

Thus, the present work proposes a numerical model developed with the Positional Finite Element Method (Positional FEM) for the study of corrosion and its effects. The proposed model enables the simulation of reinforced concrete expansion due to uniform corrosion and, in particular, the formation of corrosion products.

2. CONCRETE EXPANSION MODEL DUE TO CORROSION

2.1 Mechanical model

In order to simulate the expansion of reinforced concrete structures due to uniform corrosion, especially the formation of corrosion products, a numerical tool based on the Positional Finite Element Method was developed. The Fortran code combines a few analytical formulations to evaluate representative corrosion parameters. The mechanical behavior of the reinforced concrete is evaluated by a formulation based on the Positional Finite Element Method for composite solids, initially developed by Vanalli et at. (2008) and recently extended by Paccola e Coda (2016), in which the nodal parameters are the positions, and the deformations are related to the initial position of the body. Green strain measure and Saint-Venant-Kirchhoff constitutive law are employed.
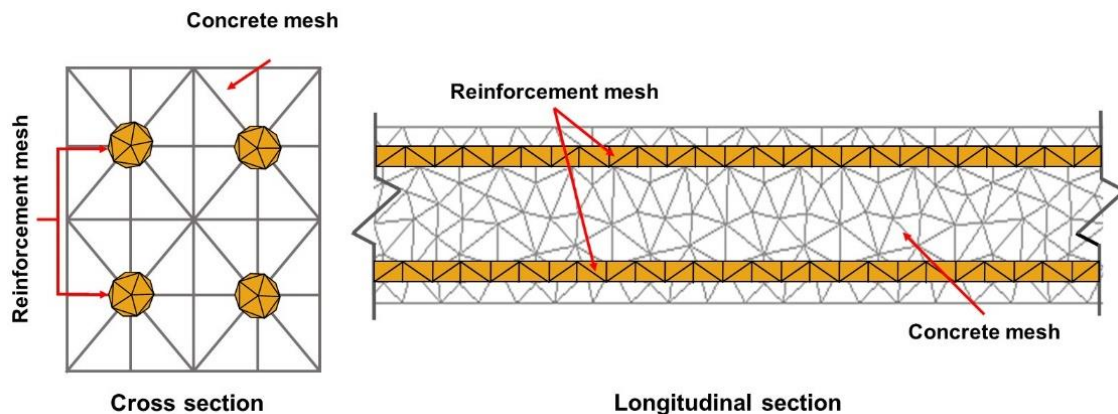

Figure 2. Example of discretization of a reinforced concrete beam cross and longitudinal sections.

Reinforced concrete is discretized considering the concrete and reinforcement matrix (Figure 2). Both the concrete matrix and the reinforcements are represented by means of flat triangular two-dimensional elements, the reinforcement mesh being coupled to the concrete matrix by means of the drawing technique, described in Vanalli et al. (2008) and Paccola and Coda (2016). In this case, a perfect adhesion between the particle and the matrix occurs, making the use of particle elements do not increase the degrees of freedom of the system. All the degrees of freedom of the particle elements are written based on the elements of the matrix.

In the sequence, the process used in this work to obtain the mechanical response of a problem via MEFP for reinforced concrete is briefly presented.

Considering conservative forces and the principle of the minimum stationary potential energy for the solution of the geometric nonlinear problem, the total potential energy of a particulate compound solid is described in equation (1).

$$\Pi = \int_{V_0^m} \mathbf{u}_e(E)dV_0{}^m + \int_{V_0^p} \Theta(E_p)dV_0{}^p - F \cdot Y \tag{1}$$

in which Θ is the specific strain energy of the particle elements, u_e is the specific strain energy of the matrix elements, F is the vector of conservative external forces, Y is the vector of nodal positions, E_p is the Green-Lagrange strain related to the particle elements, E is the Green-Lagrange strain related to the matrix elements, both evaluated by Equation (2), and $V_0{}^p$ e $V_0{}^m$ are the initial particle and matrix volumes, respectively.

$$E_{ij} = \frac{1}{2}(C_{ij} - \delta_{ij}) \tag{2}$$

where E_{ij} is the elastic Green-Lagrange strain, C_{ij} is the Cauchy-Green stretch tensor, and δ_{ij} is the Kronecker delta.

As the variation of the total potential energy is zero in the equilibrium, the problem is resumed to find the current nodal position vector, as presented in Equation (3).

$$\delta\Pi = \left(\int_{V_0^m} S : \frac{\partial E}{\partial Y}dV_0{}^m + \int_{V_0^p} S_p : \frac{\partial E_p}{\partial Y}dV_0{}^p - F \right) \cdot \delta Y \tag{3}$$

in which S is the second Piola-Kirchhoff stress developed in the elastic matrix, and S_p is is the second Piola-Kirchhoff stress developed in the particle elements. Since the problem is nonlinear, solution of Equation (3) is obtained by the Newton-Raphson process, over the unbalanced or residue vector g, as shown in Equation (4).

$$g(Y) = \left(\int_{V_0^m} S : \frac{\partial E}{\partial Y}dV_0{}^m + \int_{V_0^p} S_p : \frac{\partial E_p}{\partial Y}dV_0{}^p \right) - F = (F_{int}^m + F_{int}^p) - F = 0 \tag{4}$$

where F_{int}^m is the internal force portion of the matrix elements and F_{int}^p is the internal force portion of the particle elements. Equation (4) is expanded by a Taylor series, as described in Equation (5).

$$g(Y) \cong g(Y_0) + \frac{\partial g}{\partial Y}\Big|_{Y_0} \cdot \Delta Y = g(Y_0) + H \cdot \Delta Y = 0 \qquad (5)$$

in which Y is current trial position, and H is the Hessian matrix. H is decomposed into two matrices, one referred to the stiffness of the matrix elements (H_m), and another referred to the stiffness of the particle elements (H_p), as described in Equation (6).

$$H = \left\{ \left(\frac{\partial E}{\partial Y} : \frac{\partial^2 u_e}{\partial E \partial E} : \frac{\partial E}{\partial Y} + S : \frac{\partial^2 E}{\partial Y \partial Y} \right) + \left(\frac{\partial E_p}{\partial Y} : \frac{\partial^2 \Theta}{\partial E_p \partial E_p} : \frac{\partial E_p}{\partial Y} + S_p : \frac{\partial^2 E_p}{\partial Y \partial Y} \right) \right\} \qquad (6)$$
$$= H_m + H_f$$

The nonlinear system solution presented in Equation (5) by the Newton-Raphson method provides the correction of the trial position ($Y = Y_0 + \Delta Y$). Correction to trial position is applied until a convergence criterion such as $|\Delta Y|/|X|$ is achieved. Notice that X is the vector of the nodal positions of the initial configuration.
For further details, the reader is invited to consult in Paccola and Coda (2016) and Coda (2018).

2.2 Corrosion modeling

Understanding how corrosion products are developed and distributed around the reinforcement enables the development of models and tools that can describe the strains and stresses that arise from corrosion progress. These models assist in studies concerning the effects of corrosion on the mechanical behavior of concrete, durability and useful life of these structures.
Over the past few years, some models have been proposed to describe the distribution of rust around the reinforcement, i.e., Liu and Weyers (1998), Yuan and Ji (2009), Balafas and Burgoyne (2010) and Kiani and Shodja (2011). These models are divided into linear and non-linear, as shown in Figure 3.
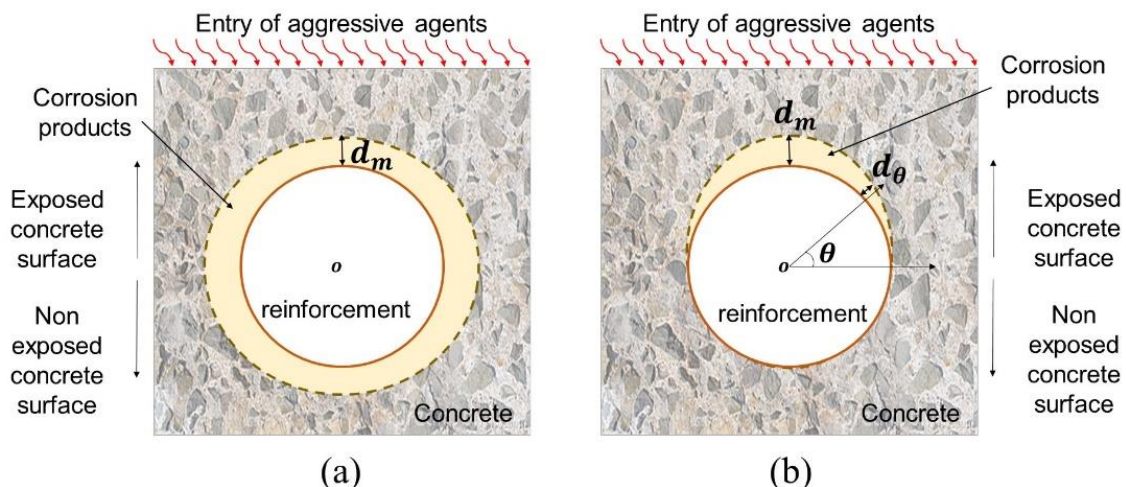
Figure 3. Rust formation profile: (a) linear e (b) non linear.

Thus, considering that the carbonation induced corrosion develops uniformly throughout the reinforcement, the model by Kiani and Shodja (2011) is used in this work to represent the corrosion progress.

Kiani and Shodja (2011) developed a linear model for the formation of rust in reinforced concrete structures, fitting experimental data from cylindrical reinforced concrete specimens of known diameter and physical properties (see Figure 4).
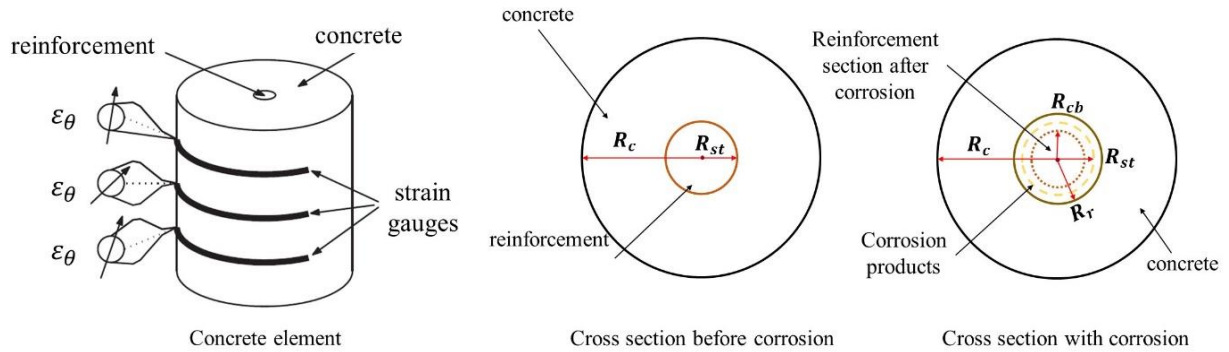
Figure 4. Model schematics of Kiani and Shodja (2011).

The model by Kiani and Shodja (2011) requires the evaluation of the reduced radius of the reinforcement due to corrosion (R_{cb}) and the radius of the rust front (R_r), which can be obtained in (7) and (8) respectively. It is also required to calculate the volume of the produced rust, according to (9), and the volume of consumed steel, according to (10).

$$R_{cb} = \sqrt{R_{st}^2 - \frac{V_s}{\pi}} \tag{7}$$

$$R_r = \sqrt{R_{cb}^2 + \frac{V_r}{\pi}} \tag{8}$$

$$V_r(t) = \frac{\alpha}{\rho_{st}} \sqrt{\int_0^t 2 \times 6{,}78 \times 10^{-10} \pi . R_{st} . i_{corr} dt} \tag{9}$$

$$V_s(t) = \frac{r_m}{\rho_{st}} \sqrt{\int_0^t 2 \times 6{,}78 \times 10^{-10} \pi . R_{st} . i_{corr} dt} \tag{10}$$

where R_{st} is the initial radius of the reinforcement (in m), α is the ratio of steel density of steel to the corrosion products density, ρ_{st} the steel density (in kg/m³), r_m the ratio of iron mass to the molecular mass of corrosion products, t (in s) is the time parameter, measured from the instant the reinforcement is depassivated and i_{corr} the natural corrosion current density (in A/m²), given by (11).

$$i_{corr}(t_p) = 0{,}85.10^{-2} . \left[\frac{37{,}8.\,(1 - a/c)^{-1{,}64}}{cob} \right] . t_p^{-0{,}29} \tag{11}$$

where a/c is the concrete water/cement ratio, t_p is the corrosion progression time, after the reinforcement is depassivated (in years), and *cob* is the thickness of concrete cover (in cm).
It is worth mentioning that the current density is constantly induced and controlled for laboratory assessment of accelerated corrosion. In this case, the density is known and Equation (11) is not employed.

2.3   Coupling the models
Considering that the cross section of a reinforced concrete structural element is represented by a particulate composite element, as shown in Figure 5, the expansion of the concrete cover due to the formation of corrosion products is simulated through the expansion of the particle element, since the reinforcement is perfectly adhered to the concrete matrix (imposed by the coupling technique).
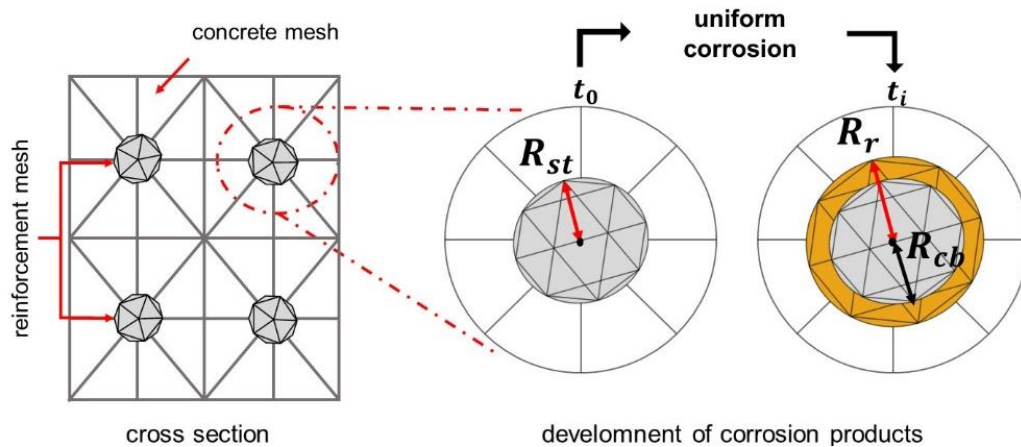
Figure 5. Representation of uniform corrosion via FEM.

In order to the reinforcement expansion consistently corresponds to the expansion caused by the corrosion products (ε_r) the expansion of the particle element is determined by (12), according to Green's strain.

$$\varepsilon_r = \frac{1}{2} \frac{\left(R_r^2 - R_{st}^2 \right)}{R_{st}^2} \tag{12}$$

However, after corrosion begins, it can be seen in Figure 5 and Equation (12) that the particle size will represent both reinforcement and corrosion products. Thus, the particle Young's modulus is corrected so the effects of reduction of steel are considered. It is then considered that the value of the particle Young's modulus is given by Equation (13):

$$E_p(t) = E_p(0)\frac{R_{cb}}{R_{st}} + E_r\frac{(R_r - R_{cb})}{R_{st}} \tag{13}$$

where $E_p(0)$ is the initial particle Young's modulus (uncorroded reinforcement), $E_p(t)$ is the particle Young's modulus at the instant t, E_r is the rust Young's modulus, R_{st} is the rebar initial radius, R_{cb} is the remaining rebar radius and R_r is the rust radius.

Finally, an additive decomposition of the Green strain is used to compose the concrete expansion due to formation of corrosion products, following Equation (14). This decomposition is possible since only small and moderate deformations are considered.

$$E_{ij} = \frac{1}{2}\left(C_{ij} - \delta_{ij}\right) - \varepsilon_r\delta_{ij} \tag{14}$$

where E_{ij} represents the elastic portion of the deformation and ε_r is the deformation of the particle (reinforcement) due to uniform corrosion for each of the main directions.

More details about the developed model, either of the formulation or of its applicability, can be obtained in Felix (2018).

3. RESULTS

Initially, two numerical simulations are presented referring to laboratory tests of concrete elements submitted to accelerated corrosion. Then, uniform corrosion on a reinforced concrete structure are analyzed using the model developed. The analysis was performed considering two environments, laboratory (accelerated corrosion) and urban (natural corrosion).

3.1   Performance analysis and model validation – Example 1

To demonstrate the efficiency of the model developed via MEFP to represent the expansion of concrete due to uniform corrosion, and especially, the formation of corrosion products, the modeling of a reinforced concrete plate under accelerated uniform corrosion is initially presented, which was experimentally analyzed by Nguyen et al. (2007).
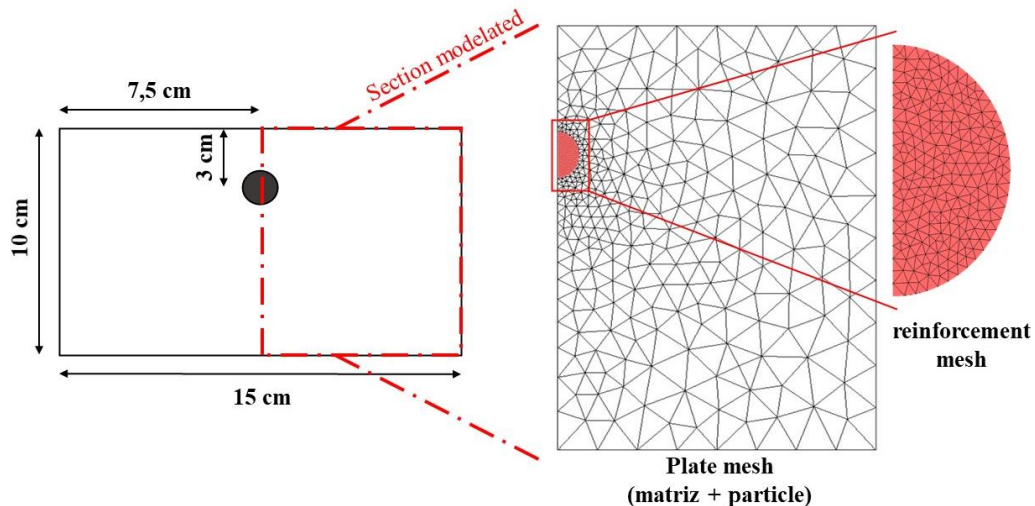
Figure 6. First example geometry and discretization

The plate contains a reinforcement with a diameter of 10 mm located in the central region, as shown in Figure 6, and was produced with concrete with compressive strength of 39 MPa and steel with a proportional limit of 500 MPa.

To achieve the accelerated corrosion test, Nguyen et al. (2007) subjected the reinforced concrete plate, after a 28-day wet cure, to a current with a constant density of $100 \, \mu A / cm^2$ for 92 hours. For numerical modeling, only half of the concrete plate was simulated (see Figure 6), due to symmetry of the problem. The plate was discretized by means of a particulate composite element, being used 680 triangular finite elements for the representation of the concrete matrix and 826 triangular finite elements for the discretization of the reinforcement.

Table 1 shows the parameters applied to model the problem, which were extracted from Nguyen et al. (2007).

Table 1. Input parameters for the corrosion simulation.

Parameter	Value	Unity
Steel density	7860	kg/m³
Valence	2	-
Density ratio of steel and corrosion products	3.7	-
Corrosion products, Young's modulus	0.15	GPa
Atomic mass of steel	55.84	-
Expansion volume ratio of corrosion products	3.7	-

It was adopted Young's modulus of 25 GPa and Poisson ratio of 0.2 for concrete, and Young's modulus of 210 GPa and Poisson ratio of 0.3 for steel.

Figure 7a presents the strain measured in the plate upper region, comparing the results obtained by the numerical simulation and by the experimental program of Nguyen et al. (2007).
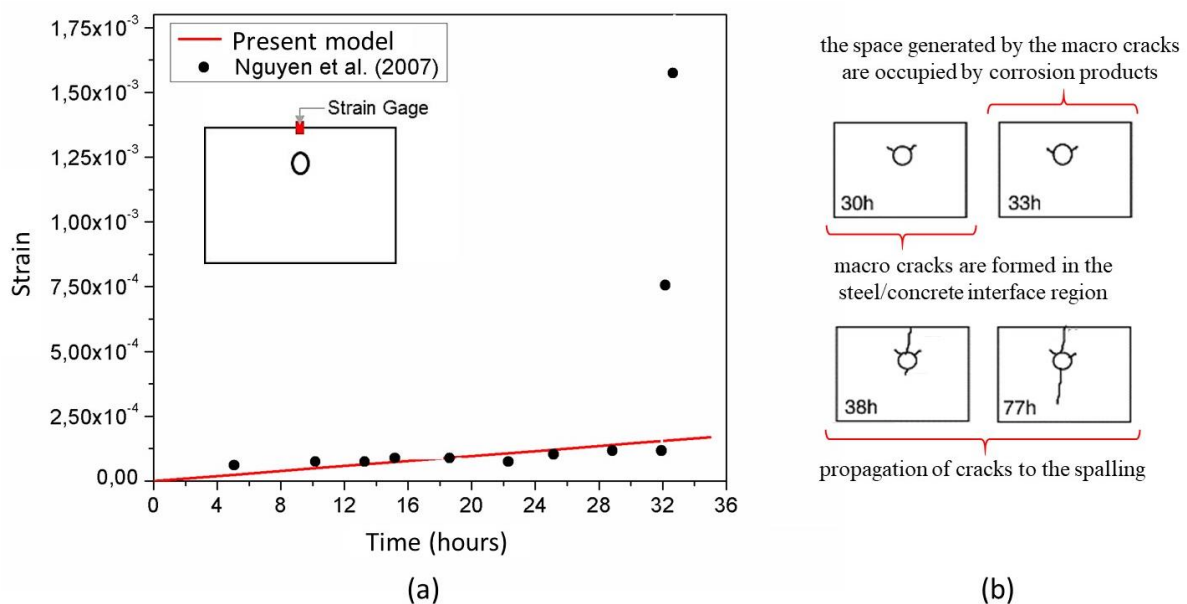
Figure 7. (a) Strain development and (b) Cracking evolution by Nguyen et al. (2007).

Figure 7.a shows that the numerical results consistently represent the experimental evaluation of the concrete expansion due to uniform corrosion, presenting an average absolute deviation of 4.12%. Notice that, after 30 hours, Nguyen et al. (2007) found a sudden increase in strain, which the numerical model was unable to represent, due to macro cracks formed in the interface of steel and

concrete – see Figure 7.b. This behavior cannot be simulated by the proposed model since only elastic strains are considered so far.

Figure 8 shows the horizontal and vertical displacements of the concrete slab after 15 and 30 hours of accelerated corrosion. One may notice that, only after 30 hours, significant deformations are observed on the surface.
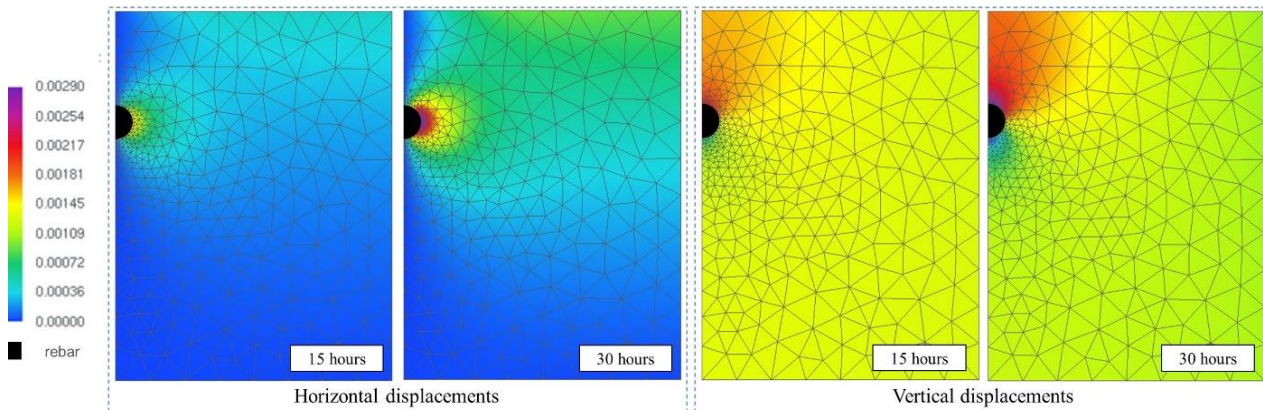
Figure 8. Displacement color maps (cm)
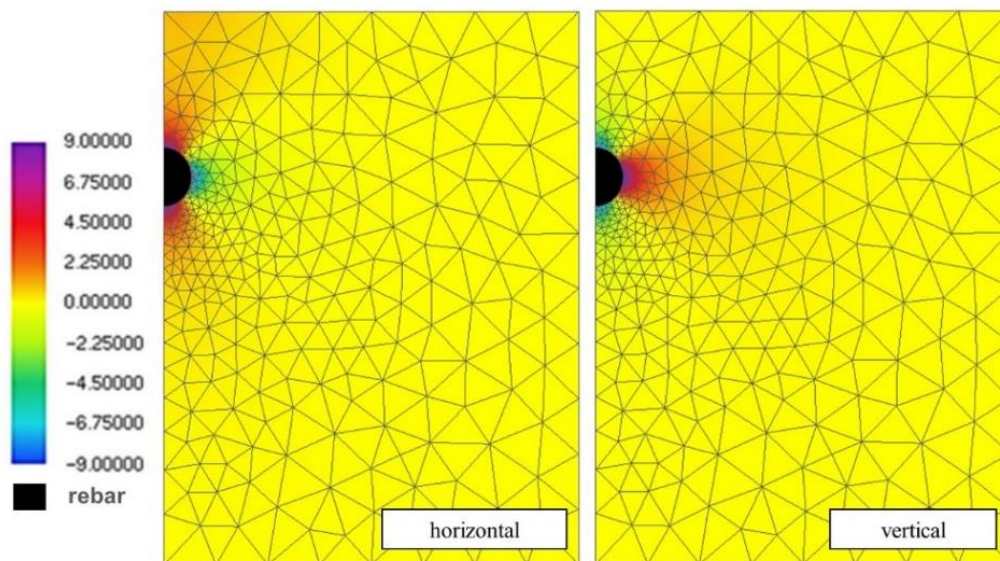
Figure 9. Stress color maps (MPa).

Figure 9 shows the stress distribution in the horizontal and vertical directions after 30 hours of accelerated corrosion. As expected, it is possible to observe that the tensile stresses present values above 3 MPa, corresponding to the tensile strength of the concrete, which would imply the development of cracks and corroborating the conclusions of Nguyen et al. (2007).

Thus, the results demonstrate that the model consistently represents the uniform corrosion expansive effects.

3.2   Performance analysis and model validation – Example 2

In the second example, a reinforced concrete beam is simulated, based in the experimental assessment of Graeff (2007), see Figure 10. The simply supported beam of length 130 cm has a rectangular cross section 7 cm wide and 14 cm high, with a span of 120 cm between supports, see Figure 10 for more details.

Development and analysis of a numerical model of the reinforced concrete expansion due uniform corrosion
Felix, E. F., Carrazedo, R., Possan, E., Ramos, E. S.
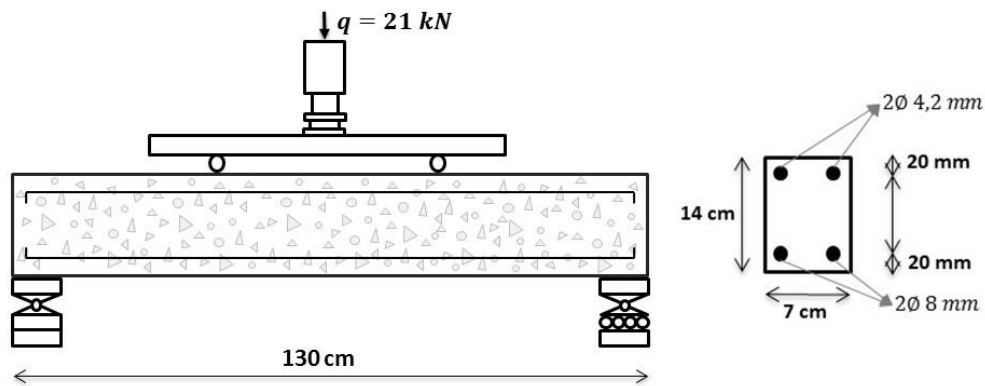
Figure 10. Reinforced concrete beam details.

The finite element mesh is composed of 134 nodes and 34 triangular elements of cubic approximation for the concrete matrix, and 340 triangular elements for the rebars. The following material properties are adopted for concrete: Young modulus of 2600.0 kN/cm², compressive strength of 2.5 kN/cm², tensile strength of 0.179 kN/cm² and Poisson's ratio of 0.2. Young modulus of 210 MPa and tensile strength of 500 MPa are adopted for rebars. Graeff (2007) has also considered the nonlinear behavior of concrete, as well as the effects of corrosion, such loss of steel section and loss of steel-concrete bond.
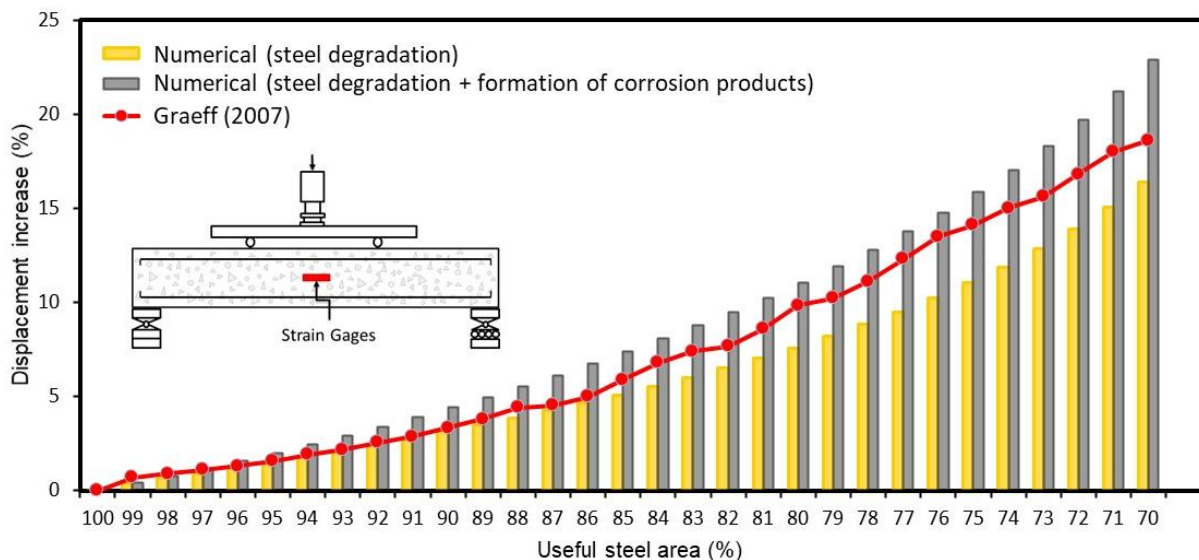
Figure 11. Comparison of beam displacement.

In this work, the simulation of corrosion was done considering two situations, one in which the effects of corrosion are related only to the loss of the steel section, and another in which the corrosion causes the loss of the steel section and the expansion of the concrete, due to the formation of corrosion products. By means of Figure 11, the results achieved with this work are compared with those determined in Graeff (2007). It can be seen from Figure 11 that the difference between the results obtained by the numerical model presented in this work (in the two simulations) and those obtained by Graeff (2007) is increasing, as the degradation of the reinforcements increases. An explanation for such a difference is because Graeff (2007) adopted in his model a nonlinear constitutive law for concrete and steel.

However, it is observed that all the curves have similar behavior in relation to displacements of the structure and that considering the initial period of corrosion (up to the moment when the reinforcement loses 15% of useful area), for cases in which the materials are still they work in a linear-elastic regime, the implemented model presents equivalent results to those of Graeff (2007).

By means of Figure 11 it is possible to see that the combined consideration of more than one corrosion degradation effect results in greater beam displacements and that, when considering the expansion of the concrete due to the formation of corrosion products, the Loss of concrete's mechanical capacity becomes greater with the advance of corrosion. This fact demonstrates the importance of considering this phenomenon in modeling the corrosion of concrete structures.

3.3   Analysis of mechanical behavior of corroded reinforced concrete beam
Third example consists of a clamped reinforced concrete beam under uniform corrosion. The objective of this analysis is to evaluate the effect of the corrosion on the displacement of the concrete structure, as well on the stress distribution. The beam geometry, dimensions, loading and boundary conditions are shown in Figure 12.
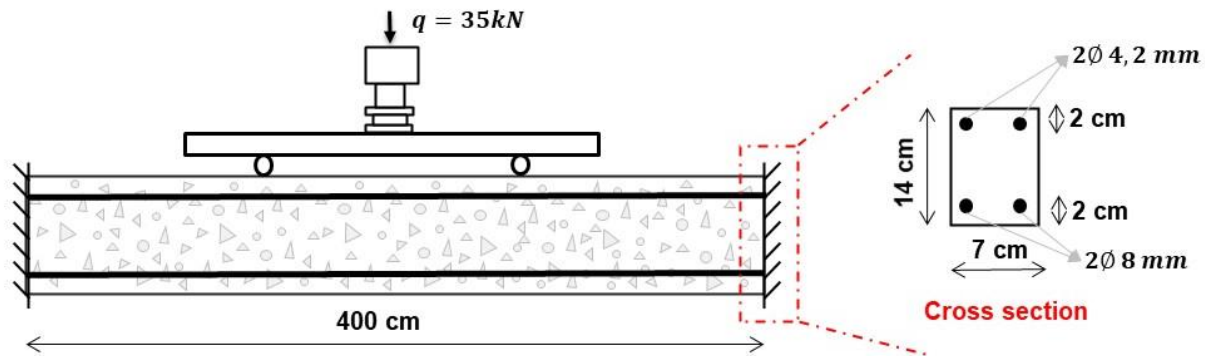
Figure 12. Beam geometry, dimensions and boundary conditions.

Corrosion is initially imposed rapidly, using a constant current of $100\,\mu A\,/\,cm^2$. Next, the effects of simulated corrosion in a laboratory environment (accelerated corrosion) are evaluated, comparing it with the effects of natural corrosion, by means of a time-varying current, determined in accordance with equation (11). The parameters used in the formulation regarding the formation of the corrosion products, whose data were extracted from Nguyen et al. (2007) are described in Table 1.

The discretization of the finite element mesh of the reinforced concrete beam was made with 2230 knots and 468 triangular elements for the representation of the concrete matrix and with 952 triangular elements (particles) for the representation of the reinforcement. Regarding the properties of the materials, the concrete has a modulus of elasticity of $2600.0\,kN\,/\,cm^2$, compressive strength of $2.5\,kN\,/\,cm^2$, tensile strength of $0.179\,kN\,/\,cm^2$ and Poisson's ratio of 0.2. The reinforcements, in turn, have a modulus of elasticity of $21000\,kN\,/\,cm^2$ and tensile strength of $50\,kN\,/\,cm^2$.

Figures 13.a and 13.b present the results referring to vertical displacement and longitudinal tension (for three different beam regions), considering the chemical-mechanical stresses (imposed by corrosion) and the stresses from the cargo.

It is noted in Figure 13.a that after 50 hours of accelerated corrosion, the structure experiences an increase in displacement of 0.26 mm (for low) for a point located in the lower part of the center of the beam (point "I"), as for a point located in the upper part of the center of the beam (point "S"), the increase was 0.14 mm, almost half of the value observed in the lower point.
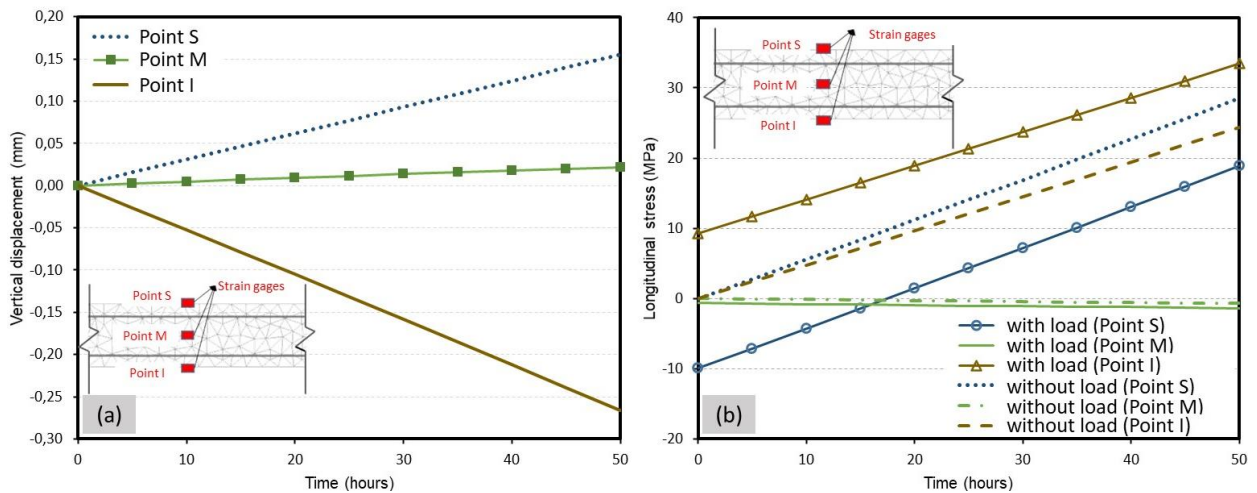
Figure 13. (a) Vertical displacement and (b) Longitudinal stresses.

The results presented in Figure 13.b demonstrate the influence of corrosion on the beam stress field under corrosion when considering the application of an external load. It is observed for the case of only corrosion (without loading) that the stresses at points "S" and "I" are always tensile (regardless of the propagation time), as pointed out by Balafas and Burgoyne (2010). However, it is noted that in the presence of an external cargo, the voltage field begins to have behavior controlled by the level of corrosion of the armatures. For example, the "S" point, located at the top of the beam, has its state of compression stress altered for traction after 15 hours of accelerated corrosion.

In other words, it has been verified that there is a significant influence of corrosion on the stress fields of reinforced concrete beams in service (with cargo). This influence has secondary effects that corroborate with the reduction of the useful life of the structures, for example, cracking of the covering concrete. The cracking state of a reinforced concrete element is highly dependent on its stress state and, consequently, if corrosion alters the stress field of a structural element, it can modify and / or accelerate its rupture mechanisms.

Figure 14.a shows the deformed configuration of the beam considering three different stress configurations: (i) only corrosion; (ii) only cargo; and (iii) joint action of cargo and corrosion. It is noted that in the case where the beam stresses are exclusively the result of corrosion, the entire structural element is stressed, due to the formation of corrosion products. It is still observed that the displacements of the beam in the case of corrosion and external loading can be described by overlapping mechanical (due to external loading) and chemical-mechanical stresses (resulting from corrosion).

Finally, Figure 14.b presents the results for the vertical displacement of the reinforced concrete beam, considering only natural corrosion.

Based on the results of the simulation of natural corrosion, which are presented in Figure 14.b, it was verified that the displacement of the "I" point after 50 years of natural corrosion is 0.47 mm, 79% greater than the displacement observed after 50 hours of accelerated corrosion.
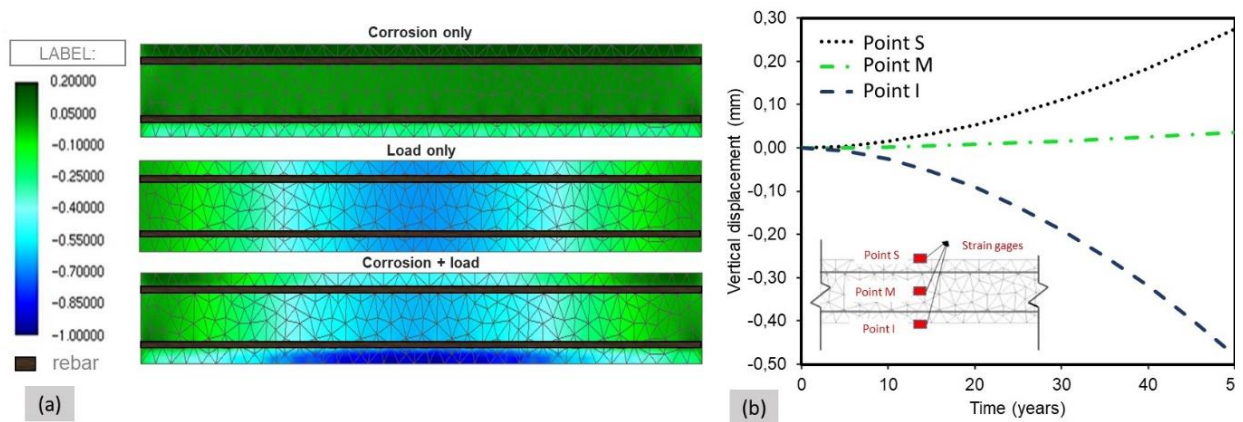
Figure 14. (a) Vertical beam displacement: (a) for 50 years e (b) at the time (mm).

4. CONCLUSIONS

The proposed model, based on the Positional Finite Element Method (Positional FEM), consistently represents the expansion of concrete due to the formation of corrosion products. The model has been validated, given the numerical simulations carried out, allowing to conclude that:

- Corrosion can significantly modify the stress distribution of a structural element, even imposing that a previous compressed region become tensioned;
- An external load does not change the fact that an element undergoes corrosion. The effects overlap, and the superposition tends to be meaningful;
- Displacements can be described by superposition of the mechanical loads and formation of corrosion products, before cracking;
- Significant differences are observed in the mechanical behavior of a structural element when exposed to natural or accelerated corrosion, and no correlation are directly found;
- As long as damage is not relevant, small strain may be assumed, and the superposition principle can be extended to evaluate the corrosion in reinforced concrete structures.

Finally, we conclude that the proposed model is a viable and efficient alternative for the simulation of reinforce concrete elements under uniform corrosion.

5. ACKNOWLEDGMENT

6. REFERENCES

Almusallam, A. A. (2001), *Effect of degree of corrosion on the properties of reinforcing steel bars. Construction and Building Materials.* 15(8):361–368. https://doi.org/10.1016/S0950-0618(01)00009-5

Andrade, C., Alonso, C., Molina, F. J. (1993), *Cover cracking as a function of bar corrosion: Part 1 Experimental test. Materials and Structures.* 26:453–464. https://doi.org/10.1007/BF02472805

Balafas, I., Burgoyne, C. J. (2011), *Modeling the structural effects of rust in concrete cover. Journal of Engineering Mechanics.* Journal of Engineering Mechanics. 137(3):175–185. https://doi.org/10.1061/(ASCE)EM.1943-7889.0000215

Bhargava, K., Ghosh, A. K., Mori, Y., Ramanujam, S. (2005), *Modeling of time to corrosion-induced cover cracking in reinforced concrete structures. Cement and Concrete Research.* 35 (11):2203–2218. https://doi.org/10.1016/j.cemconres.2005.06.007

Coda, H. B. (2018), *"O método dos elementos finitos posicional: sólidos e estruturas – Não linearidade geométrica e dinâmica"*. Publisher: EESC-USP, Place of publication: São Carlos, SP, p. 284. ISBN: 9788580230680

Du, X., Jin, L. (2014), *Meso-scale numerical investigation on cracking of cover concrete induced by corrosion of reinforcing steel.* Engineering Failure Analysis. 39:21–33. https://doi.org/10.1016/j.engfailanal.2014.01.011

Felix, E. F. (2018), *"Modelagem da deformação do concreto armado devido à formação dos produtos de corrosão"*. Master Thesis, Escola de Engenharia de São Carlos/USP, São Carlos.

Gentil, V. (2011), *"Corrosão"*. Editora LCT, 6º edição, Rio de Janeiro, Brasil, p. 376.

Graeff, A. G. (2007), *"Avaliação experimental e modelagem dos efeitos estruturais da propagação da corrosão em elementos de concreto armado"*. Master Thesis, Universidade Federal do Rio Grande do Sul, Porto Alegre.

Hansen, E. J., Saouma, V. E. (1999), *Numerical simulation of reinforced concrete deterioration: Part 2-steel corrosion and concrete cracking.* ACI Materials Journal. 96:331–338. ISSN: 0889-325X.

Helene, P. (1986), *"Corrosão em armaduras para concreto armado"*. PINI, São Paulo, Brasil. p. 46.

Isgor, O. B., Razaqpur, A. G. (2006), *Modelling steel corrosion in concrete structures.* Materials and Structures. 39(3):291–302. https://doi.org/10.1007/s11527-005-9022-7

Jiang, L., Lin, B., Cai, Y. (2000), *A model for predicting carbonation of high-volume fly ash concrete.* Cement and Concrete Research. 30(5):699–702. https://doi.org/10.1016/S0008-8846(00)00227-1

Kiani, K., Shodja, H. M. (2011), *Prediction of the penetrated rust into the microcracks of concrete caused by reinforcement corrosion.* Applied Mathematical Modelling. 35(5):2529–2543. https://doi.org/10.1016/j.apm.2010.11.039

Liu, Y., Weyers, R. E. (1998), *Modeling the time-to-corrosion cracking in chloride contaminated reinforced concrete structures.* Materials Journal. 95(6):675–680.

Maruya, T., Hsu, K., Takeda, H., Tangtermsirikul, S. (2003), *Numerical modeling of steel corrosion in concrete structures due to chloride ion, oxygen and water movement.* Journal of Advanced Concrete Technology. 1(2):147–160. https://doi.org/10.3151/jact.1.147

Mehta, P. K., Monteiro, P. J. M. (2014), *"Concreto: microestrutura, propriedades e materiais"*. Ibracon, São Paulo, Brasil, p. 751.

Molina, F. J., Alonso, C., Andrade, C. (1993), *Cover cracking as a function of bar corrosion: Part 2-Numerical model.* Materials and Structures. 26 :532–548. https://doi.org/10.1007/BF02472864

Nguyen, Q. T., Caré, S., Millard, A., Berthaud, Y. (2007), *Analyse de la fissuration du béton armé en corrosion accélérée.* Comptes Rendus Mecanique. 335(2): 99–104. https://doi.org/10.1016/j.crme.2007.01.005

Ožbolt, J., Oršanić, F., Balabanić, G. (2014), *Modeling pullout resistance of corroded reinforcement in concrete: Coupled three-dimensional finite element model.* Cement and Concrete Composites. 46:41–55. https://doi.org/10.1016/j.cemconcomp.2013.10.014

Paccola, R. R., Coda, H. B. (2016), *A direct FEM approach for particulate reinforced elastic solids.* Composite Structures. 45:235–251. https://doi.org/10.1016/j.compstruct.2016.01.062

Paul, S. C., Zijl, G. P. A. G. V. (2016), *Chloride-induced corrosion modelling of cracked reinforced SHCC.* Archives of Civil and Mechanical Engineering. 16(4):734–742. https://doi.org/10.1016/j.acme.2016.04.016

Ribeiro, D., Cunha, M., Helene, P. (2015), *"Corrosão em Estruturas de Concreto Armado: Teoria, Controle e Métodos de Análise"*. Elsevier Brasil, Campus, São Paulo, Brasil, p. 272.

Vanalli, L., Paccola, R. R., Coda, H. B. (2008), *A simply way to introduce fibers into FEM models.* Communications in Numerical Methods in Engineering. 24:585–603. https://doi.org/10.1002/cnm.983

Yuan, Y., Ji, Y. (2009), *Modeling corroded section configuration of steel bar in concrete structure.* Construction and Building Materials. 23(6):2461–2466. https://doi.org/10.1016/j.conbuildmat.2008.09.026

Zhu, W. (2014), "*Effect of corrosion on the mechanical properties of the corroded reinforcement and the residual structural performance of the corroded beams*", Doctoral Dissertation, Institut National des Sciences Appliquées de Toulouse (INSA de Toulouse).

Development and analysis of a numerical model of the reinforced concrete expansion due uniform corrosion
Felix, E. F., Carrazedo, R., Possan, E., Ramos, E. S.

Revista ALCONPAT

An analytical model for the design of corner combined footings

A. Luévanos Rojas[1]* , S. López Chavarría[1] , M. Medina Elizondo[1] ,
R. Sandoval Rivas[1] , O. M. Farías Montemayor [1]

*Contact author: arnulfol_2007@hotmail.com

DOI: https://doi.org/10.21041/ra.v10i3.432

ABSTRACT

This work shows an analytical model for the design of corner combined footings subjected to an axial load and two orthogonal flexural moments per each column. It considers the real pressure on the ground below of the footing, and the methodology is based on the principle that the integration of the shear force is the moment. The current design considers the maximum pressure at all contact points. This model is verified by equilibrium of shear forces and moments. The application of the model is presented by means of a numerical example. Therefore, the proposed model is the most appropriated, because it generates better quality control in the resources used.

Keywords: corner combined footings; analytical model for design; flexural moments; flexural shearing; punching shearing.

[1] Instituto de Investigaciones Multidisciplinarias, Universidad Autónoma de Coahuila, Torreón, Coahuila, México.

Responsible Associate Editor for this paper: Paulo Helene

Contribution of each author
In this work, the author Dr. Arnulfo Luévanos Rojas contributed to the original idea of the article, mathematical development of the new model and coordinated the work in general. The author Dr. Sandra López Chavarría contributed to the discussion of the results. The author Dr. Manuel Medina Elizondo contributed to the writing of the work. The author C. a Dr. Ricardo Sandoval Rivas contributed to the elaboration of the figures. The author C. a Dr. Oscar Mario Farías Montemayor contributed in the application of the proposed model.

Discussions and subsequent corrections to the publication
Any dispute, including the replies of the authors, will be published in the second issue of 2021 provided that the information is received before the closing of the first issue of 2021.

Un modelo analítico para el diseño de zapatas combinadas de esquina

RESUMEN

Este trabajo muestra un modelo analítico para el diseño de zapatas combinadas de esquina sometidas a una carga axial y dos momentos flexionantes ortogonales por cada columna. El modelo toma en cuenta la presión real del suelo debajo de la zapata, y la metodología se basa en el principio de que la integración de la fuerza de corte es el momento. El diseño actual considera la presión máxima en todos los puntos de contacto. Este modelo se verifica por equilibrio de fuerzas de corte y momentos. La aplicación del modelo se presenta por medio de un ejemplo numérico. Por lo tanto, el modelo propuesto es el más apropiado, ya que genera un mejor control de calidad en los recursos utilizados.
Palabras clave: zapatas combinadas de esquina; modelo analítico para diseño; momentos flexionantes; cortante por flexión; cortante por penetración.

Um modelo analítico para projeto de sapata de canto combinadas

RESUMO

Este trabalho apresenta um modelo analítico para o dimensionamento de sapatas angulares combinadas submetidas a uma carga axial e dois momentos fletores ortogonais para cada pilar que leva em consideração a pressão real do solo sob a sapata, e a metodologia é baseada no princípio de que a integração da força cortante é o momento. O projeto atual considera a pressão máxima em todos os pontos de contato. Este modelo é verificado pelo equilíbrio das forças de cisalhamento e momentos. A aplicação do modelo é apresentada por meio de um exemplo numérico. Portanto, o modelo proposto é o mais adequado, pois gera um melhor controle de qualidade dos recursos utilizados.
Palavras-chave: sapatas combinadas de canto; modelo analítico para projeto; momentos de flexão; cisalhamento por flexão; cisalhamento por punção.

An analytical model for the design of corner combined footings
Luévanos Rojas, A., López Chavarría, S., Medina Elizondo, M., Sandoval Rivas, R., Farías Montemayor, O. M.

1. INTRODUCTION

A foundation or more commonly called a base that is the element of an architectural structure that connects it to the ground, and that transfers the loads from the structure to the ground. Foundations are divided into two types, such as shallow and deep (Bowles, 2001; Das et al., 2006).
Five main types of shallow foundations for columns are: 1) strip footing; 2) spread or isolated footing; 3) combined footing supporting two or more columns; 4) strap or cantilever footing; 5) raft or mat foundations covering the whole foundation area (Bowles, 2001).
A combined footing is necessary to support a column located very close to the edge of a property line so as not to invade the adjacent property. The combined footing can be a uniform thickness slab or an inverted T-beam. If the slab type of the combined footing is used to support two or more columns (typically two), the slab must have a rectangular, trapezoidal or T-shaped form when one column is loaded more than the other (Kurian, 2005; Punmia et al., 2007; Varghese, 2009).
The ground pressure under a footing depends on the type of ground, the relative rigidity of the ground and the footing, and the depth of foundation at level of contact between footing and ground. Figure 1 shows the distribution of ground pressure under the footing according to the type of ground and the stiffness of the footing (Bowles, 2001).

|(a) Rigid footing on sandy ground|(b) Rigid footing on clay ground|(c) Flexible footing on sandy ground|(d) Flexible footing on clay ground|(e) Uniform distribution used in design|
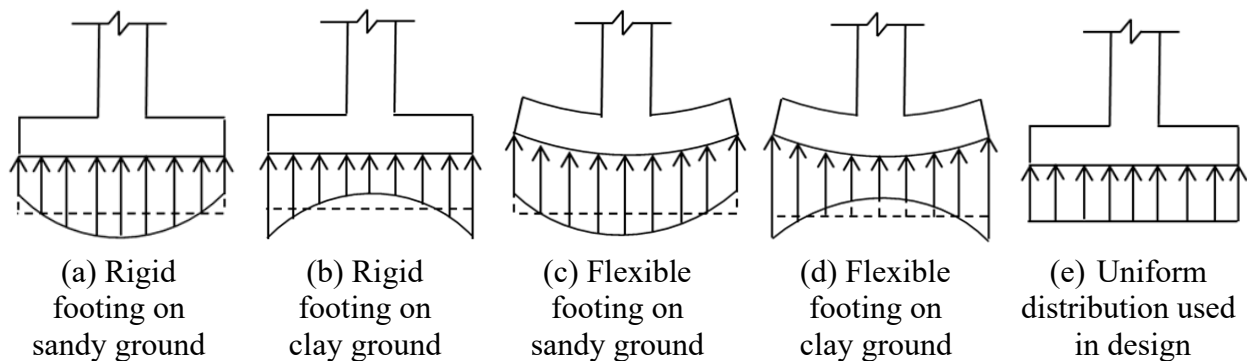
Figure 1. Soil pressure below of the footing

Studies on foundation structures and mathematical models for footings have been successfully investigated in various geotechnical engineering problems. The main contributions of various researchers in the last decade are: "Behavior of repeatedly loaded rectangular footings resting on reinforced sand" (El Sawwaf and Nazir, 2010); "Nonlinear vibration of hybrid composite plates on elastic foundations" (Chen et al., 2011); "Stochastic design charts for bearing capacity of strip footings" (Shahin and Cheung, 2011); "Modified particle swarm optimization for optimum design of spread footing and retaining wall" (Khajehzadeh et al., 2011); "Design of isolated footings of rectangular form using a new model" (Luévanos-Rojas et al., 2013); "Design of isolated footings of circular form using a new model" (Luévanos-Rojas, 2014a); "Design of boundary combined footings of rectangular shape using a new model" (Luévanos-Rojas, 2014b); "Determination of the ultimate limit states of shallow foundations using gene expression programming (GEP) approach" (Tahmasebi poor et al., 2015); "Design of boundary combined footings of trapezoidal form using a new model" (Luévanos-Rojas, 2015); "New iterative method to calculate base stress of footings under biaxial bending" (Aydogdu, 2016); "A comparative study for the design of rectangular and circular isolated footings using new models" (Luévanos-Rojas, 2016a); "Influence of footings stiffness on punching resistance" (Fillo et al., 2016); "A new model for the design of rectangular combined boundary footings with two restricted opposite sides" (Luévanos-Rojas, 2016b); "Structural design of isolated column footings" (Abdrabbo et al., 2016); "Optimal design for rectangular isolated footings using the real pressure on the ground" (Luévanos-Rojas et al.,

2017a); "Experimental and finite element analyses of footings of varying shapes on sand" (Anil et al., 2017); "A comparative study for design of boundary combined footings of trapezoidal and rectangular forms using new models" (Luévanos-Rojas et al., 2017b); "Performance of isolated and folded footings" (El-kady and Badrawi, 2017); "Analysis and Design of Various Types of Isolated Footings" (Balachandar and Narendra Prasad, 2017); "A new model for T-shaped combined footings Part II: Mathematical model for design" (Luévanos-Rojas et al., 2018); "Punching shear resistance of reinforced concrete footings: evaluation of design codes" (Santos et al., 2018); "Soil foundation effect on the vibration response of concrete foundations using mathematical model" (Dezhkam and Yaghfoori, 2018); "Nonlinearity analysis in studying shallow grid foundation" (Ibrahim et al., 2018); "Modeling for the strap combined footings Part II: Mathematical model for design" (Yáñez-Palafox et al., 2019); "Numerical method for analysis and design of isolated square footing under concentric loading" (Magade and Ingle, 2019).

The document related to this work is: "Optimal dimensioning for the corner combined footings" to obtain only the minimum area of the contact surface between the ground and the footing (López-Chavarría et al., 2017), but this document does not present the design of corner combined footings to obtain the effective depth (effective cant) and reinforcing steel.

This document shows an analytical model for the design of corner combined footings subjected to an axial load and two orthogonal flexural moments for each column, and the ground pressure on the footing is presented in terms of the effects generated by each column, and the methodology is based on the principle that the integration of the shear force is the moment. The current design considers the maximum pressure at all contact points, because the center of gravity of the footing coincides with the position of the force resulting from the loads. This model is verified by equilibrium of shear forces and moments. The main advantage of the proposed model is to present the moment, the flexural shearing and the punching shearing by mean of analytical equations. Therefore, the proposed model will be the most appropriate, since it generates a better quality control in the resources used (labor, materials, minor equipment, etc.), because it adjusts to the conditions of the real pressure on the ground.

2. FORMULATION OF THE PROPOSED MODEL

The critical sections for footings according to the code are (ACI 318S-14, 2014): 1) The moment is located on the face of the column; 2) The flexural shearing is located at a distance "d" from the face of the column; 3) The punching shearing is presented at a distance of "d/2" in both directions. The axial load and two orthogonal flexural moments (biaxial flexure) of each column applied to the corner combined footing are shown in Figure 2(a). The pressure below of the corner combined footing that varies linearly, and stress at each vertex of the footing is presented in Figure 2(b).
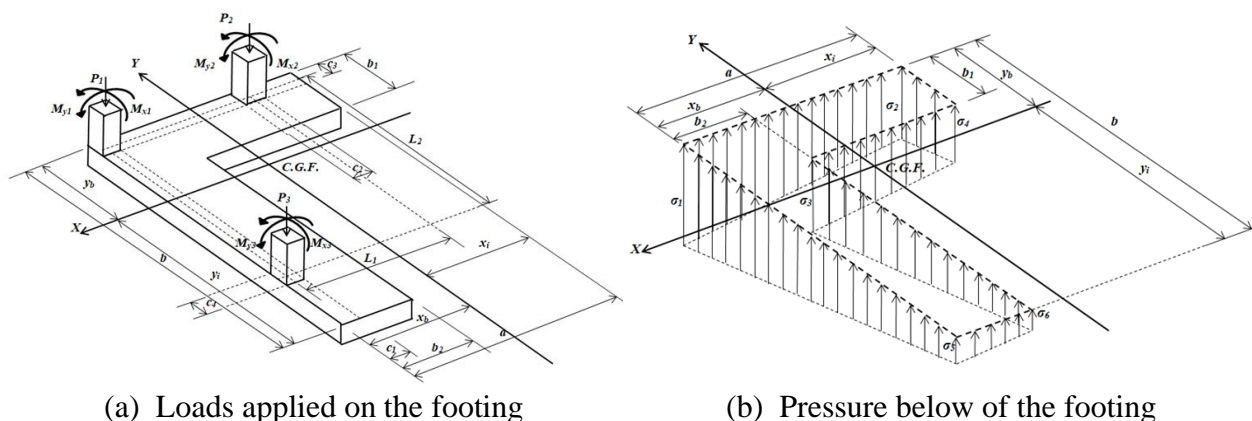
(a) Loads applied on the footing   (b) Pressure below of the footing
Figure 2. Corner combined footing

The stresses in the main direction ("X" and "Y" axes) are:

$$\sigma(x, y) = \frac{R}{A} + \frac{M_{xT}y}{I_x} + \frac{M_{yT}x}{I_y} \tag{1}$$

where: R, M_{xT}, M_{yT}, A, I_x, and I_y are shown in (López-Chavarría et al., 2017).
The stresses below of the column 2 ("X_2" and "Y_2" axes) are (see Figure 3):

$$\sigma_{P_2}(x, y) = \frac{P_2}{w_2 b_1} + \frac{12[M_{x2} + P_2(b_1 - c_3)/2]y}{w_2 b_1^{\,3}} + \frac{12 M_{y2} x}{w_2^{\,3} b_1} \tag{2}$$

The stresses below of the column 3 ("X_3" and "Y_3" axes) are (see Figure 3):

$$\sigma_{P_3}(x, y) = \frac{P_3}{w_3 b_2} + \frac{12[M_{y3} + P_3(b_2 - c_1)/2]x}{w_3 b_2^{\,3}} + \frac{12 M_{x3} y}{w_3^{\,3} b_2} \tag{3}$$

where: w_2 and w_3 are the widths of the analysis surface in the columns 2 and 3: $w_2 = c_2 + d$, $w_3 = c_4 + d$.

2.1 Flexural shearing and flexural moments

The critical sections for flexural moments are presented on the axes: a'-a', b'-b', c'-c', d'-d', e'-e', f'-f', g'-g', h'-h', i'-i' and j'-j' (see Figure 3). The critical sections for flexural shearing are presented on the axes: k'-k', l'-l', m'-m', n'-n', o'-o', p'-p', q'-q' and r'-r' (see Figure 4).
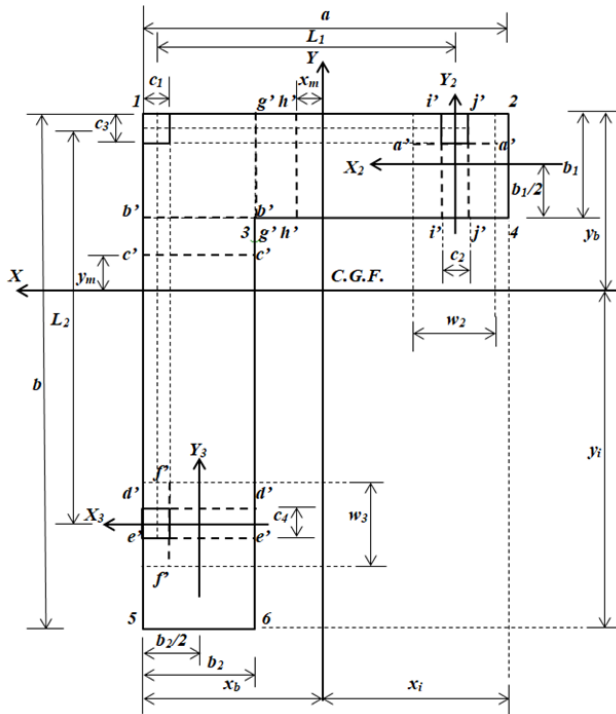
Figure 3. Critical sections for flexural moments
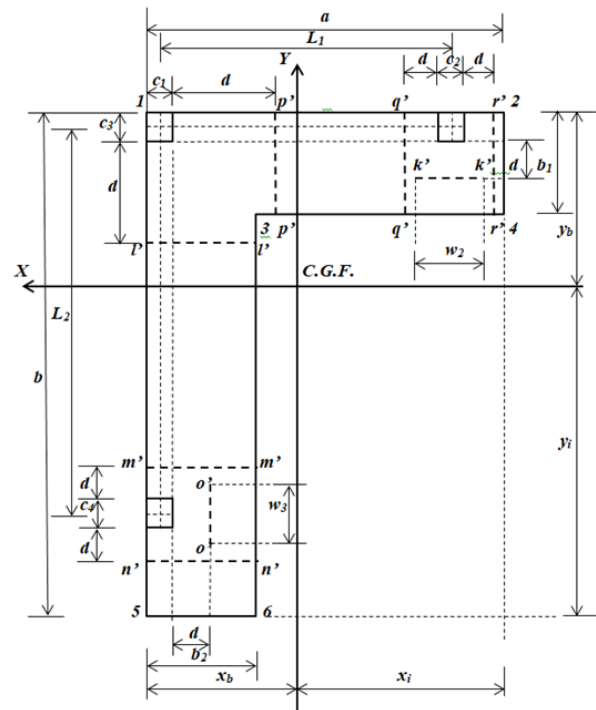
Figure 4. Critical sections for flexural shearing

Note: When the moments around the X axis are obtained, the moments around the Y axis are considered equal to zero. When the moments around the Y axis are obtained, the moments around the X axis do not influence. Because these are perpendicular axes between them.

2.1.1 Flexural shearing and moments on an axis parallel to the "X_2" axis of $-b_1/2 \leq y_2 \leq b_1/2 - c_3/2$

Shear force "V_{y2}" is found through the pressure volume of the area formed by the "X_2" axis with a width "$w_2 = c_2 + d$" and the free end (inner side) of the footing:

$$
V_{y_2} = -\int_{-b_1/2}^{y_2} \int_{-w_2/2}^{w_2/2} \sigma_{P_2}(x,y)dxdy
$$
$$
= -\frac{P_2\left[12(b_1 - c_3)y_2{}^2 + 4b_1{}^2 y_2 - b_1{}^2(b_1 - 3c_3)\right]}{4b_1{}^3} - \frac{3M_{x2}\left(4y_2{}^2 - b_1{}^2\right)}{2b_1{}^3} \quad (4)
$$

The moment by integration of equation (4) with respect to "y_2" is:

$$
M_{X_2} = -\frac{P_2 y_2\left[4(b_1 - c_3)y_2{}^2 + 2b_1{}^2 y_2 - b_1{}^2(b_1 - 3c_3)\right]}{4b_1{}^3} - \frac{M_{x2}y_2\left(4y_2{}^2 - 3b_1{}^2\right)}{2b_1{}^3} + C_1 \quad (5)
$$

where: M_{X2} is the moment around the "X_2" axis, and V_{y2} is the shear force at a distance "y_2". Now, substituting "$y_2 = -b_1/2$" and "$M_{X2} = 0$" into equation (5), we obtain the constant "C_1":

$$
C_1 = \frac{P_2(b_1 - 2c_3) + 4M_{x2}}{8} \quad (6)
$$

Substituting equation (6) into equation (5) and the generalized moment equation is presented as follows:

$$
\begin{aligned}
M_{X_2} = &-\frac{P_2 y_2\left[4(b_1 - c_3)y_2{}^2 + 2b_1{}^2 y_2 - b_1{}^2(b_1 - 3c_3)\right]}{4b_1{}^3} - \frac{M_{x2}y_2\left(4y_2{}^2 - 3b_1{}^2\right)}{2b_1{}^3} \\
&+ \frac{P_2(b_1 - 2c_3) + 4M_{x2}}{8}
\end{aligned} \quad (7)
$$

2.1.2 Flexural shearing and moments on an axis parallel to the "X" axis of $y_b - c_3/2 \leq y \leq y_b$

Shear force "V_y" is found through the pressure volume of the area formed by the "X" axis with a width "a" and the free end (top side) of the footing:

$$
V_y = -\int_y^{y_b} \int_{x_b-a}^{x_b} \sigma(x,y)dxdy
$$
$$
= -\frac{Ra(y_b - y)}{A} - \frac{M_{xT}a(y_b{}^2 - y^2)}{2I_x} - \frac{M_{yT}a(2x_b - a)(y_b - y)}{2I_y} \quad (8)
$$

The moment by integration of equation (8) with respect to "y" is:

$$
M_X = -\frac{Ray_1(2y_b - y)}{2A} - \frac{M_{xT}ay_1(3y_b{}^2 - y^2)}{6I_x} + C_2 \quad (9)
$$

where: M_X is the moment around the "X" axis, and V_y is the shear force at a distance "y".
Now, substituting "$y = y_b$" and "$M_X = 0$" into equation (9), we obtain the constant "C_2":

$$C_2 = \frac{Ray_b{}^2}{2A} + \frac{M_{xT}ay_b{}^3}{3I_x} \tag{10}$$

Substituting equation (10) into equation (9) and the generalized moment equation is presented as follows:

$$M_X = \frac{Ra(y_b - y)^2}{2A} + \frac{M_{xT}a(2y_b{}^3 - 3y_b{}^2y + y^3)}{6I_x} \tag{11}$$

Substituting "$y = y_b - c_3/2$" into equation (11), we obtain the moment around the axis located in the center of column 1 and 2 "$M_{c3/2}$":

$$M_{c_3/2} = \frac{Rac_3{}^2}{8A} + \frac{M_{xT}ac_3{}^2(6y_b - c_3)}{48I_x} \tag{12}$$

2.1.3 Flexural shearing and moments on an axis parallel to the "X" axis of $y_b - b_1 \leq y \leq y_b - c_3/2$

Shear force "V_y" is found through the pressure volume of the area formed by the "X" axis with a width "a" and the top side of the footing:

$$\begin{aligned} V_y &= P_1 + P_2 - \int_y^{y_b} \int_{x_b-a}^{x_b} \sigma(x,y)dxdy \\ &= P_1 + P_2 - \frac{Ra(y_b - y)}{A} - \frac{M_{xT}a(y_b{}^2 - y^2)}{2I_x} - \frac{M_{yT}a(2x_b - a)(y_b - y)}{2I_y} \end{aligned} \tag{13}$$

The moment by integration of equation (13) with respect to "y" is:

$$M_X = (P_1 + P_2)y - \frac{Ray_1(2y_b - y)}{2A} - \frac{M_{xT}ay_1(3y_b{}^2 - y^2)}{6I_x} + C_3 \tag{14}$$

Now, substituting "$y = y_b - c_3/2$" and "$M_X = M_{c3/2} - M_{x1} - M_{x2}$" into equation (14), we obtain the constant "C_3":

$$C_3 = \frac{Ray_b{}^2}{2A} + \frac{M_{xT}ay_b{}^3}{3I_x} - (P_1 + P_2)\left(y_b - \frac{c_3}{2}\right) - M_{x1} - M_{x2} \tag{15}$$

Substituting equation (15) into equation (14) and the generalized moment equation is presented as follows:

$$M_X = \frac{Ra(y_b - y)^2}{2A} + \frac{M_{xT}a(2y_b{}^3 - 3y_b{}^2y + y^3)}{6I_x} - (P_1 + P_2)\left(y_b - y - \frac{c_3}{2}\right) - M_{x1} - M_{x2} \tag{16}$$

An analytical model for the design of corner combined footings

Luévanos Rojas, A., López Chavarría, S., Medina Elizondo, M., Sandoval Rivas, R., Farías Montemayor, O. M.

323

Substituting "$y = y_b - b_1$" into equation (16), we obtain the moment around the b'-b' axis "M_{b1}":

$$M_{b_1} = \frac{Rab_1^2}{2A} + \frac{M_{xT}ab_1^2(3y_b - b_1)}{6I_x} - (P_1 + P_2)\left(b_1 - \frac{c_3}{2}\right) - M_{x1} - M_{x2} \tag{17}$$

2.1.4 Flexural shearing and moments on an axis parallel to the "X" axis of $y_b - L_2 - c_3/2 \leq y \leq y_b - b_1$

Shear force "V_y" is found through the pressure volume of the area formed by the "X" axis and the top side of the footing:

$$\begin{aligned}
V_y &= P_1 + P_2 - \int_{y_b-b_1}^{y_b}\int_{x_b-a}^{x_b} \sigma(x,y)dxdy - \int_{y}^{y_b-b_1}\int_{x_b-b_2}^{x_b} \sigma(x,y)dxdy \\
&= P_1 + P_2 - \frac{R[ab_1 + b_2(y_b - y - b_1)]}{A} \\
&\quad - \frac{M_{xT}\{ab_1(2y_b - b_1) + b_2[(y_b - b_1)^2 - y^2]\}}{2I_x} \\
&\quad - \frac{M_{yT}[ab_1(2x_b - a) + b_2(2x_b - b_2)(y_b - y - b_1)]}{2I_y}
\end{aligned} \tag{18}$$

The moment by integration of equation (18) with respect to "y" is:

$$\begin{aligned}
M_X &= (P_1 + P_2)y - \frac{Ry[2ab_1 + b_2(2y_b - y - 2b_1)]}{2A} \\
&\quad - \frac{M_{xT}y\{3ab_1(2y_b - b_1) + b_2[3(y_b - b_1)^2 - y^2]\}}{6I_x} + C_4
\end{aligned} \tag{19}$$

Now, substituting "$y = y_b - b_1$" and "$M_X = M_{b1}$" into equation (19), we obtain the constant "C_4":

$$\begin{aligned}
C_4 &= \frac{R[ab_1(2y_b - b_1) + b_2(y_b - b_1)^2]}{2A} + \frac{M_{xT}[ab_1(3y_b^2 - 3y_bb_1 + b_1^2) + b_2(y_b - b_1)^3]}{3I_x} \\
&\quad - (P_1 + P_2)\left(y_b - \frac{c_3}{2}\right) - M_{x1} - M_{x2}
\end{aligned} \tag{20}$$

Substituting equation (20) into equation (19) and the generalized moment equation is presented as follows:

$$\begin{aligned}
M_X &= \frac{R[ab_1(2y_b - 2y - b_1) + b_2(y_b - y - b_1)^2]}{2A} - \frac{(P_1 + P_2)(2y_b - 2y - c_3)}{2} \\
&\quad + \frac{M_{xT}ab_1[2(3y_b^2 - 3y_bb_1 + b_1^2) - 3y(2y_b - b_1)]}{6I_x} \\
&\quad + \frac{M_{xT}b_2[y^3 + (y_b - b_1)^2(2y_b - 3y - 2b_1)]}{6I_x} - M_{x1} - M_{x2}
\end{aligned} \tag{21}$$

Substituting "$y = y_b - L_2 - c_3/2$" into equation (21), we obtain the moment around the axis located in the center of column 3 "M_{L2}":

$$M_{L_2} = \frac{R[ab_1(2L_2 + c_3 - b_1) + b_2(L_2 + c_3/2 - b_1)^2]}{2A} - (P_1 + P_2)L_2$$
$$+ \frac{M_{xT}ab_1{}^2(3y_b - b_1)}{6I_x} + \frac{M_{xT}b_2[(y_b - L_2 - c_3/2)^3 - (y_b - b_1)^3]}{6I_x} \quad (22)$$
$$+ \frac{M_{xT}\{3[ay_b{}^2 - (a - b_2)(y_b - b_1)^2](L_2 + c_3/2 - b_1)\}}{6I_x} - M_{x1} - M_{x2}$$

2.1.5 Flexural shearing and moments on an axis parallel to the "X" axis of $y_b - b \le y \le y_b - L_2 - c_3/2$

Shear force "V_y" is found through the pressure volume of the area formed by the "X" axis and the top side of the footing:

$$V_y = P_1 + P_2 + P_3 - \int_{y_b-b_1}^{y_b} \int_{x_b-a}^{x_b} \sigma(x,y)dxdy - \int_{y}^{y_b-b_1} \int_{x_b-b_2}^{x_b} \sigma(x,y)dxdy$$
$$= R - \frac{M_{yT}[ab_1(2x_b - a) + b_2(2x_b - b_2)(y_b - y - b_1)]}{2I_y} \quad (23)$$
$$- \frac{R[ab_1 + b_2(y_b - y - b_1)]}{A} - \frac{M_{xT}\{ab_1(2y_b - b_1) + b_2[(y_b - b_1)^2 - y^2]\}}{2I_x}$$

The moment by integration of equation (23) with respect to "y" is:

$$M_X = Ry - \frac{R[2ab_1 + b_2(2y_b - y - 2b_1)]y}{2A}$$
$$- \frac{M_{xT}[3ab_1(2y_b - b_1) + b_2[3(y_b - b_1)^2 - y^2]]y}{6I_x} + C_5 \quad (24)$$

Now, substituting "$y = y_b - L_2 - c_3/2$" and "$M_X = M_{L2} - M_{x3}$" into equation (24), we obtain the constant "C_5":

$$C_5 = \frac{R[ab_1(2y_b - b_1) + b_2(y_b - b_1)^2]}{2A} + \frac{M_{xT}[ay_b{}^3 - (a - b_2)(y_b - b_1)^3]}{3I_x} + P_3L_2$$
$$- \frac{R(2y_b - c_3)}{2} - M_{x1} - M_{x2} - M_{x3} \quad (25)$$

Substituting equation (25) into equation (24) and the generalized moment equation is presented as follows:

$$M_X = P_3L_2 - \frac{R[b_2y(2y_b - y - 2b_1) - ab_1(2y_b - 2y - b_1) - b_2(y_b - b_1)^2]}{2A}$$
$$- R\left(y_b - y - \frac{c_3}{2}\right) + \frac{M_{xT}[ay_b{}^3 - (a - b_2)(y_b - b_1)^3]}{3I_x} \quad (26)$$
$$- \frac{M_{xT}\{3ab_1(2y_b - b_1) + b_2[3(y_b - b_1)^2 - y^2]\}y}{6I_x} - M_{x1} - M_{x2} - M_{x3}$$

In the next paragraphs we get the equations of the shear forces and generalized moments by the procedure used above. Therefore, the equations for shear forces and generalized moments are shown below.

2.1.6 Flexural shearing and moments on an axis parallel to the "Y_3" axis of $-b_2/2 \leq x_3 \leq b_2/2 - c_1/2$

$$
\begin{aligned}
V_{x_3} &= -\int_{-w_3/2}^{w_3/2}\int_{-b_2/2}^{x_3} \sigma_{P_3}(x,y)dxdy \\
&= -\frac{P_3\left[12(b_2 - c_1)x_3{}^2 + 4b_2{}^2 x_3 - b_2{}^2(b_2 - 3c_1)\right]}{4b_2{}^3} - \frac{3M_{y3}\left(4x_3{}^2 - b_2{}^2\right)}{2b_2{}^3}
\end{aligned}
\tag{27}
$$

$$
\begin{aligned}
M_{Y_3} &= -\frac{P_3 x_3\left[4(b_2 - c_1)x_3{}^2 + 2b_2{}^2 x_3 - b_2{}^2(b_2 - 3c_1)\right]}{4b_2{}^3} - \frac{M_{y3}x_3\left(4x_3{}^2 - 3b_2{}^2\right)}{2b_2{}^3} \\
&\quad + \frac{P_3(b_2 - 2c_1) + 4M_{y3}}{8}
\end{aligned}
\tag{28}
$$

2.1.7 Flexural shearing and moments on an axis parallel to the "Y" axis of $x_b - c_1/2 \leq x \leq x_b$

$$
\begin{aligned}
V_x &= -\int_{y_b-b}^{y_b}\int_{x}^{x_b} \sigma(x,y)dxdy \\
&= -\frac{Rb(x_b - x)}{A} - \frac{M_{xT}b(2y_b - b)(x_b - x)}{2I_x} - \frac{M_{yT}b(x_b{}^2 - x^2)}{2I_y}
\end{aligned}
\tag{29}
$$

$$
M_Y = \frac{Rb(x_b - x)^2}{2A} + \frac{M_{yT}b\left(2x_b{}^3 - 3x_b{}^3 x + x^3\right)}{6I_y}
\tag{30}
$$

2.1.8 Flexural shearing and moments on an axis parallel to the "Y" axis of $x_b - b_2 \leq x \leq x_b - c_1/2$

$$
\begin{aligned}
V_x &= P_1 + P_3 - \int_{y_b-b}^{y_b}\int_{x}^{x_b} \sigma(x,y)dxdy \\
&= P_1 + P_3 - \frac{Rb(x_b - x)}{A} - \frac{M_{xT}b(2y_b - b)(x_b - x)}{2I_x} - \frac{M_{yT}b(x_b{}^2 - x^2)}{2I_y}
\end{aligned}
\tag{31}
$$

$$
M_Y = \frac{Rb(x_b - x)^2}{2A} + \frac{M_{yT}b(2x_b{}^3 - 3x_b{}^2 x + x^3)}{6I_y} - (P_1 + P_3)\left(x_b - x - \frac{c_1}{2}\right) - M_{y1} - M_{y3}
\tag{32}
$$

2.1.9 Flexural shearing and moments on an axis parallel to the "Y" axis of $x_b - L_1 - c_1/2 \leq x \leq x_b - b_2$

$$
\begin{aligned}
V_x &= P_1 + P_3 - \int_{y_b-b}^{y_b} \int_{x_b-b_2}^{x_b} \sigma(x,y)dxdy - \int_{y_b-b_1}^{y_b} \int_{x}^{x_b-b_2} \sigma(x,y)dxdy \\
&= P_1 + P_3 - \frac{R[bb_2 + b_1(x_b - x - b_2)]}{A} \\
&\quad - \frac{M_{xT}[bb_2(2y_b - b) + b_1(2y_b - b_1)(x_b - x - b_2)]}{2I_x} \\
&\quad - \frac{M_{yT}\{bb_2(2x_b - b_2) + b_1[(x_b - b_2)^2 - x^2]\}}{2I_y}
\end{aligned}
\tag{33}
$$

$$
\begin{aligned}
M_Y &= \frac{R[bb_2(2x_b - 2x - b_2) + b_1(x_b - x - b_2)^2]}{2A} - \frac{(P_1 + P_3)(2x_b - 2x - c_1)}{2} \\
&\quad + \frac{M_{yT}bb_2[2(3x_b{}^2 - 3x_bb_2 + b_2{}^2) - 3x(2x_b - b_2)]}{6I_y} \\
&\quad + \frac{M_{yT}b_1[x^3 + (x_b - b_2)^2(2x_b - 3x - 2b_2)]}{6I_y} - M_{y1} - M_{y3}
\end{aligned}
\tag{34}
$$

2.1.10 Flexural shearing and moments on an axis parallel to the "Y" axis of $x_b - a \leq x \leq x_b - L_1 - c_1/2$

$$
\begin{aligned}
V_x &= P_1 + P_2 + P_3 - \int_{y_b-b}^{y_b} \int_{x_b-b_2}^{x_b} \sigma(x,y)dxdy - \int_{y_b-b_1}^{y_b} \int_{x}^{x_b-b_2} \sigma(x,y)dxdy \\
&= R - \frac{M_{xT}[bb_2(2y_b - b) + b_1(2y_b - b_1)(x_b - x - b_2)]}{2I_x} \\
&\quad - \frac{M_{yT}\{bb_2(2x_b - b_2) + b_1[(x_b - b_2)^2 - x^2]\}}{2I_y} - \frac{R[bb_2 + b_1(x_b - x - b_2)]}{A}
\end{aligned}
\tag{35}
$$

$$
\begin{aligned}
M_Y &= P_2 L_1 - \frac{R[b_1 x(2x_b - x - 2b_2) - bb_2(2x_b - 2x - b_2) - b_1(x_b - b_2)^2]}{A} \\
&\quad - R\left(x_b - x - \frac{c_1}{2}\right) + \frac{M_{yT}[bx_b{}^3 - (b - b_1)(x_b - b_2)^3]}{3I_y} \\
&\quad - \frac{M_{yT}\{3bb_2(2x_b - b_2) + b_1[3(x_b - b_2)^2 - x^2]\}x}{6I_y} - M_{y1} - M_{y2} - M_{y3}
\end{aligned}
\tag{36}
$$

2.2 Punching shearing
The critical sections for punching shearing are shown in Figure 5.

2.2.1 Punching shearing for the corner column (column 1)
The critical section for column 1 is presented at the perimeter formed by points 1, 7, 8 and 9 of the footing (see Figure 5). The punching shearing is obtained by the axial load of column 1 minus the pressure volume of the area delimited by points 1, 7, 8 and 9:

An analytical model for the design of corner combined footings

Luévanos Rojas, A., López Chavarría, S., Medina Elizondo, M., Sandoval Rivas, R., Farías Montemayor, O. M.

327

$$V_{p1} = P_1 - \int_{y_b-c_3-d/2}^{y_b} \int_{x_b-c_1-d/2}^{x_b} \sigma(x,y)dxdy$$

$$= P_1 - \frac{M_{xT}(2y_b - c_3 - d/2)(c_1 + d/2)(c_3 + d/2)}{2I_x}$$

$$- \frac{M_{yT}(2x_b - c_1 - d/2)(c_1 + d/2)(c_3 + d/2)}{2I_y} - \frac{R(c_1 + d/2)(c_3 + d/2)}{A} \qquad (37)$$
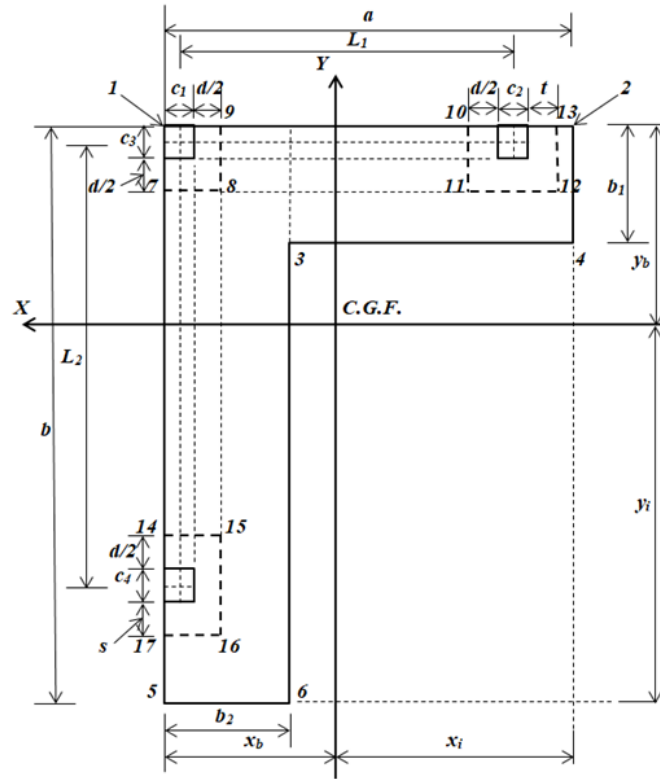
Figure 5. Critical sections for punching shearing

2.2.2 Punching shearing for the column of a limit (column 2)
The critical section for column 2 is presented at the perimeter formed by points 10, 11, 12 and 13 of the footing (see Figure 5). The punching shearing is obtained by the axial load of column 2 minus the pressure volume of the area delimited by points 10, 11, 12 and 13:

$$V_{p2} = P_2 - \int_{y_b-c_3-d/2}^{y_b} \int_{x_b-L_1-(c_1+c_2)/2-t}^{x_b-L_1-(c_1-c_2)/2+d/2} \sigma(x,y)dxdy$$

$$= P_2 - \frac{M_{yT}(c_2 + d/2 + t)(c_3 + d/2)(2x_b - 2L_1 - c_1 + d/2 - t)}{2I_y}$$

$$- \frac{M_{xT}(c_2 + d/2 + t)(c_3 + d/2)(2y_b - c_3 - d/2)}{2I_x}$$

$$- \frac{R(c_2 + d/2 + t)(c_3 + d/2)}{A} \qquad (38)$$

Note: when $d/2 \leq a - L_1 - (c_1 + c_2)/2 \rightarrow t = d/2$, and when $d/2 > a - L_1 - (c_1 + c_2)/2 \rightarrow t = a - L_1 - (c_1 + c_2)/2$.

2.2.3 Punching shearing for the column of a limit (column 3)

The critical section for column 3 is presented at the perimeter formed by points 14, 15, 16 and 17 of the footing (see Figure 5). The punching shearing is obtained by the axial load of column 3 minus the pressure volume of the area delimited by points 14, 15, 16 and 17:

$$
\begin{aligned}
V_{p3} = P_3 &- \int_{y_b-L_2-(c_3+c_4)/2-s}^{y_b-L_2-(c_3-c_4)/2+d/2} \int_{x_b-c_1-d/2}^{x_b} \sigma(x,y)dxdy \\
&= P_3 - \frac{M_{xT}(c_4 + d/2 + s)(c_1 + d/2)(2y_b - 2L_2 - c_3 + d/2 - s)}{2I_x} \\
&- \frac{M_{yT}(c_4 + d/2 + s)(c_1 + d/2)(2x_b - c_1 - d/2)}{2I_y} \\
&- \frac{R(c_4 + d/2 + s)(c_1 + d/2)}{A}
\end{aligned}
\tag{39}
$$

Note: when $d/2 \le b - L_2 - (c_3 + c_4)/2 \to s = d/2$, and when $d/2 > b - L_2 - (c_3 + c_4)/2 \to t = b - L_2 - (c_3 + c_4)/2$.

3. VERIFICATION OF THE PROPOSED MODEL

The model proposed in this document is verified as follows:

1.- For flexural moments on the X_2 and X axes: When "$y_2 = - b_1/2$" is substituted into equation (7) we obtain $M_{X2} = 0$, if "$y = y_b$" is substituted into equation (11) we obtain $M_X = 0$, and substituting "$y = y_b - b$" into equation (26) we obtain $M_X = 0$. Therefore, the equations for the moments on the X_2 and X axes satisfy the equilibrium.

2.- For flexural moments on the Y_3 and Y axes: When "$x_3 = - b_2/2$" is substituted into equation (28) we obtain $M_{Y3} = 0$, if "$x = x_b$" is substituted into equation (30) we obtain $M_Y = 0$, and substituting "$x = x_b - a$" into equation (36) we obtain $M_Y = 0$. Therefore, the equations for the moments on the Y_3 and Y axes satisfy the equilibrium.

3.- For flexural shearing on the X_2 and X axes: When "$y_2 = - b_1/2$" is substituted into equation (4) we obtain $V_{y2} = 0$, if "$y = y_b$" is substituted into equation (8) we obtain $V_y = 0$, and substituting "$y = y_b - b$" into equation (23) we obtain $V_y = 0$. Therefore, the equations for the flexural shearing on the X_2 and X axes satisfy the equilibrium.

4.- For flexural shearing on the Y_3 and Y axes: When "$x_3 = - b_2/2$" is substituted into equation (27) we obtain $V_{x3} = 0$, if "$x = x_b$" is substituted into equation (29) we obtain $V_x = 0$, and substituting "$x = x_b - a$" into equation (35) we obtain $V_x = 0$. Therefore, the equations for the flexural shearing on the Y_3 and Y axes satisfy the equilibrium.

4. APPLICATION OF THE PROPOSED MODEL

The design of a corner combined footing that supports three square columns is shown below with the following information: the three columns are of 40x40 *cm*, $L_1 = 5.00$ *m*, $L_2 = 5.00$ *m*, H (depth of the footing) = 2.0 *m*, $P_{D1} = 300$ *kN*, $P_{L1} = 200$ *kN*, $M_{Dx1} = 80$ *kN-m*, $M_{Lx1} = 70$ *kN-m*, $M_{Dy1} = 120$ *kN-m*, $M_{Ly1} = 80$ *kN-m*, $P_{D2} = 600$ *kN*, $P_{L2} = 400$ *kN*, $M_{Dx2} = 160$ *kN-m*, $M_{Lx2} = 140$ *kN-m*, $M_{Dy2} = 120$ *kN-m*, $M_{Ly2} = 80$ *kN-m*, $P_{D3} = 500$ *kN*, $P_{L3} = 400$ *kN*, $M_{Dx3} = 120$ *kN-m*, $M_{Lx3} = 80$ *kN-m*, $M_{Dy3} = 150$ *kN-m*, $M_{Ly3} = 100$ *kN-m*, $f'_c = 28$ *MPa*, $f_y = 420$ *MPa*, $q_a = 252$ *kN/m²*, γ_c (concrete density) = 24 *kN/m³*, γ_s (ground fill density) = 15 *kN/m³*.

The loads and moments acting on the corner combined footing are: $P_1 = 500$ kN-m, $M_{x1} = 150$ kN-m, $M_{y1} = 200$ kN-m, $P_2 = 1000$ kN, $M_{x2} = 300$ kN-m, $M_{y2} = 200$ kN-m, $P_3 = 900$ kN, $M_{x3} = 200$ kN-m, $M_{y3} = 250$ kN-m.

The available load capacity of the ground is assumed of $\sigma_{máx} = 213.00$ kN/m², because at the load capacity of the ground "q_a" is subtracted from the weight of the footing (γ_c by the thickness of the footing), and the weight of the filling of the ground (γ_s by the thickness of the filling).

Substituting $\sigma_{máx}$, L_1, L_2, P_1, M_{x1}, M_{y1}, P_2, M_{x2}, M_{y2}, P_3, M_{x3}, M_{y3} into equations (30) to (42) from work (López-Chavarría et al. 2017), and the solution by MAPLE-15 software is: $A_{min} = 11.31$ m², $M_{xT} = -8.65$ kN-m, $M_{yT} = 9.49$ kN-m, $R = 2400$ kN, $a = 6.36$ m, $b = 5.95$ m, $b_1 = 1.00$ m, $b_2 = 1.00$ m, $\sigma_1 = 211.31$ kN/m², $\sigma_2 = 212.75$ kN/m², $\sigma_3 = 211.78$ kN/m², $\sigma_4 = 213.00$ kN/m², $\sigma_5 = 212.77$ kN/m², $\sigma_6 = 213.00$ kN/m².

The practical dimensions of the corner combined footing that supports three square columns are: $a = 6.40$ m, $b = 6.00$ m, $b_1 = 1.00$ m, $b_2 = 1.00$ m. Now, the practical dimensions to verify the stresses are substituted in the same software MAPLE-15, and the solution is: $A_{min} = 11.40$ m², $M_{xT} = 27.89$ kN-m, $M_{yT} = 7.89$ kN-m, $R = 2400$ kN, $a = 6.40$ m, $b = 6.00$ m, $b_1 = 1.00$ m, $b_2 = 1.00$ m, $\sigma_1 = 212.30$ kN/m², $\sigma_2 = 211.11$ kN/m², $\sigma_3 = 211.34$ kN/m², $\sigma_4 = 210.34$ kN/m², $\sigma_5 = 207.68$ kN/m², $\sigma_6 = 207.49$ kN/m².

The geometric properties of the footing are: $x_b = 2.02$ m, $y_b = 1.82$ m, $I_x = 36.21$ m⁴, $I_y = 42.73$ m⁴. The factorized loads and moments acting on the footing are: $P_{u1} = 680$ kN, $M_{ux1} = 208$ kN-m, $M_{uy1} = 272$ kN-m, $P_{u2} = 1360$ kN, $M_{ux2} = 416$ kN-m, $M_{uy2} = 272$ kN-m, $P_{u3} = 1240$ kN, $M_{ux3} = 272$ kN-m, $M_{uy3} = 340$ kN-m. The resulting loads and moments factorized by equations (31) to (33) (López-Chavarría et al., 2017) are obtained: $R_u = 3280$ kN, $M_{uxT} = -4.21$ kN-m, $M_{uyT} = 39.79$ kN-m.

The moment on the a'-a' axis by equation (7) is obtained "$M_{a'} = 289.15$ kN-m" in $y_2 = b_1/2 - c_3$. The moment on the b'-b' axis by equation (16) is obtained "$M_{b'} = -1335.85$ kN-m" in $y = y_b - b_1$. Now, substituting the corresponding values into equation (21) and deriving with respect to "y", this is equal to zero to obtain the position the maximum moment "$y_m = 0.12$ m", subsequently, it is substituted in equation (21), and the moment is obtained "$M_{c'} = -1405.08$ kN-m". The moment on the d'-d' axis by equation (21) is obtained "$M_{d'} = 168.08$ kN-m" in $y = y_b - L_2 - c_3/2 + c_4/2$. The moment on the e'-e' axis by equation (26) is obtained "$M_{e'} = 51.87$ kN-m" in $y = y_b - L_2 - c_3/2 - c_4/2$.

The moment on the f'-f' axis by equation (28) is obtained "$M_{f'} = 238.18$ kN-m" in $x_3 = b_2/2 - c_1$. The moment on the g'-g' axis by equation (32) is obtained "$M_{g'} = -1280.14$ kN-m" in $x = x_b - b_2$. Now, substituting the corresponding values into equation (34) and deriving with respect to "x", this is equal to zero to obtain the position the maximum moment "$x_m = 0.37$ m", subsequently, it is substituted in equation (34), and the moment is obtained "$M_{h'} = -1339.60$ kN-m". The moment on the i'-i' axis by equation (34) is obtained "$M_{i'} = 278.39$ kN-m" in $x = x_b - L_1 - c_1/2 + c_2/2$. The moment on the j'-j' axis by equation (36) is obtained "$M_{j'} = 141.97$ kN-m" in $x = x_b - L_1 - c_1/2 - c_2/2$.

The effective cant below column 2 is: 18.33 cm. The effective cant for the maximum moment "$M_{c'}$" is: 46.42 cm. The effective cant below column 3 is: 16.63 cm. The effective cant for the maximum moment "$M_{h'}$" is: 45.32 cm. The effective cant after several proposals is: $d = 92.00$ cm, $r = 8.00$ cm and $t = 100$ cm.

Table 1 shows the flexural shearing acting on the footing and those resisted by the concrete according to the code (ACI 318S-14).

Table 1. Flexural shearing.

Axes	Coordinates	Analysis width cm	Flexural shearing	
			Acting kN	Resisted kN
k'	$y_2 = b_1/2 - c_3 - d$	132	0*	928.56
l'	$y = y_b - c_3 - d$	100	114.14	703.45
m'	$y = y_b - c_3/2 - L_2 + c_4/2 + d$	100	– 684.15	703.45
n'	$y = y_b - c_3/2 - L_2 - c_4/2 - d$	100	0*	703.45
o'	$x_3 = b_2/2 - c_1 - d$	132	0*	928.56
p'	$x = x_b - c_1 - d$	100	92.11	703.45
q'	$x = x_b - c_1/2 - L_1 + c_2/2 + d$	100	– 699.81	703.45
r'	$y = y_b - c_3/2 - L_2 - c_4/2 - d$	100	22.68	703.45

* The axis is located outside the footing area.

Table 2 shows the punching shearing acting on the footing and those resisted by the concrete according to the code (ACI 318S-14).

Table 2. Punching shearing.

Column	Critical perimeter	Punching shearing			
		Acting kN	Resisted kN		
1	$b_0 = c_1 + c_3 + d$	466.23	3629.81	7500.95	2348.70
2	$b_0 = c_2 + 2c_3 + 2d$	1036.93	6415.49	13112.93	4151.20
3	$b_0 = 2c_1 + c_4 + 2d$	911.26	6415.49	13112.93	4151.20

Table 3 shows the reinforcing steel of the corner combined footing (ACI 318S-14).

Table 3. Reinforcing steel of the footing.

Reinforcing steel			Area cm²
Direction of the "Y" axis	Steel on the top with a width b_2	Main steel	42.10
		Minimum steel	30.67
		Steel proposed	45.63 (9Ø1")
	Steel on the top with a width $a - b_2$	Steel by temperature	97.20
		Steel proposed	99.75 (35Ø3/4")
	Steel at the bottom with a width b_2	Main steel	4.86
		Minimum steel	30.67
		Steel proposed	35.49 (7Ø1")
	Steel below of the column 2 with a width w_2	Main steel	8.37
		Minimum steel	40.48
		Steel proposed	42.75 (15Ø3/4")
	Steel at the bottom with a width $a - b_2 - w_2$	Steel by temperature	73.44
		Steel proposed	74.10 (26Ø3/4")
Direction of the "X" axis	Steel on the top with a width b_1	Main steel	40.06
		Minimum steel	30.67
		Steel proposed	40.56 (8Ø1")
	Steel on the top with a width	Steel by temperature	90.00

	$b - b_1$	Steel proposed	91.20 (32Ø3/4")
	Steel at the bottom with a width b_1	Main steel	8.07
		Minimum steel	30.67
		Steel proposed	35.49 (7Ø1")
	Steel below of the column 3 with a width w_3	Main steel	6.88
		Minimum steel	40.48
		Steel proposed	42.75 (15Ø3/4")
	Steel at the bottom with a width $b - b_1 - w_3$	Steel by temperature	66.24
		Steel proposed	68.40 (24Ø3/4")

The effects that govern the thickness of the footings are the moments, the flexural shearing and the punching shearing, and the reinforcing steel is designed by the moments. For the thickness of the numerical example, it governs by the flexural shearing on the q'-q' axis (see Table 1).
Table 4 shows the minimum development length for deformed bars "l_d" and the available length "l_a".
Thus, the available length is greater than the minimum development length in both directions (top and bottom) (see Table 4). Therefore, the hooks are not necessary for the corner combined footing.

Table 4. Minimum development length and available length.

Location of steel	ψ_t	$\psi_e = \lambda$	Development length cm	Available length	
				Direction of the "X" axis cm	Direction of the "Y" axis cm
Top	1.3	1.0	154.17	165	170
Bottom	1.0	1.0	96.00	140	100

Figure 6 shows in detail the reinforcing steel and the dimensions of the corner combined footing.
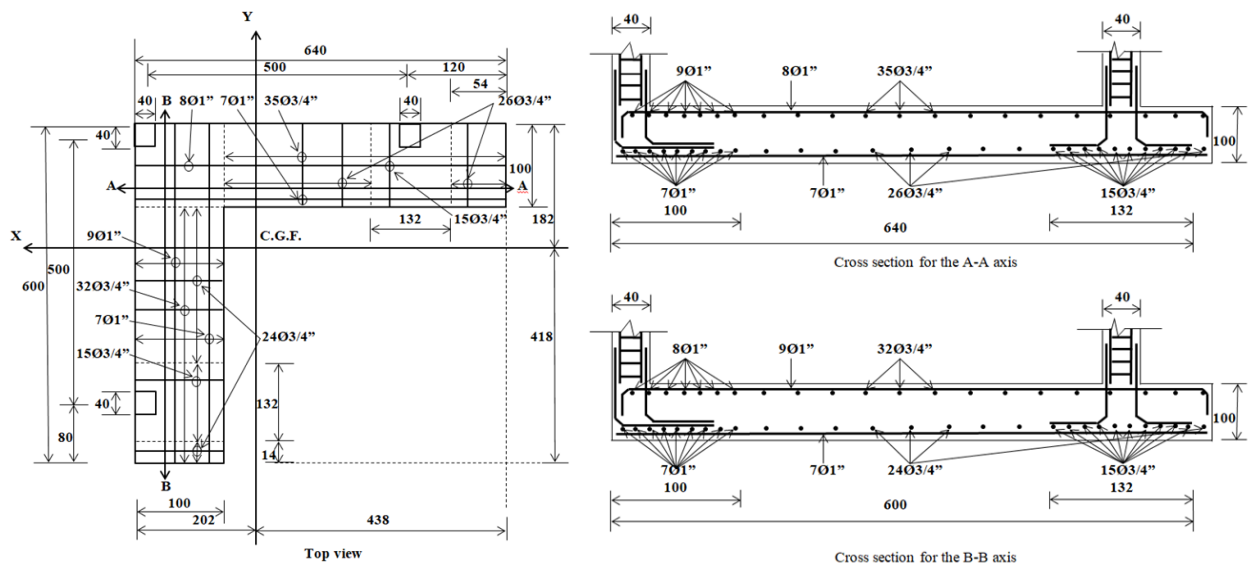

Figure 6. Final design of the corner combined footing

5. CONCLUSIONS

The new model presented in this work is applied only for the design of corner combined footings. The assumptions are: the structural member is rigid and the ground that supports the footing is elastic and homogeneous, which complies with the expression of the biaxial flexure, i.e., the pressure varies linearly.

The new model presented in this document concludes the following:

1.- The thickness for the corner combined footings is governed by the flexural shearing, and the isolated footings are governed by the punching shearing.

2.- The new model is not limited, whereas the current design assumes that the maximum pressure at all contact points, i.e., the force resulting from the applied loads coincides with the position of the geometric center of the footing.

3.- The new model is more suited to real conditions with respect to the current design, because the new model takes into account the linear pressure of the ground and the current design considers the uniform pressure in all the contact surface and this is the maximum pressure.

4.- The new model for the design of corner combined footings subject to axial load and two moments in orthogonal directions due to each column considers two restricted property lines, but it can be applied to three property lines.

The new model shown in this work in terms of the applied loads due to each column can be applied to: 1) Load without moments, 2) Load and a moment (uniaxial flexure), 3) Load and two orthogonal moments (biaxial flexure).

Therefore, the proposed model is the most appropriate, since it generates better quality control in the resources used.

Important issues for future research may be: 1) A continuation of this work will be to formulate the minimum cost for the corner combined footings; 2) When the corner combined footings support more than two columns in each direction; 3) The proposed model can be expanded to design foundation slabs; 4) When the footing rests on another type of ground, by example on totally clayey grounds (cohesive grounds) or on totally sandy grounds (granular grounds), the pressure diagram is different from the linear and the diagram could be parabolic (see Figure 1).

6. REFERENCES

Abdrabbo, F., Mahmoud, Z. I. and Ebrahim, M. (2016), *Structural design of isolated column footings*. Alexandria Engineering Journal. 55(3):2665-2678. https://doi.org/10.1016/j.aej.2016.06.016

ACI 318S-14 (2014), "*Building Code Requirements for Structural Concrete and Commentary*, Committee 318", New York, USA.

Anil, Ö, Akbaş, S.O., BabagĪray, S., Gel, A.C. and Durucan, C. (2017), *Experimental and finite element analyses of footings of varying shapes on sand*. Geomechanics and Engineering. 12(2):223-238. https://doi.org/10.12989/gae.2017.12.2.223

Aydogdu, I. (2016), *New Iterative method to Calculate Base Stress of Footings under Biaxial Bending*. International Journal of Engineering & Applied Sciences (IJEAS). 8(4):40-48. https://doi.org/10.24107/ijeas.281460

Balachandar, S. and Narendra Prasad, D. (2017), *Analysis and Design of Various Types of Isolated Footings*. International Journal of Innovative Research in Science, Engineering and Technology. 6(3):3980-3986. http://www.ijirset.com/upload/2017/march/173_balachandar%20pmu.pdf

Bowles, J. E. (2001), "*Foundation analysis and design*". McGraw-Hill, New York, USA.

Chen, W-R., Chen, C-S and Yu, S-Y. (2011), *Nonlinear vibration of hybrid composite plates on elastic foundations*. Structural Engineering & Mechanics. 37(4):367-383. https://doi.org/10.12989/sem.2011.37.4.367

Das, B.M., Sordo-Zabay, E., Arrioja-Juarez, R. (2006), "*Principios de ingeniería de cimentaciones*", Cengage Learning Latín América, Distrito Federal, México.

Dezhkam, B. and Yaghfoori, A. (2018), *Soil foundation effect on the vibration response of concrete foundations using mathematical model*. Computers and Concrete. 22(2):221-225. https://doi.org/10.12989/cac.2018.22.2.221

El-kady, M. S. and Badrawi, E. F. (2017), *Performance of isolated and folded footings*. Journal of Computational Design and Engineering. 4:150-157. https://doi.org/10.1016/j.jcde.2016.09.001

Sawwaf, M. and Nazir, A. K. (2010), *Behavior of repeatedly loaded rectangular footings resting on reinforced sand*. Alexandria Engineering Journal. 49:349-356. https://doi.org/10.1016/j.aej.2010.07.002

Fillo, L., Augustin, T. and Knapcová, V. (2016), *Influence of footings stiffness on punching resistance*. Perspectives in Science. 7:204-207. https://doi.org/10.1016/j.pisc.2015.11.034

Ibrahim, A., Dif, A. and Othman, W. (2018), *Nonlinearity analysis in studying shallow grid foundation*. Alexandria Engineering Journal. 57:859-866. https://doi.org/10.1016/j.aej.2016.11.021

Khajehzadeh, M., Taha, M. R., El-Shafie, A. and Eslami, M. (2011), *Modified particle swarm optimization for optimum design of spread footing and retaining wall*. Journal of Zhejiang University-SCIENCE A. 12(6):415-427. https://link.springer.com/article/10.1631/jzus.A1000252

Kurian, N. P. (2005), "*Design of foundation systems*", Alpha Science Int'l Ltd., New Delhi, India.

López-Chavarría, S., Luévanos Rojas, A. and Medina Elizondo, M. (2017), *Optimal dimensioning for the corner combined footings*. Advances in Computational Design. **2**(2):169-183. https://doi.org/10.12989/acd.2017.2.2.169

Luévanos-Rojas, A., Faudoa-Herrera, J. G., Andrade-Vallejo, R. A. and Cano-Alvarez M. A. (2013), *Design of Isolated Footings of Rectangular Form Using a New Model*. International Journal of Innovative Computing, Information and Control. 9(10):4001-4022. http://www.ijicic.org/ijicic-12-10031.pdf

Luévanos-Rojas, A. (2014a), *Design of isolated footings of circular form using a new model*. Structural Engineering and Mechanics. 52(4):767-786. https://doi.org/10.12989/sem.2014.52.4.767

Luévanos-Rojas, A. (2014b), *Design of boundary combined footings of rectangular shape using a new model*. Dyna-Colombia. 81(188):199-208. http://dx.doi.org/10.15446/dyna.v81n188.41800

Luévanos-Rojas, A. (2015), *Design of boundary combined footings of trapezoidal form using a new model*. Structural Engineering and Mechanics. 56(5):745-765. https://doi.org/10.12989/sem.2015.56.5.745

Luévanos-Rojas, A. (2016a), *A comparative study for the design of rectangular and circular isolated footings using new models*. Dyna-Colombia. 83(196):149-158. http://dx.doi.org/10.15446/dyna.v83n196.51056

Luévanos-Rojas, A. (2016b), *A new model for the design of rectangular combined boundary footings with two restricted opposite sides*. Revista ALCONPAT. 6(2):172-187. https://doi.org/10.21041/ra.v6i2.137

Luévanos-Rojas, A., López-Chavarría, S. and Medina-Elizondo, M. (2017a), *Optimal design for rectangular isolated footings using the real soil pressure*. Ingeniería e Investigación. 37(2):25-33. http://dx.doi.org/10.15446/ing.investig.v37n2.61447

Luévanos-Rojas, A., Barquero-Cabrero, J. D., López-Chavarría, S. and Medina-Elizondo, M. (2017b), *A comparative study for design of boundary combined footings of trapezoidal and*

rectangular forms using new models. Coupled Systems Mechanics. 6(4):417-437. https://doi.org/10.12989/csm.2017.6.4.417

Luévanos-Rojas, A., López-Chavarría, S. & Medina-Elizondo, M. (2018), *A new model for T-shaped combined footings Part II: Mathematical model for design*. Geomechanics and Engineering. 14(1):61-69. https://doi.org/10.12989/gae.2018.14.1.061

Magade, S. B. and Ingle, R. K. (2019), *Numerical method for analysis and design of isolated square footing under concentric loading*. International Journal of Advanced Structural Engineering. 11:9-20. https://doi.org/10.1007/s40091-018-0211-3

Punmia, B. C., Kumar-Jain, A., Kumar-Jain, A. (2007), "*Limit state design of reinforced concrete*", Laxmi Publications (P) Limited, New Delhi, India.

Santos, D. F. A., Lima Neto, A. F. and Ferreira, M. P. (2018), *Punching shear resistance of reinforced concrete footings: evaluation of design codes*. IBRACON Structures and Materials Journal. 11(2):432-454. https://doi.org/10.1590/s1983-41952018000200011

Shahin M. A. and Cheung E. M. (2011), *Stochastic design charts for bearing capacity of strip footings*. Geomechanics and Engineering. 3(2):153-167. http://hdl.handle.net/20.500.11937/6498

Tahmasebi poor, A., Barari, M., Behnia, M. and Najafi, T. (2015), *Determination of the ultimate limit states of shallow foundations using gene expression programming (GEP) approach*. Soils and Foundations. 55(3):650-659. https://doi.org/10.1016/j.sandf.2015.04.015

Varghese, P. C. (2009), "*Design of reinforced concrete foundations*", PHI Learning Pvt. Ltd., New Delhi, India.

Yáñez-Palafox, J.A., Luévanos-Rojas, A., López-Chavarría, S. and Medina-Elizondo, M. (2019), *Modeling for the strap combined footings Part II: Mathematical model for design*. Steel and Composite Structures. 30(2):109-121. https://doi.org/10.12989/scs.2019.30.2.109

Control of reinforcement concrete in pile caps over steel piles – Case study

R. Boni[1]*, P. Helene[2] (iD)
* Contact Author: ricardo.boni@concretophd.com.br
DOI: https://doi.org/10.21041/ra.v10i2.467

ABSTRACT

This paper presents a case study about the challenges and good building practices involved in the execution of structural reinforced concrete pile caps over steel piles. The structural reinforcements were carried out in a project with 3 residential towers of approximately 30 floors each, located on the seafront. As a result, it was observed that mix design to define the type and characteristics of concrete, prototype event, particularities of the construction site, executive procedures employed, as well as the systematic monitoring and control of concreting events and other constructive stages were determining factors to promote the safety and quality of reinforcement services in accordance with the assumptions and design requirements.

Keywords: structural reinforcement; pile caps; concrete.

_____

[1] PhD Engenharia, São Paulo, Brasil.
[2] Professor Titular da Escola Politécnica da USP, PhD Engenharia, São Paulo, Brasil.

Contribution of each author

In this paper, the author R. Boni contributed with the collection of data, images and writing of the text, the author P. Helene contributed with guidance and final revision of the text. Both authors were responsible for the original idea, development, and structuring of the article.

Discussions and subsequent corrections to the publication

Any dispute, including the replies of the authors, will be published in the second issue of 2021 provided that the information is received before the closing of the first issue of 2021.

Controle do concreto de reforço de blocos de fundação sobre estacas metálicas – Estudo de caso

RESUMO

Este artigo apresenta um estudo de caso sobre os desafios, as engenhosidades e as boas práticas de construção envolvidas na execução de reforços estruturais de blocos de fundação de concreto armado sobre estacas metálicas. Os reforços estruturais em questão foram realizados em um empreendimento com 3 torres residenciais de aproximadamente 30 pavimentos tipo cada, localizado próximo da orla marítima. Como resultado, observou-se que um estudo prévio de dosagem para definição do tipo e características do concreto a ser utilizado, execução de evento protótipo de concretagem, particularidades do canteiro de obras, definição prévia dos procedimentos executivos empregados, bem como o acompanhamento e o controle sistemático dos eventos de concretagem e das demais etapas construtivas foram fatores determinantes para promover a segurança e a qualidade dos serviços de reforço em conformidade com as premissas de projeto.
Palavras-chave: reforço estrutural; blocos de fundação; concreto.

Control del hormigón de refuerzo de encepados de fundación sobre pilotes metálicos – Estudio de caso

RESUMEN

Este artículo presenta un estudio de caso sobre los desafíos, el ingenio y las buenas prácticas de construcción involucradas en la ejecución de refuerzos estructurales de encepados de fundación de hormigón armado sobre pilotes metálicos. Los refuerzos estructurales en cuestión se llevaron a cabo en un proyecto con 3 edificios residenciales de aproximadamente 30 pisos cada uno, ubicados cerca del paseo marítimo. Como resultado, se observó que un estudio previo de dosificación para definir el tipo y las características del hormigón a ser utilizado, la ejecución de un hormigonado prototipo, las particularidades del sitio de construcción, la definición previa de los procedimientos de ejecución empleados, así como el monitoreo y el control sistemático de los hormigonados y otros procedimientos de construcción fueron factores determinantes para promover la seguridad y la calidad de los servicios de refuerzo de acuerdo con las premisas de diseño.
Palabras clave: refuerzo estructural; encepado de fundación; hormigón.

1. INTRODUCTION

Located on a plot of over 7.000 m², about 250 m from the seafront in the city of Vitória, ES, Brazil. The project consists of 3 residential towers with a total of 166 units. *Tower* 1 has 33 floors and *Towers* 2 and 3 have 31 floors each.

The residential complex, whose construction was completed at the end of year 2010, also has two garage floors under the projection of the towers and the area of common use, both located above the water level, that is, without the need to use pressure slab. The structural reinforcement of pile caps of residential towers project was carried out in the first semester of 2018, between the months of January and May, due to non-conformities observed in the structure construction, verified during the partial collapse occurred in the area leisure facilities.

This paper presents the studies, the tests, the ingenuity, the good engineering practices, the procedures employed in the execution of these reinforcements and the activities developed, with emphasis on the quality control of concrete.

2. BASIC DATA OF REINFORCEMENT PROJECT AND CONCRETE MIX DESIGN

The structural reinforcement project for the residential tower pile caps was prepared according the recommendations of standard ABNT NBR 6118:2014. This project includes the reinforcement of 20 structural elements, as highlighted in Figures 1 and 2, which presents the structural reinforcements executed in floor plan and in perspective (highlighted in red), respectively.
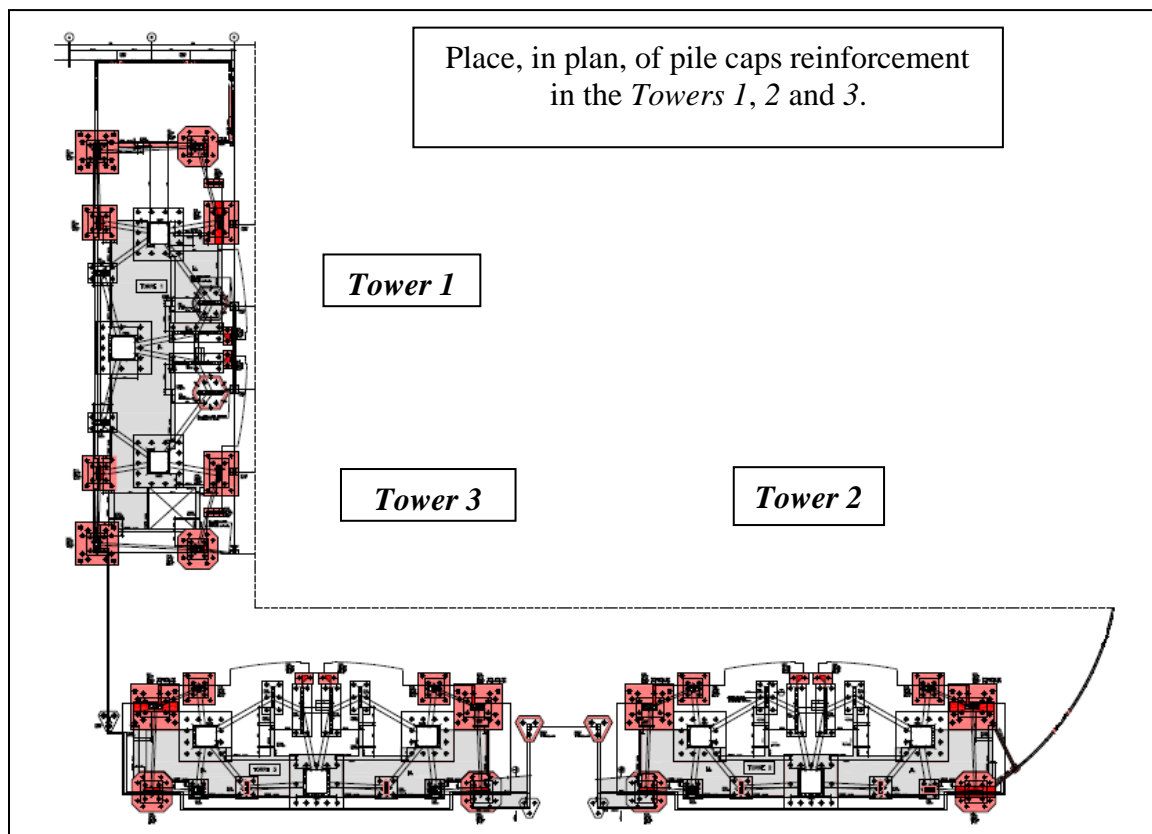

Figure 1. Location detail, in plan, of pile caps structural reinforcement in the residential towers.
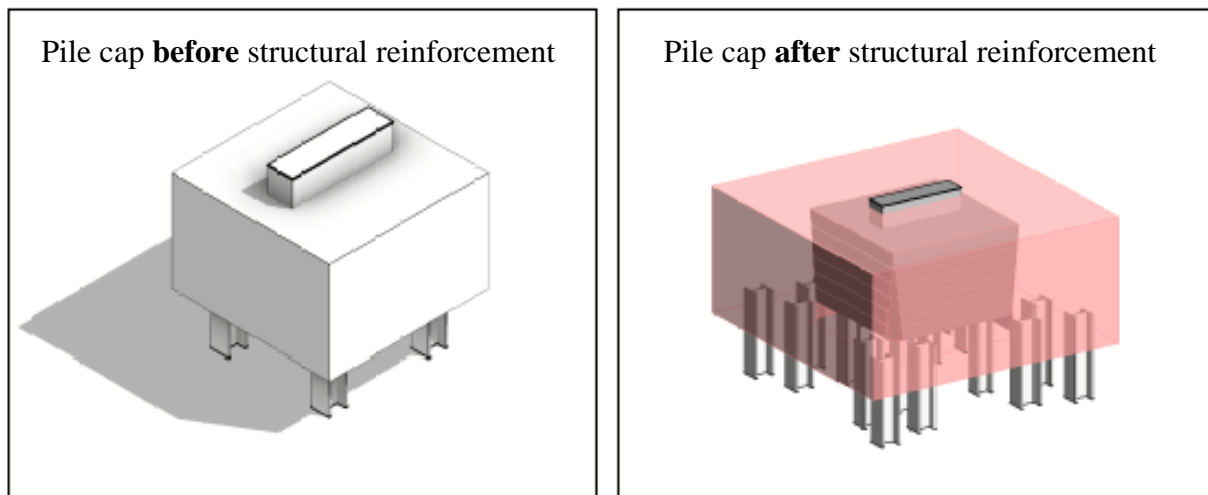
Figure 2. Generic detail in perspective from the pile caps structural reinforcement (before and after).

In Figure 2, it is noted that additional steel piles were driven into the periphery of existing piles caps. In total, 152 piles shape W200x86 and W250x115 were spiked, with a workload of 194tf and 258tf, respectively. Execution lengths ranged from 20 to 22 meters deep. The foundation reinforcement project was developed based on the requirements of standard ABNT NBR 6122:2010.

The compressive strength of concrete specified for the reinforcement of elements was $f_{ck} \geq$ 40MPa, modulus of elasticity $Ec \geq$ 32GPa, for a tension corresponding to 14MPa (0,35 fck), with a maximum w/c ratio of 0,50. This specification meets the strong environmental aggressiveness class (CAA III) required in project, according to sub-items 6.4 "*Environmental aggressiveness*" and 7.4 "*Quality of cover concrete*" of standard ABNT NBR 6118:2014.

Thus, based on design assumptions, availability of raw materials in the region, needs and particularities of the construction site a concrete mix design study was developed. For this study, the standards ABNT NBR 12655:2015 and ABNT NBR 15823:2017 Parts 1 to 6 related to self-compacting concrete were used. In addition to these standards, it also served as a reference the guidelines of the IBRACON method (TUTIKIAN, B.; HELENE, P., 2011) for the development of a self-compacting concrete, with SFII spreading class, which is shown in Table 1.

Table 1. Self-compacting concrete mix design, dry material weight, $f_{ck} \geq$ 40MPa by 28 days of age for 1m³ of concrete

Self-compacting concrete mix design, spreading class *SFII*	Design for f_{ck} 40MPa
cement consumption by m³ (CP III-40-RS)	425kg
water/(cement+addition) ratio	0,43
water	183kg
fine sand	329kg
medium sand	494kg
crushed stone 0	960kg
polyfunctional additive	2,5kg
superplasticizer additive[1]	1,5kg

(1) Fully added to the mixing central. Only in the case of eventual spreading corrections, it was allowed the additional use of this additive in construction site, in small quantities, depending on the need.

The visual aspect of concrete in question can be seen in Figures 3, 4 and 5, which show the spreading tests, passing skill in J ring and passing skill in box L, performed in accordance with standards ABNT NBR 15823-2:2017, ABNT NBR 15823-3:2017 and ABNT NBR 15823-4:2017, respectively. Still, in Figure 3, it is also possible to observe the visual stability index (IEV) of concrete that was developed especially for the structural reinforcement of pile cap on this project.

Figure 3. Detail of spreading test performed in the laboratory during the dosage study.

Figure 4. Detail of passing skill test through box L, performed in the laboratory during the dosage study.

Figure 5. Detail of passing skill test through the J ring, performed in the laboratory during the dosage study.

In order to minimize possible non-conformities related to compressive strength and elasticity modulus of concrete, it was agreed among stakeholders that, during the events of concreting the structural reinforcement, no water would be added to the balloon of the mixer truck after it left the mixing central (where the amount of mixing water is properly controlled by hydrometers).

Therefore, at the construction site, after conducting the acceptance tests (spreading measured by slump flow test), if there was a need to correct the spreading of concrete, this would be done only by means of an additive, through technical support consultant.

Also, prior to the concreting of reinforcement of pile caps, a prototype event (simulation in a concrete mixer truck) was carried out to evaluate the behavior of concrete studied in the laboratory under field conditions. It was observed that the time to transport the concrete from the mixing central to the construction site was approximately 25 minutes, a distance of 9,6 km and that the time to cast the concrete was, at most, 30 minutes, by concrete mixer truck.

At the opportunity of prototype concreting event, cylindrical specimens were also molded for compression strength tests at 3, 7, 14, 28 and 45 days of age and elasticity modulus at 28 days, as shown in Figure 6.

Figure 6. Detail of the molding of cylindrical specimens in the prototype concreting event for tests of resistance to compression and modulus of elasticity.

Based on favorable results of resistance to compression and modulus of elasticities obtained in dosage study carried out in laboratory and in the mentioned prototype event, the services for concreting the structural reinforcement of pile caps were initiated according to the steps detailed below in the sub-item *Executive Procedures*.

3. EXECUTIVE PROCEDURES

The executive procedures adopted in this case study are based on the Brazilian standards in force, mainly the standard ABNT NBR 14931: 2004 and on good engineering practices.

The services started with the driving of steel piles in the regions located around the pile caps to be reinforced, as shown in the perspective of Figure 2. These piles have depths ranging from 20 to 22 m and were spiked by adapted piles, positioned between slabs, as shown in Figure 7.
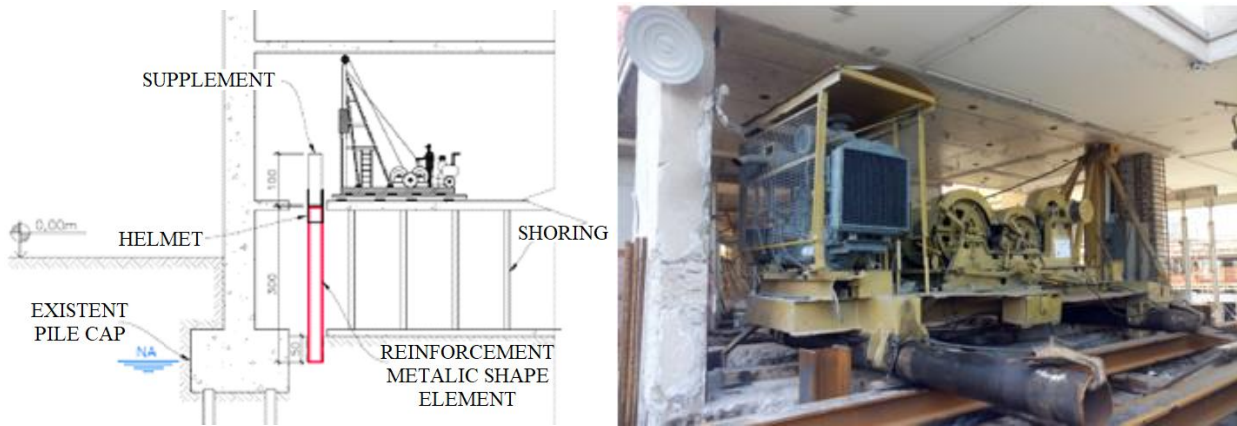
Figure 7. Detail of the adapted pile spiking positioned between slabs to perform the spiking services of the structural reinforcement piles.

Due to the difficulty of access, the dimensions of spiking equipment and the existing interference at the site, for the execution of this reinforcement step, some additional services were necessary, including:

- ✓ previously propping the ground floor slab, under which the spiking equipment were supported;
- ✓ adapt all the spiking equipment, as the height of the pile tower is much greater than the distance between slabs (ceiling height);
- ✓ execute localized demolitions and holes in the ground floor slab to allow for the spiking of steel piles;
- ✓ divide previously the steel piles (in lengths ranging from 2 to 4 m) to allow the plumb position of shape at the spiking point;
- ✓ use a supplement (above the protective helmet of the pile head) in order to help spike the shape.

In this way the metal segments piles were spiked and immediately welded to the subsequent segments, as the services progressed. Figure 8 illustrates the execution of services and the piles spiked in the periphery of one of pile caps. In the latter case, for better visualization, the image registration made after excavating the pile cap surroundings.

Figure 8. Detail of execution of spiking services (on the left) and of steel piles spiked around the pile cap to be reinforced (on the right).

After spiking all the piles of a certain pile cap, the excavation was carried out. For such, a system was installed with water level lowering pumps located in the region surrounding the pile cap (this system would be deactivated only after concreting and backfilling). The excavation was carried out with small equipment or, in most cases, manually, again due to interference and difficult access conditions.

In the sequence, the thin concrete coverage with 5 cm thickness was executed, as well measure of dimensions of existing piles caps, through the topography, possible eccentricities of existing piles (under load), as shown in Figure 9.

Figure 9. Detail of measurement dimensions of existing pile cap and of the steel piles, after excavation and execution of thin concrete.

After this stage, the services of cutting the piles began, whose top should be 35 cm above the lower level of reinforcement pile cap, and preparation of lateral surfaces of pile cap, as shown in Figure 10. In this stage, chamfers and ridges were made in the edges and lateral surfaces of pile caps, in addition to chipping of all faces, except the lower one, according to structural design requirements.

Figure 10. Detail of execution of chamfers and ridges in the edges and lateral surfaces of pile cap.

The execution of chamfers and ridges on the sides of existing blocks were essential and very important, since they aimed to guarantee the quality of concreting joint in the old concrete/new concrete interface (to be launched) and to collaborate in the transmission of efforts. The execution of chamfers on the lateral edges provided a cone-like geometry (or stopper) that dispensed the verification of adherence between the existing block and structural reinforcement.

It is recorded that the ridges were made 3 cm deep along all the lateral surfaces and the chamfers of lateral edges with dimensions varying from 0 cm (on the upper face) to 15 cm (on the lower face of pile cap), as evidenced in Figure 11.
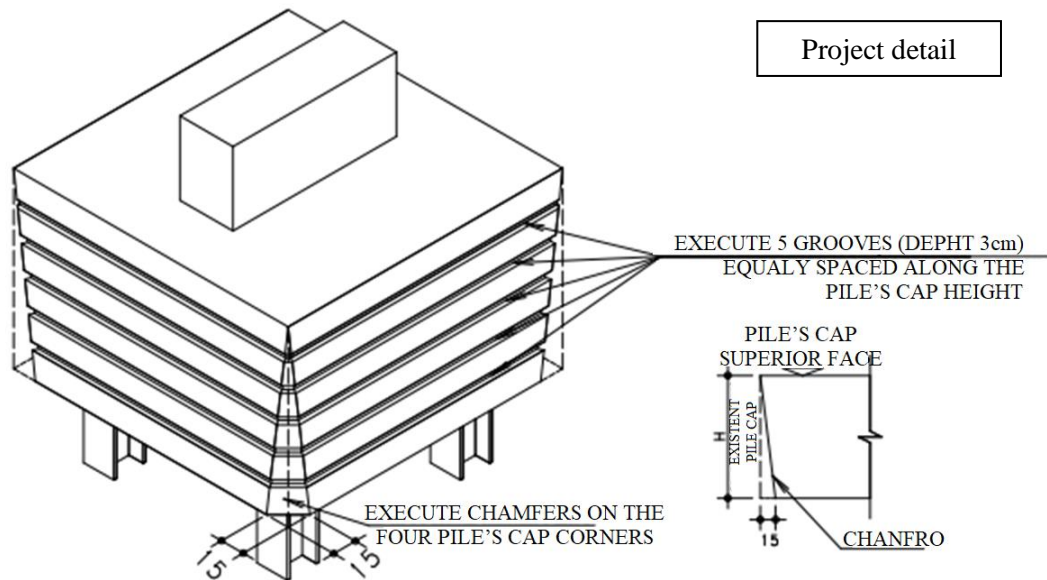
Figure 11. Detail of project indicating positioning of ridges and chamfers.

The Figure 12 shows the pile cap after the completion of concrete surface treatment services.
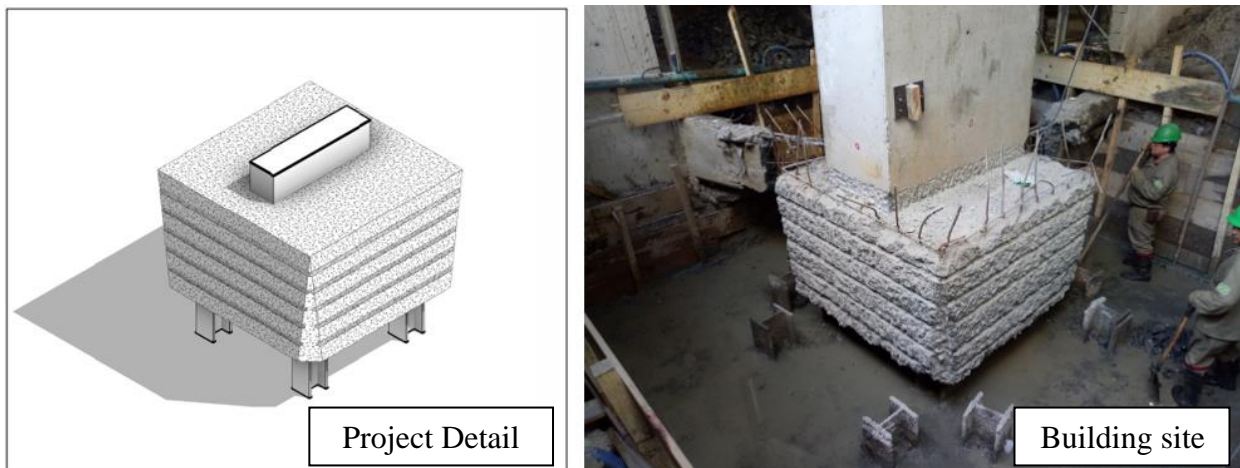
Figure 12. Detail of the surface treatment of pile cap. Detail of the project (left) and the situation "*building site*" (right).

After preparing the surface, the structural reinforcement services started by a specialized company and certified labor began, through monitoring and verification of services, with regard to positioning, gauges, number of bars and other steps involving quality control, including the use of multi-support spacers on sides and bottom of pile cap, in order to guarantee the specified coverage of project (40 mm).

It is recorded that that the steel bars used in the structural reinforcement of pile caps (gauges 25 mm, 20 mm, 16 mm and 12,5 mm) were delivered to the work cut/folded and properly identified. Figure 13 shows the execution of reinforcement frame services for the pile caps.

Figure 13. Detail of execution of reinforcement frame services of pile caps.

Upon verification of frame and release by the engineering staff, initiated the assembling the wooden forms and shoring, as shown in Figure 14. All of these services were also monitored and checked for flatness, plumbs, dimensions, locking system and water tightness.

Figure 14. Detail of the formwork of structural reinforcement pile caps.

Finishing the structural reinforcement services, the concreting of reinforcement structural element was carried out, through the use of self-compacting, pumped concrete, as detailed in item 2 "*Basic Data of Reinforcement and Concrete Design*" of this paper. Figure 15 shows the visual aspect of concrete observed in the field.

Figure 15. Visual aspect of self-compacting concrete used to reinforce structural pile caps.

At this stage, it was indispensable that the concrete was cast at a low speed to avoid trapping air on the lower surface of pile cap, thus avoiding possible hidden concrete failures. In order to avoid non-conformities of this nature, the concrete from the lower portion of pile cap was launched slowly, on only one side of pile cap, and moderately vibrated with immersion vibrators with a diameter needle of 40 mm.

It is important to note that the treated surface of existing pile cap, the region of interface with the new concrete, was previously cleaned with a pressurized water jet, in order to remove all dust, powdery material or any other type of contaminant. The self-compacting concrete was cast on a clean surface in a dry saturated condition.

The Figure 16 shows the concreting event of reinforcement of one pile cap, performed with self-compacting concrete, respecting the premises mentioned in the previous paragraph.

Figure 16. Detail of the concreting of reinforcement of pile cap, made with self-compacting concrete.

On the receipt of concrete at building site, spreading tests (*slump flow test*) were carried out on all concrete mixer trucks, by specialized laboratory, according to recommendations of standard ABNT NBR 15823-2:2017. In these cases, the spreading class, the visual stability index obtained, as well as the visual aspect of concrete, which should be cohesive, with no exudation or apparent segregation were observed and analyzed. As previously noted, in the case of need for correction spreading, only superplasticizer additive was used, under no circumstances was the spreading corrected by adding water on the construction site.

In addition to the receiving tests mentioned in the previous paragraph, whenever possible, technical visits were made to the concrete batching central, in order to monitor the concrete production procedures, with regard to the control of inputs, tests to determine the moisture content of fine aggregates, dosage, mixture and other steps.

In order to minimize the risk of fissuration, after concreting, the side forms were maintained for a period of 3 days in order to avoid the surface evaporation of water. In addition, the top face of pile cap was always kept moist, by aspersion potable water, in order to guarantee ideal curing conditions.

Subsequently, after removing the formwork, thorough inspections were carried out on all surfaces of reinforcement performed and in the regions of new concrete/old concrete interface. It is registered that no type of non-conformity was found related to concreting failure, fissures etc.

Figure 17 shows the visual aspect and the surface finish of concrete in the hardened state applied in the reinforcement of pile caps.

Control of reinforcement concrete in pile caps over steel piles – Case study

Figure 17. Detail of the visual aspect and the surface finish of concrete of reinforced pile caps.

Soon after the inspection, the blocks were released to be grounded. For this, a mechanical compactor was used.

With regard to technological control of concrete, 6 specimens were molded per concrete mixer truck to perform compression resistance tests at the ages of 7, 28 and 45 days (2 per age), using the total sampling criterion, according to item 6.2.3.1 "*Control of concrete by total sampling (100%)*" of standard ABNT NBR 12655:2015.

The specimens were molded, stored and transported in accordance with the requirements of standard ABNT NBR 5738:2015. It is noteworthy that the specimens molded for the 45 days of age would only be tested in the case of identification of non-conformities related to the compressive strength at 28 days. The results obtained are detailed below.

4. RESULTS OBTAINED

Considering the executive procedures described above and the good engineering practices adopted, the results obtained are presented below, regarding the integrity and quality of concrete used.

After concreting and carrying out visual inspections on all reinforcements of pile caps, it was found that they did not show any fissures resulting from the retraction phenomenon or any other type of material failure that could compromise their integrity, its durability and service life of structure.

Regarding the technological control of concrete applied in the structural reinforcement of pile caps on residential towers, Figure 18 graphically presents the results of concrete compressive strength at 7 and 28 days of age of 66 concrete mixer trucks (100% sampling), in the form of chart

As can be seen, the average resistance obtained was 45,2MPa, standard deviation of 2,9 MPa, coefficient of variation equal to 6,4% and with extreme values ranging from 40,7 MPa (minimum) to 53,9 MPa (maximum). Considering the resistance specified in the project, it is registered that all results are in compliance.
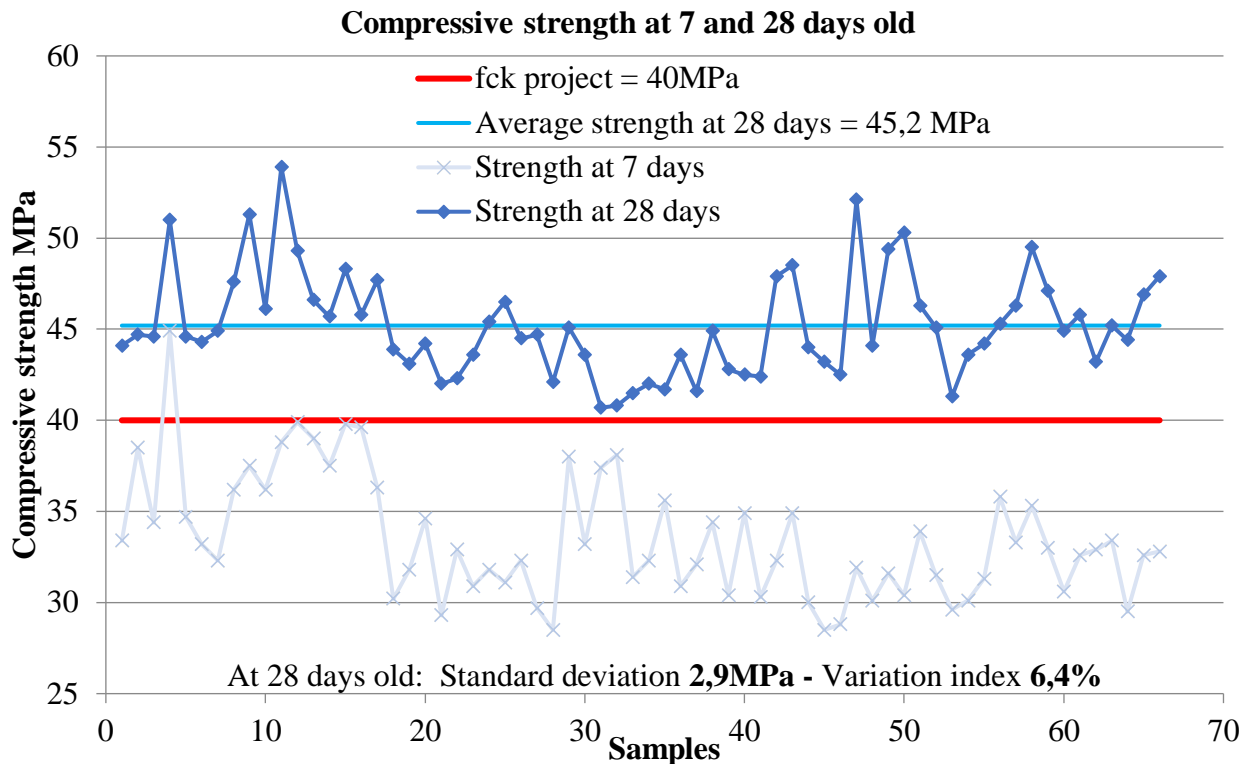
Figure 18. Concrete individual chart of values fck 40MPa, self-compacting used in the structural reinforcement of pile caps.

5. FINAL CONSIDERATIONS

This article aimed to highlight that simple recommendations coherent with the current standardization and good constructive practices, previous studies, as well as the systematic control and technical monitoring of activities that preceded and followed the concreting events, were sufficient to promote an upstanding structural element and a satisfactory final result in accordance with the project requirements.

6. ACKNOWLEDGEMENTS

Special thanks are due to the professionals from companies and offices responsible for the preparation of Geoconsult foundation project, for the structural reinforcement project França & Associados, for the construction Cyrela and for the supply of concrete Concrevit, which together with the consulting of PhD Engenharia made this possible achievement with quality.

7. BIBLIOGRAPHIC REFERENCES

Associação Brasileira de Normas Técnicas. (2014). *NBR 6118: Projeto de estruturas de concreto - Procedimento*. Rio de Janeiro.
Associação Brasileira de Normas Técnicas. (2004). *NBR 12655: Concreto de cimento Portland – Preparo, controle, recebimento e aceitação - Procedimento*. Rio de Janeiro.
Associação Brasileira de Normas Técnicas. (2004). *NBR 14931: Execução de estruturas de concreto - Procedimento*. Rio de Janeiro.
Associação Brasileira de Normas Técnicas. (2010). *NBR 6122: Projeto e execução de fundações*. Rio de Janeiro.

Control of reinforcement concrete in pile caps over steel piles – Case study

Associação Brasileira de Normas Técnicas. (2015). *NBR 5738: Procedimento para moldagem e cura de corpos de prova*. Rio de Janeiro.

Associação Brasileira de Normas Técnicas. (2017). *NBR 15823-1: Concreto autoadensável. Parte 1: Classificação, controle e recebimento no estado fresco.* Rio de Janeiro.

Associação Brasileira de Normas Técnicas. (2017). *NBR 15823-2: Concreto autoadensável. Parte 2: Determinação do espalhamento, do tempo de escoamento e do índice de estabilidade visual – Método do cone de Abrams.* Rio de Janeiro.

Associação Brasileira de Normas Técnicas. (2017). *NBR 15823-3: Concreto autoadensável. Parte 3: Determinação da habilidade passante – Método do anel J.* Rio de Janeiro.

Associação Brasileira de Normas Técnicas. (2017). *NBR 15823-4: Concreto autoadensável. Parte 4: Determinação da habilidade passante – Método da caixa L e da caixa U.* Rio de Janeiro.

Helene, P., Terzian, P. (1993), "*Manual de dosagem e controle do concreto*". PINI/SENAI, São Paulo, Brasil, p. 349.

Tutikian, B., Helene, P. (2011), *"Dosagem dos Concretos de Cimento Portland"* In. Geraldo C. Isaia (Org.). Concreto: Ciência e Tecnologia. 1 ed. São Paulo: Ibracon, 2011, v. 1, p. 415-451.

Revista ALCONPAT

Time variability analysis for damage detection in flexible pavement using infrared thermography

M. Pacara-Copa[1]* 🆔, J. H. A. Rocha[2] 🆔, J. S. Ledezma-Perez [1]🆔

*Contact author: marinapacara@gmail.com

DOI: https://doi.org/10.21041/ra.v10i3.468

ABSTRACT

This document discusses the time range to optimize and understand infrared thermography results when used on damage detection for flexible pavement. A monitoring activity was performed during 14 continuous hours (5:00 a.m. to 7:00 p.m.) for four study areas in a centrally located avenue in Cochabamba City, Bolivia. This activity evidenced an effective time range to take thermographic images from 11:00 a.m. to 4:00 p.m. Damage visualization by differential colorimetry in thermograms at different times was also verified. This test enables locating areas where a detailed inspection may be performed. As a limitation, its sensibility to changes under environmental conditions is evident.

Keywords: infrared thermography, flexible pavement, inspection.

[1] Departamento de Ingeniería Civil, Facultad de Ciencias y Tecnología, Universidad Mayor de San Simón, Cochabamba, Bolivia.

[2] Departamento de Ingeniería Civil, Facultad de Tecnología, Universidad Privada del Valle, Cochabamba, Bolivia.

Contribution of each author

In this work the author M. Pacara-Copa contributed with the original idea, field work and monitoring, data collection, choice and development of the work methodology, writing of the work and discussion of results; the author JHA Rocha contributed with the choice and development of the work methodology, data collection, discussion of results and review of the work writing, and the author JS Ledezma P. contributed with the discussion of results and review of the manuscript.

Discussions and subsequent corrections to the publication

Any dispute, including the replies of the authors, will be published in the second issue of 2021 provided that the information is received before the closing of the first issue of 2021.

Análisis de la variabilidad horaria para la detección de daños en pavimentos flexibles usando termografía infrarroja

RESUMEN

En este trabajo se discute el rango horario para optimizar e interpretar los resultados de la termografía infrarroja cuando es utilizada en la detección de daños de pavimentos flexibles. Se realizó un seguimiento de 14 horas continuas (5:00 a.m. a 7:00 p.m.) para cuatro zonas de estudio en una avenida céntrica de la ciudad de Cochabamba, Bolivia. El seguimiento evidenció un rango horario óptimo para la toma de imágenes termográficas de 11:00 a.m. hasta las 4:00 p.m.; también se constató la visualización del deterioro mediante la colorimetría diferenciada en los termogramas a diferentes horas. Este ensayo permite localizar las áreas en las que se puede efectuar una inspección detallada. Como limitante se tiene su sensibilidad a cambios en las condiciones ambientales.
Palabras clave: termografía infrarroja; pavimento flexible; inspección.

Análise do melhor horário para a detecção de danos em pavimentos flexíveis usando termografia infravermelha

RESUMO

Este trabalho discute o intervalo de tempo para otimizar e interpretar os resultados da termografia infravermelha quando é usada para detectar danos em pavimentos flexíveis. Um acompanhamento de 14 h contínuas (5h às 19h) foi realizado para quatro áreas de estudo em uma avenida central na cidade de Cochabamba, Bolívia. O acompanhamento mostrou um intervalo de tempo ideal para a obtenção de imagens termográficas a partir das 11h até às 16h. A visualização da deterioração também foi verificada pela colorimetria diferenciada nos termogramas em diferentes momentos. Este teste permite localizar áreas onde uma inspeção detalhada pode ser feita. Como limitação observa-se a sua sensibilidade às mudanças nas condições ambientais.
Palavras-chave: termografía infravermelha; pavimento flexível; inspeção.

Time variability analysis for damage detection in flexible pavement using infrared thermography
Pacara-Copa, M., Rocha, J. H. A., Ledezma-Perez, J. S.

351

1. INTRODUCTION

Road infrastructure works are very important for socioeconomic development in any country, since they allow for mobilization of people and goods (Vyas *et al*., 2019). However, these works suffer damages (fissures, deformation, delamination, etc.); therefore inspection, maintenance and reconditioning activities are required in order to guarantee their useful life and provide optimal service conditions (Solla *et al*., 2014).

In Bolivia, road maintenance and conservation started when the Bolivian-American Cooperation Road Service (*Servicio Cooperativo Boliviano Americano de Caminos-SCBAC*) was founded in 1955 (Lovera, 2017). Later, in 1961, National Road Service Agency (*Servicio Nacional de Caminos - SNC*) was created. This entity was in charge of managing and maintaining roads all over the country. In 2006 it was replaced by Bolivian Road Administration Agency (*Administradora Boliviana de Carreteras - ABC*) according to Law 3507 (Bolivia, 2006a), whose institutional mission is to integrate the country by planning and managing the Main Road Network (*Red Vial Fundamental - RVF*) (Bolivia, 2006b). ABC activities include: planning, management, study and engineering, construction, maintenance, preservation and operation for RVF and its access roads (ABC, 2011).

Despite standards and institutions in charge of road conservation, a great percentage of roads show visible issues in Bolivia, mainly on flexible pavement (*Los Tiempos*, 2016, 2019; *Opinión*, 2018). Timely care for road maintenance and/or rehabilitation exceeds capacity of pertinent entities such as ABC. This situation is caused by lack of inspection techniques. Many main roads, mostly in cities, are not properly inspected to minimize of traffic interruption. This aspect avoids appropriate evaluation and diagnosis of current conditions on flexible pavement. Therefore, actions taken for rehabilitation are incorrect or improvised in many cases.

Some methods for infrastructure inspection in both concrete or flexible pavement bridges and roads are bibliographically available (Rehman *et al*., 2016; Janků *et al*., 2019; Dong *et al*., 2016). The most widely used method is the ground-penetrating radar (georadar) (Khamzin *et al*., 2017; Fernandes & Pais, 2017; Tosti *et al*., 2018). Nevertheless, a direct contact with infrastructure and interrupting vehicle traffic are required. Hence, techniques for an inspection without traffic interruption and remotely efficient are required. Accordingly, infrared thermography rises as an alternative for this purpose. This technique does not required direct contact with the inspected subject and may be performed at different distance rates. (Baggathiappan *et al*., 2013; Rocha *et al*., 2017).

Although inspection studies for pavement using infrared thermography are available (Garrido *et al*., 2018; Golrokh and Lu, 2019), bibliography related to flexible pavement is scarce (Solla *et al*., 2014; Lin *et al*., 2018; Vyas *et al*., 2019). Therefore, evaluating capacities and limitations -as an inspection method for flexible pavement mostly in situ is still required, since reported information is experimental and has been applied in different places.

In this sense, this document is intended to discuss a time range to optimize and understand infrared thermography results when used for damage detection on flexible pavement, considering two sections of San Martin Avenue in Cochabamba City, Bolivia as a study case. This selected section is characterized by showing high vehicle traffic and jam as well as damaged flexible pavement (Los Tiempos, 2016).

2. INFRARED THERMOGRAPHY

Thermal radiation is the type of electromagnetic radiation that comprises heat transference and it is emitted as a consequence of energy transition in molecules, atoms and electrons. The intensity of infrared radiation emitted by a body depends on the temperature of its surface. Thereby, it is considered that any body whose temperature is above absolute zero (0 K) emits infrared radiation (Rocha et al., 2017).
Thermal energy irradiated by an object is expressed according to the energy emitted by a perfect radiator called a black body or ideal emitter (Cengel, 2003).
The human eye may see radiation in the electromagnetic spectrum between 0.4 – 0.7 μm (visible spectrum), the infrared band ranges 0.9 – 14 μm, equipment being necessary for its detection. Thermographic cameras, used for inspection, work in this infrared band. The ratio between electromagnetic radiation and temperature is explained through Stephan-Boltzman Law equation (1) (Baggathiappan et al., 2013).

$$W = \sigma * \varepsilon * T^4 \qquad\qquad (1)$$

Where W is radiation intensity (w/m2), σ is Stephan – Boltzmann Constant (5.67*10-8 W/m2*K4), ε is surface emissivity, and T is temperature measured (K).

3. PROCEDURE

In order to meet the objective intended in this article, a monitoring activity during 14 continuous hours was performed on July 20 to 27, 2020. Thermographic images were taken every hour, considering midday as a time axis, meaning 7 hours before and 7 hours after were considered. Monitoring time range was from 5:00 a.m. to 7:00 p.m.
Two sections were considered as case study: the first was located on San Martin Avenue between Jordan and Sucre Streets, where Palace of Justice is across from 25 de Mayo Market, and the second was on San Martin Avenue between Heroinas Avenue and Colombia Street where many stores and optical shops are located.
Each study section was divided in two areas to take thermograms. Figure 1 shows the areas where thermografic images were taken. Area 1 is located on the corner of San Martin Avenue and Jordan Street on the southeastern sidewalk, where panoramic images of the whole sidewalk were taken. Area 2 is located in the middle of Section 1: San Martin Avenue between Jordan and Sucre Streets on the eastern sidewalk. Area 3 is located in the intersection of San Martin Avenue and Heroinas Avenue on the central green space. Area 4 is located in the middle of Section 2 on San Martin Avenue between Heroinas Avenue and Colombia Street.
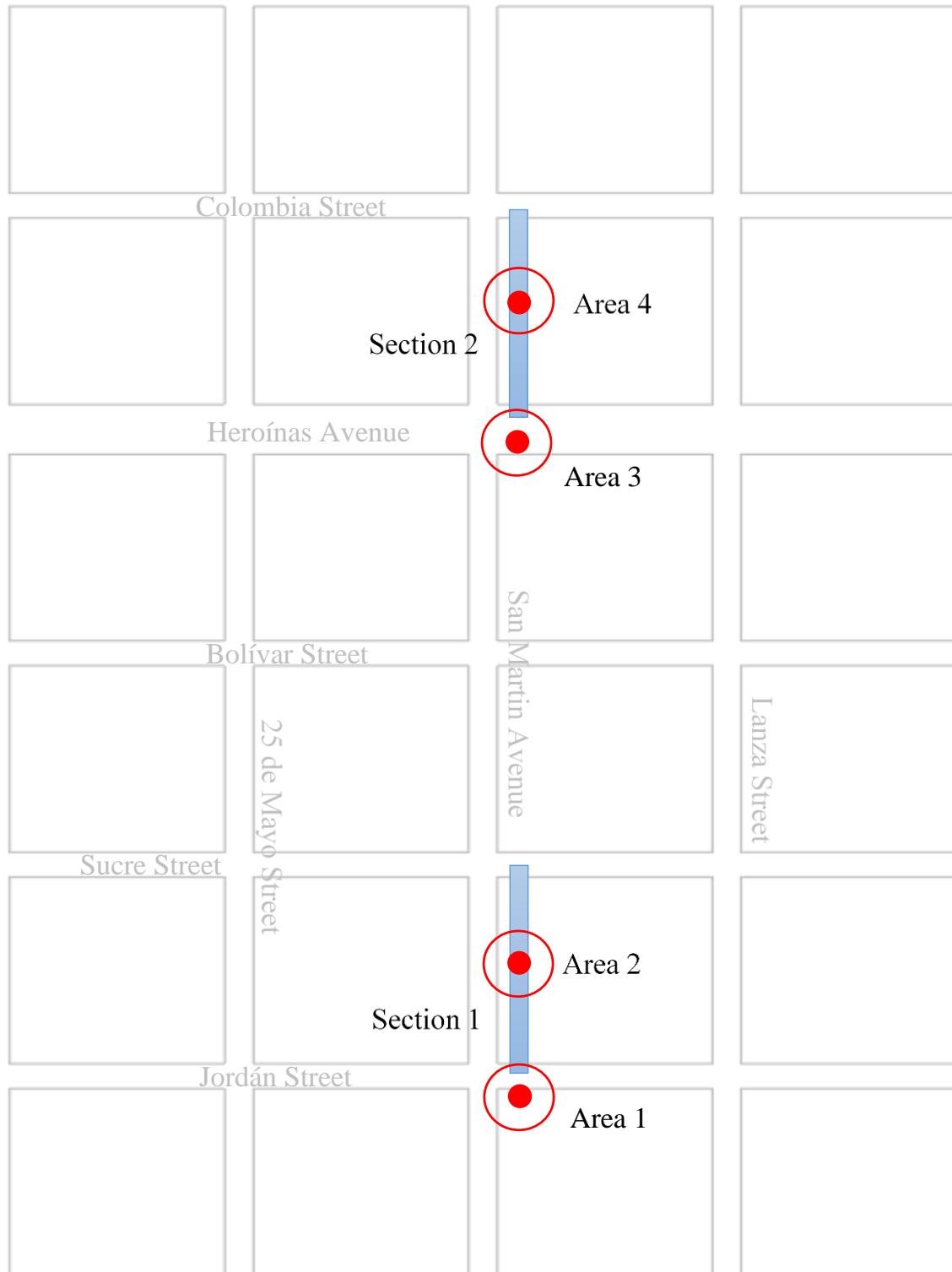
Figure 1. Areas to take thermografic images.

The equipment used was a CAT S60 equipped including an FLIR integrated camera, whose characteristics are detailed in Table 1.

Time variability analysis for damage detection in flexible pavement using infrared thermography
Pacara-Copa, M., Rocha, J. H. A., Ledezma- Perez, J. S.

Table 1. S60 MyFLIR specifications.

Thermal and visual camera including MSX	
Thermal Sensor	Pixel size: 17 mm. Spectral range: 8 to 14 mm.
Thermal Resolution	80 x 60
Visual Resolution	640 x 480
HFOV/VFOV	46º ± 1º/35º±1º
Image Frequency	8,7 Hz
Focus	Fixed 15 cm – Infinite
Integrated in Shutter	Automatic/manual
Radiometry	
Dynamic scene range	-20ºC - 120ºC
Precision	±5ºC o ±5%
	Difference percentage between ambient temperature and scene
	60 s applicable after start when unit is located between 15ºC and 35ºC, and the scene is located between 10ºC and 120ºC.
Thermal Sensitivity (MRDT)	150 mK

Source: FLIR (2016)

Thermograms resulting from monitoring (including a 1-hour interval) were processed and analyzed by *FLIRTools* program.

Besides being a tool that facilitates inspection reports, *FLIRTools* edits and analyzes images quickly, for this program has an option to adjust and modify parameters and enables scaling temperature ranges and/or change colorimetry according to any scenario relevant to the study.

4. RESULTS

Results submitted are dated July 22, 2018, because it enabled detection of thermal gradients and data repeatability. It is worth mentioning that due to technique sensitivity to environmental conditions (intermittent cloudiness and rain) many days were interrupted or excluded for this activity.

Thermograms for all four areas were analyzed in a visual manner, in the first intances, and then in a quantitative manner, in order to determine the optimal range for data collection to detect damage in flexible pavement. At the same time, qualities of *FLIRTools* were analyzed for the benefit of proposed technique.

4.1 Visibility of damage on paving surface in thermographic images
After in situ monitoring, damage visibility in thermografic images was verified. Figure 2 shows Area 4, and Figure 3 shows the corresponding thermogram.
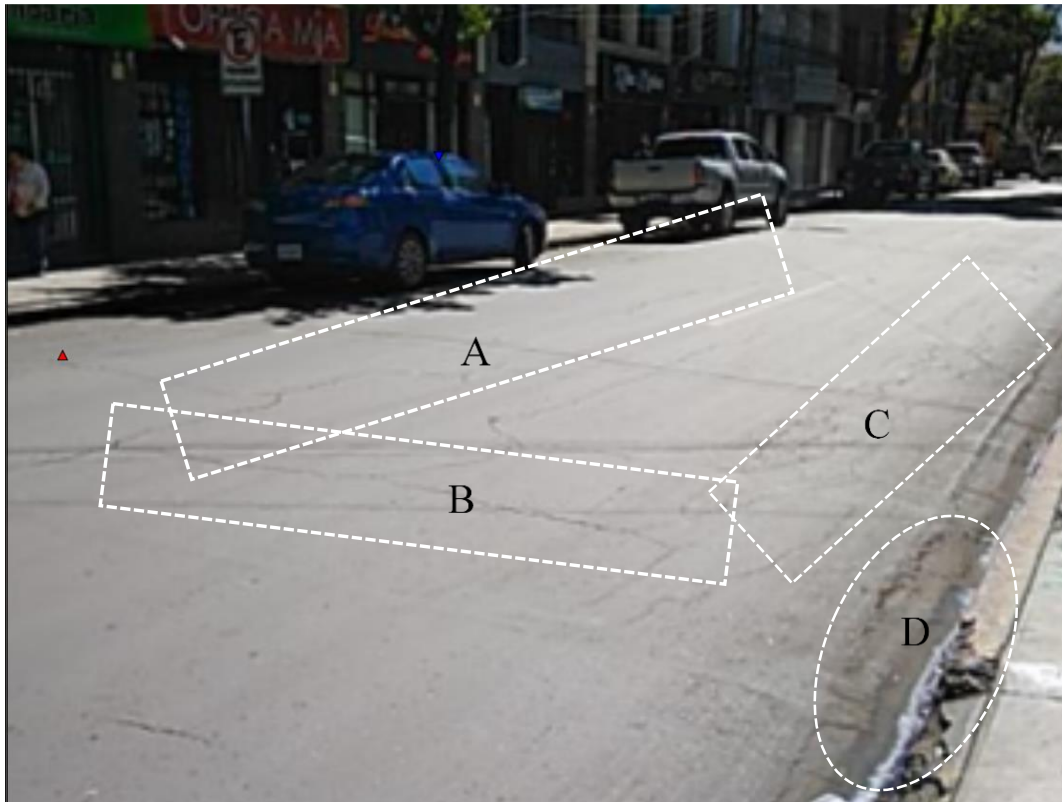
Figure 2. Digital image for Area 4.

34.9°C

26.0°C
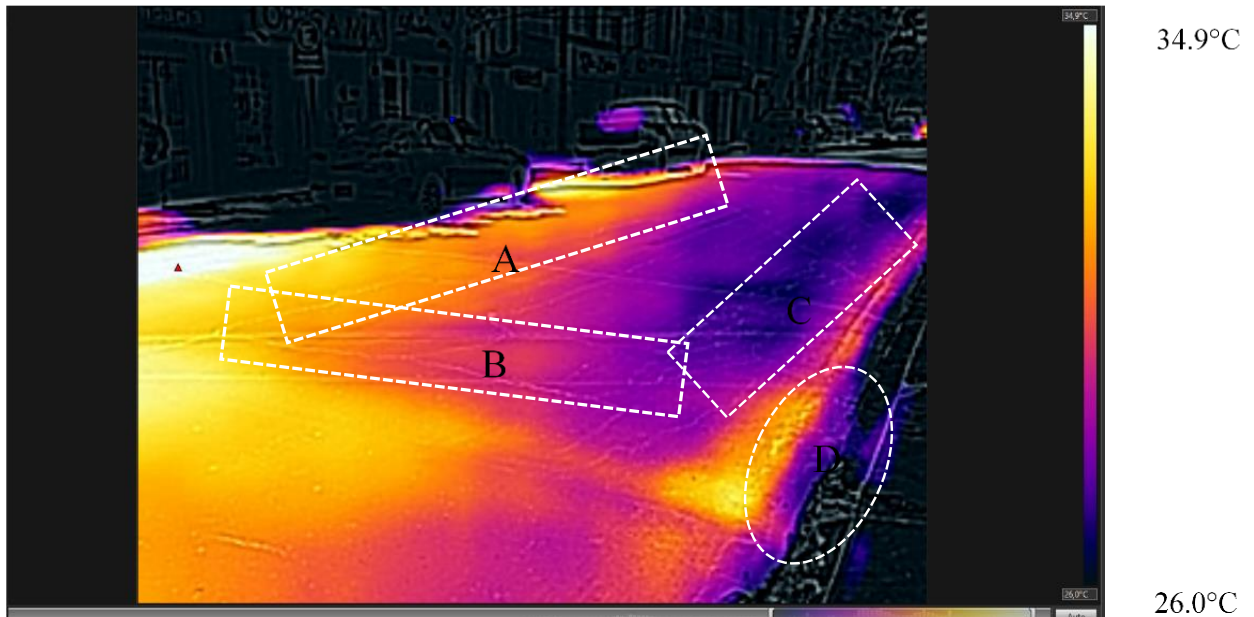
Figure 3. Thermal image for Area 4.

Figure 2 shows transversal (B) and longitudinal (A) cracking, crocodile leather texture (C), and aggregate detachment (D) among other defect appearances. Figure 3 shows the thermographic image of previously mentioned area, where varied colorimetry can be seen. This evidences a previous relation to damages observed in Figure 2.

It can be noticed that the thermographic image in Figure 3 shows the temperature ranges on the right side; this range varies from 26°C to 34.9°C. Yellow with white tendency areas represent high temperatures and blue with black tendency areas represent low temperatures. This color pallet may

356

Time variability analysis for damage detection in flexible pavement using infrared thermography
Pacara-Copa, M., Rocha, J. H. A., Ledezma- Perez, J. S.

be modified at user convenience. However, no uniformity in asphaltic pavement is observed, since cold and hot areas are distinguished.

4.2 Variation in thermographic images at different times
Differential colorimetry in Area 1 at different times of the day was visually analyzed under the same temperature range with *FLIRTools* program. Figure 4 shows thermographic images in Area 1 during three different times and under the same temperature range. This temperature was 23°C as the maximum and 16°C as the minimum range. Figures 4a, 4b y 4c represent 7:00 a.m., 1:00 p.m. and 6:00 p.m., respectively.

Figure 4. Visibility of thermografic images at different day times in Area 1.
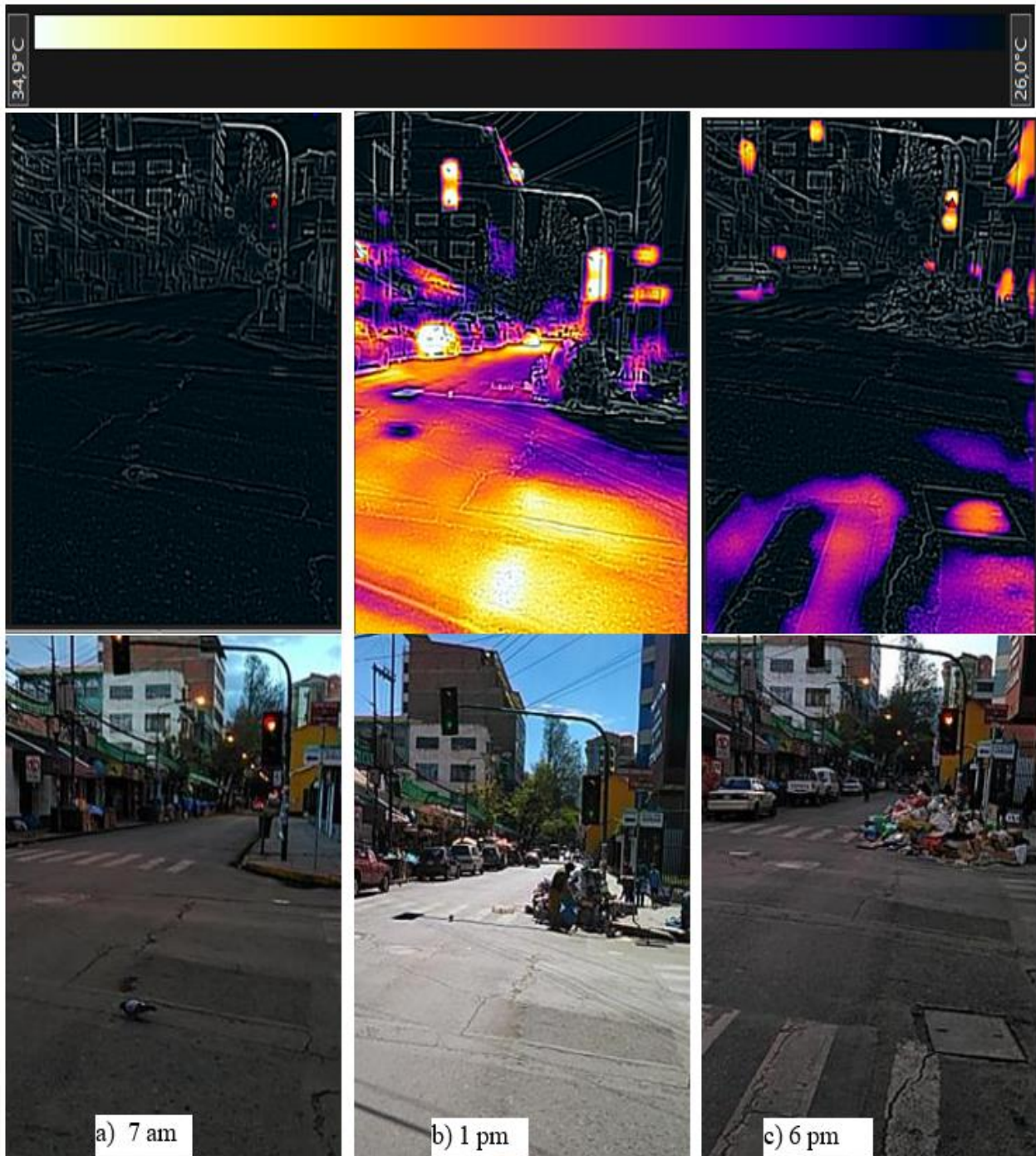
When observing thermographic images related to digital images, it can be noticed that Figure 4b, representing 1:00 p.m., shows flexible asphalt showing different temperatures on its surface, unlike Figure 4a (7:00 a.m.) that shows no difference in pavement temperatures. Figure 4c (6:00 p.m.) shows that only some areas in pavement reveal temperatures close to maximum value, according to temperature range established.

4.3 Determining optimal time range during daytime to take thermographic images
In order to determine optimal time range to take thermographic images, temperature difference in two sections with different characteristics was used in order to obtain a differential that might be evaluated by a graphics.
In order to obtain the difference in temperatures, the equation (2) was used, which is an expression proposed in bibliography for a qualitative and quantitative analysis of results (Washer *et al*., 2010; Farrag *et al*., 2016; Rocha *et al*., 2017).

$$\Delta T = Tc - Tf \qquad (2)$$

Where ΔT is the differential or thermal gradient (°C), Tc is the temperature of damaged area in the study (°C), and Tf is the temperature of an area other than the damaged one (°C).
Figures 5, 6, 7 and 8, show temperature variation during monitoring period for two points with different characteristics. Each figure shows results for each of all four analyzed areas, this is to distinguish the thermal differential or temperature gradient (ΔT).
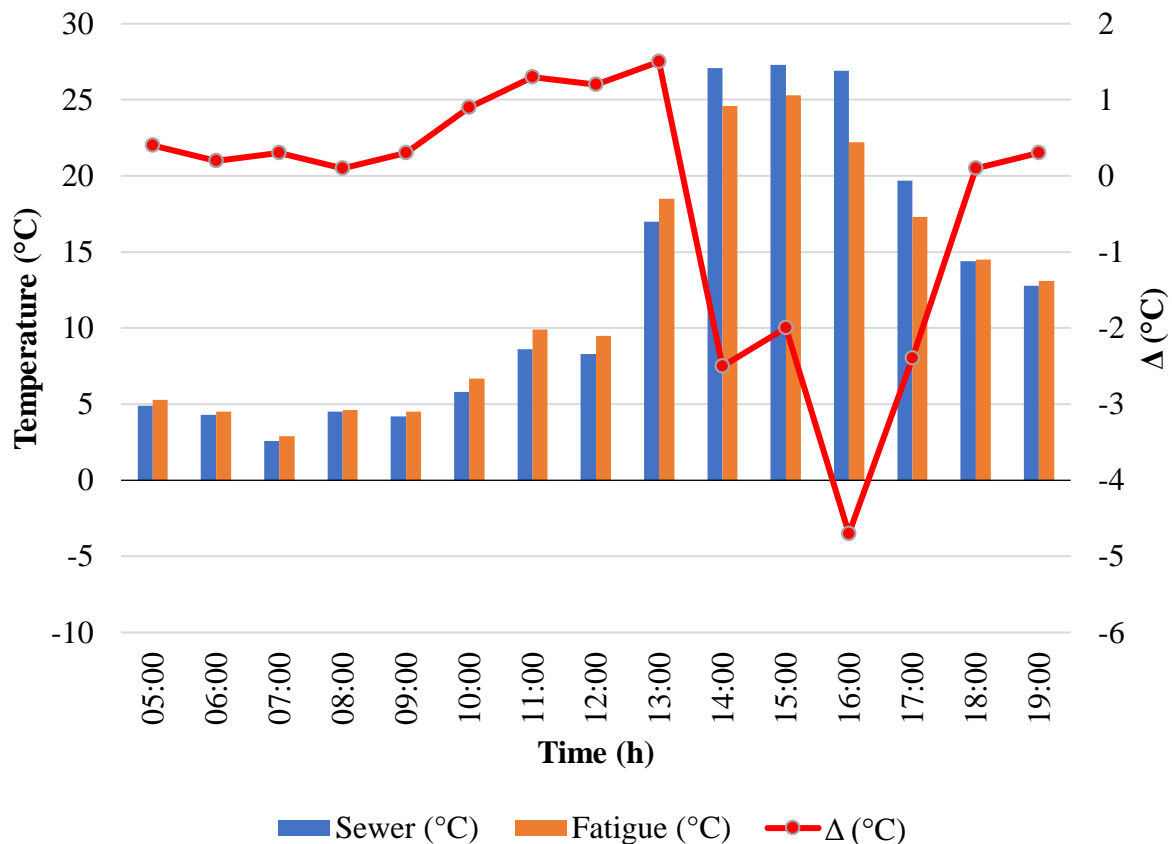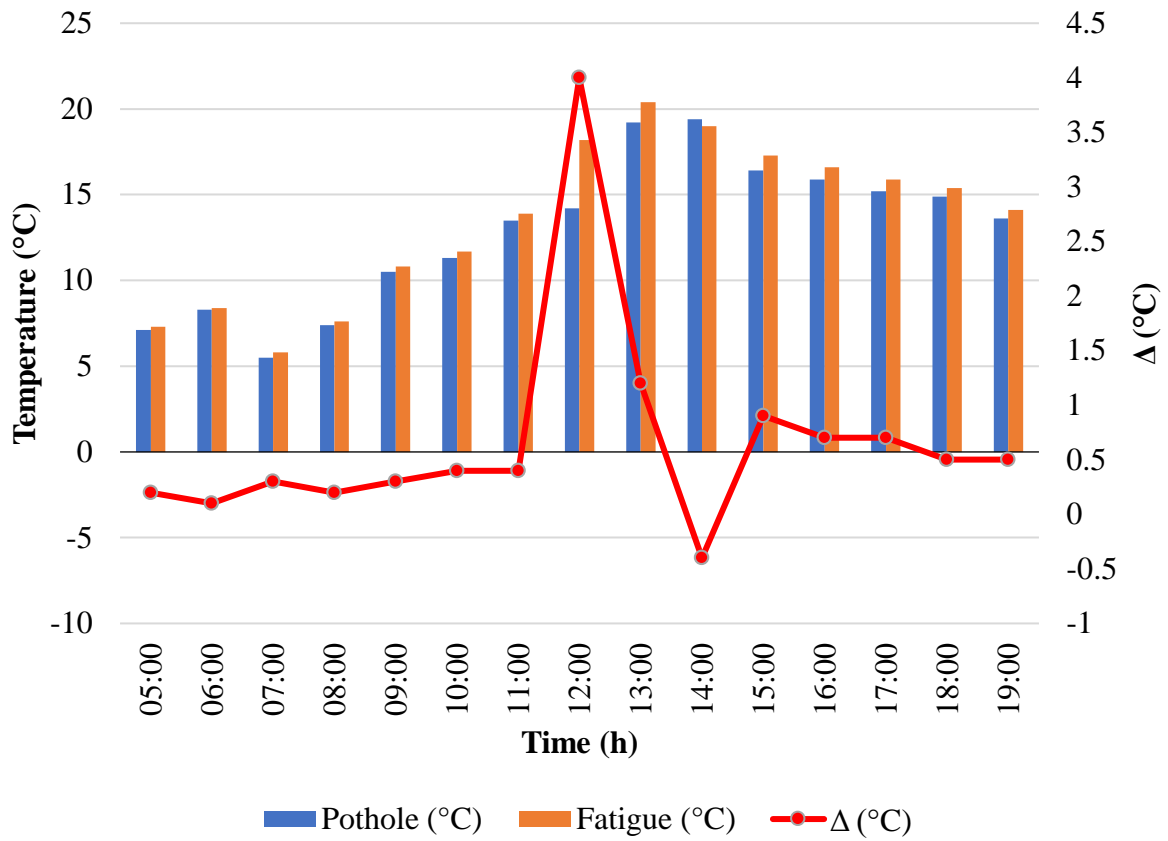

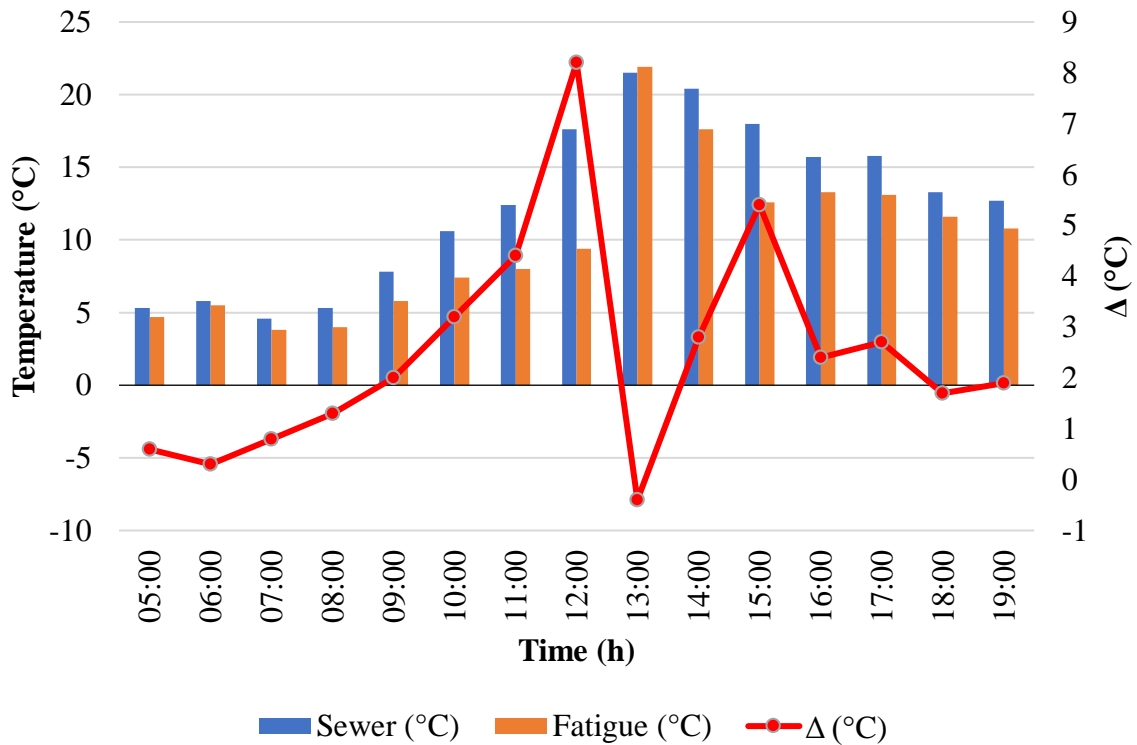Figure 5. Temperatures in Area 1.

Figure 6. Temperatures in Area 2.

Figure 7. Temperatures in Area 3.
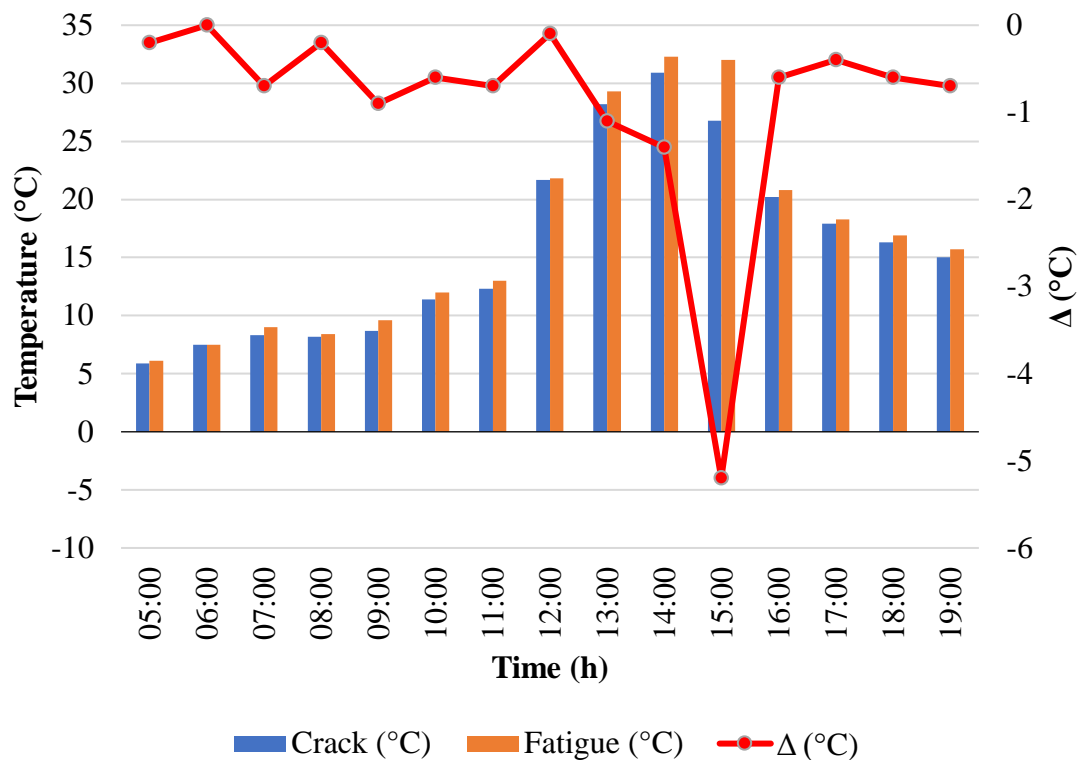
Figure 8. Temperatures in Area 4.

Figure 9 shows temperature differential (ΔT) for all four areas regarding time as well as ambient temperature and relative humidity. Maximum values for thermal gradients given between 11:00 a.m. and 4:00 p.m. are shown. It can also be seen that between 5:00 a.m. and 8:00 a.m., differential values are minimal, being this an ineligible period for an appropriate analysis. The period from 4:00 p.m. to 7:00 p.m. shows small differential values, due to cooling process (evening). Once solar radiation is absent, heated sections tend to balance with the environment (Washer *et al.*, 2010), Figure 4c. It can be observed that the best period is between 11:00 a.m. and 4:00 p.m. because a greater differential in temperature is present, which enables visualization of defect appearances in thermograms. This is consistent with other investigations indicating that whenever thermal gradients are higher, defect appearances are detected (Solla *et al.*, 2014; Farrag *et al.*, 2016; Rocha *et al.*, 2017).

Regarding thermal gradient behavior with ambient temperature and relative humidity, it can be observed that maximum gradients occur when ambient temperature is high and relative humidity is low. Otherwise, when ambient temperature is low relative humidity is high, lower thermal gradients are present, 5:00 a.m. to 8:00 a.m., which confirm this technique is sensitive to environmental conditions (Rocha & Póvoas, 2017).

Even though this article was only applied in a single period of the year, this technique may be used in any season. Solar exposure and a high ambient temperature are required. Nevertheless, optimal periods for inspection will change according to the season, depending on times of exposure to solar radiation and ambient temperature (Washer et al., 2010).
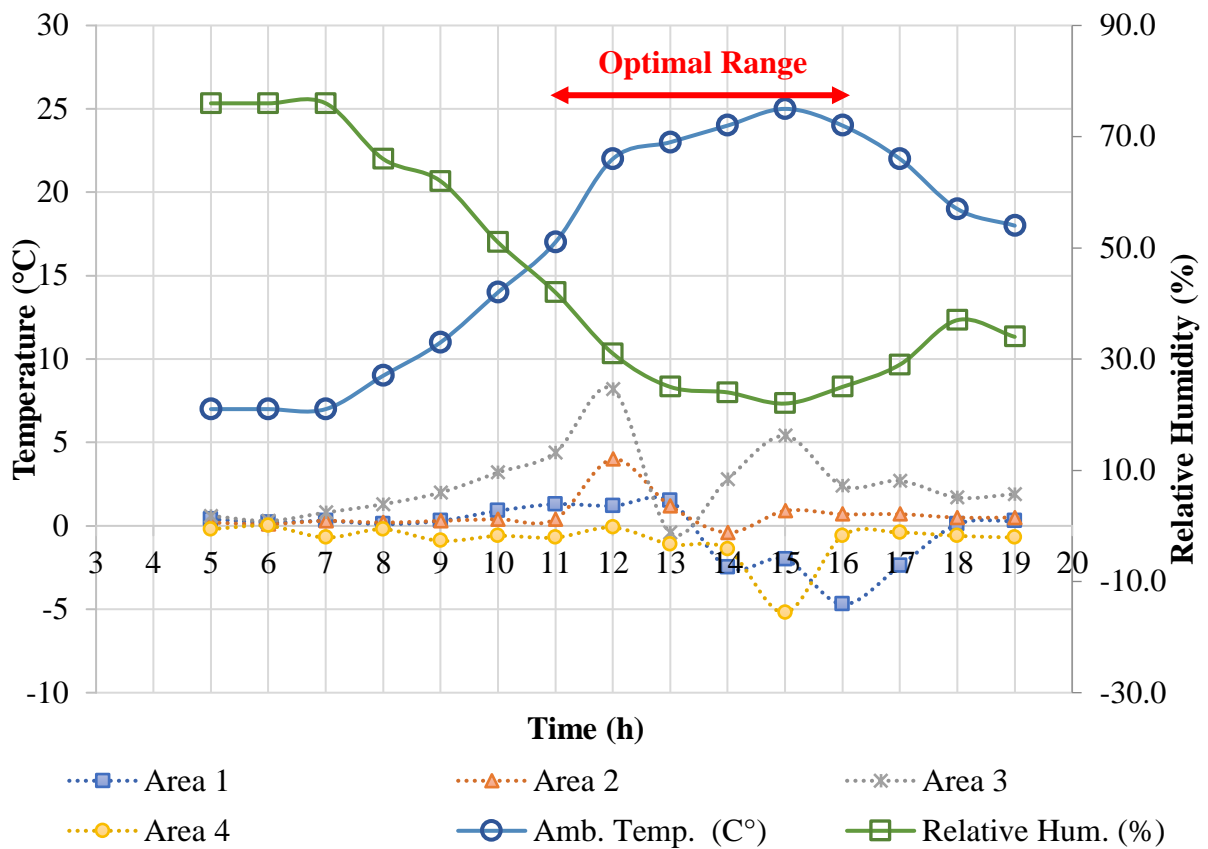
Figure 9. Temperature gradient in all four study areas.

5. CONCLUSIONS

Implementing infrared thermography to detect damage in flexible pavement generate positive results. This test may be considered as a preliminary non-destructive inspection method since it can analyze large areas in small intervals of time. However, these periods are limited during afternoon hours. The optimal range found for inspection was from 11:00 a.m. to 16:00 p.m.

This technique may detect invisible anomalies, showing an impacted section, but not the type or extent of damage. This aspect requires a detailed inspection where other studies and tests may accurately determine the type and nature of damage reflected by colorimetry in a thermogram.

This technique shows low thermal gradients on cloudy days as opposed to sunny days including high temperatures. Sudden temperature changes during monitoring activities reveal discontinuous data that are detrimental to analysis of damage behavior in flexible pavement, most of all regarding preliminary inspections. Implementing active infrared thermography and other non-destructive tests may reduce these uncertainties and generate more objective results.

6. REFERENCES

ABC – Administradora Boliviana de Carreteras (2011), *"Manual de diseño de conservación vial"*. ABC, La Paz, Bolivia, p. 365. Last access on May 30, 2019. Available at: http://www.abc.gob.bo/wp-content/uploads/2018/09/manual_de_diseno_de_conservacion_vial_abc.pdf

Bagavathiappan, S., Lahiri, B., Saravanan, T., Philip, J. (2013), *Infrared thermography for*

condition monitoring - A review. Infrared Physics & Technology. 60(1):35-55. Doi: https://doi.org/10.1016/j.infrared.2013.03.006

Bolivia (2006a), *Ley N°3507*, 27 de octubre de 2006. Último acceso 30 de mayo de 2019. Disponible en: http://www.abc.gob.bo/wp-content/uploads/2018/07/Ley_3507.pdf

Bolivia (2006b), *Decreto Supremo N°28946*, 25 de noviembre de 2006. Last access on May 30, 2019. Available at: http://www.abc.gob.bo/wp-content/uploads/2018/07/Decreto_Supremo_N%C2%BA_28946.pdf

Cengel, Y. (2003), *"Heat Transfer, a practical approach"*. McGraw-Hill, Segunda Edición, p. 932.

Farrag, S., Yehia, S., Qaddoumi, N. (2016). *Investigation of Mix-Variation Effect on Defect-Detection Ability Using Infrared Thermography as a Nondestructive Evaluation Technique*. Journal of Bridge Engineering, 21(3):1-15. Doi: https://doi.org/10.1061/(ASCE)BE.1943-5592.0000779

Fernandes, F. M., Pais, J. C. (2017), *Laboratory observation of cracks in road pavements with GPR*. Construction and Building Materials, 154:1130-1138. Doi: https://doi.org/10.1016/j.conbuildmat.2017.08.022

FLIR (2016), *"Smartphone S60 de Cat® Manual del usuario"*. Last access on May 28, 2019. Available at: https://www.catphones.com/download/User-Manuals/S60-Smartphone/S60-Manual-del-usario-Espa%C3%B1ol.pdf

Garrido, I., Lagüela, S., Arias, P. (2018), Infrared Thermography's Application to Infrastructure Inspections. *Infrastructures*, 3(3):1-19. Doi: https://doi.org/10.3390/infrastructures3030035

Golrokh, A. J., Lu, Y. (2019), *An experimental study of the effects of climate conditions on thermography and pavement assessment*. International Journal of Pavement Engineering, 1-12. Doi: https://doi.org/10.1080/10298436.2019.1656809

Janků, M., Cikrle, P., Grošek, J., Anton, O., Stryk, J. (2019), *Comparison of infrared thermography, ground-penetrating radar and ultrasonic pulse echo for detecting delaminations in concrete bridges*. Construction and Building Materials, 225:1098–1111. Doi: https://doi.org/10.1016/j.conbuildmat.2019.07.320

Khamzin, A. K., Varnavina, A. V., Torgashov, E. V., Anderson, N. L., Sneed, L. H. (2017), *Utilization of air-launched ground penetrating radar (GPR) for pavement condition assessment*. Construction and Building Materials, 141:130-139. Doi: https://doi.org/10.1016/j.conbuildmat.2017.02.105

Lin, S., Ashlock, J., Williams, R. C., Lee, H. D., Wang, Y. (2018), *Evaluation of three nondestructive testing techniques for quality assessment of asphalt pavements*. Nondestructive Testing and Evaluation, 33(4):361-375. Doi: https://doi.org/10.1080/10589759.2018.1484921

Los Tiempos (2016), *"Caos de tráfico vehicular en la ciudad de Cochabamba"*. Last access on May 30, 2019. Available at: http://www.lostiempos.com/actualidad/opinion/20161221/columna/caos-trafico-vehicular-ciudad-cochabamba

Los Tiempos (2016), *"Población protesta por el mal estado de las calles en Cochabamba"*. Last access on June 25, 2019. Available at: https://www.lostiempos.com/actualidad/local/20160420/poblacion-protesta-mal-estado-calles-cochabamba

Los Tiempos (2019), *"Cochabamba: ciudad de baches y eternas fallas en el asfalto"*. Último acceso 25 de junio de 2020. Disponible en: https://www.lostiempos.com/especial-multimedia/20190408/cochabamba-ciudad-baches-eternas-fallas-asfalto

Lovera, G. C. (2017), *"La política caminera del modelo de capitalismo de Estado de 1952 – 1985"*, Tesis de licenciatura, Universidad Mayor de San Andrés, p. 126.

Muñoz-Potosi, A., Pencue-Fierro, L., León-Téllez, J. (2009), *Análisis Termográfico Para La Determinación De Puntos Críticos En Equipos Mecánicos Y Eléctricos*. Bistua: Revista de la Facultad de Ciencias Básicas, 7(1):1-4. Available at: http://www.redalyc.org/articulo.oa?id=90312171013

Opinión (2018), *Alcaldía inicia reparación de baches en las calles*. Último acceso 25 de junio de 2020. Disponible en: https://www.opinion.com.bo/articulo/cochabamba/alcald-iacute-inicia-reparaci-oacute-n-baches-calles/20180220000500605048.html

Rehman, S., Ibrahim, Z., Memon, S. A., Jameel, M. (2016), *Nondestructive test methods for concrete bridges: A review*. Construction and Building Materials. 107(15):58-86. Doi: https://doi.org/10.1016/j.conbuildmat.2015.12.011

Revillas, S. (2011), *"Guía de la termografía infrarroja, aplicaciones en ahorro y eficiencia energética"*. eBuilding, Madrid, España, p. 189. Available at: https://www.fenercom.com/pdf/publicaciones/Guia-de-la-Termografia-Infrarroja-fenercom-2011.pdf

Rocha, J., Póvoas, Y. (2017), *Infrared thermography as a non-destructive test for the inspection of reinforced concrete bridges: A review of the state of the art*. Revista ALCONPAT, 7(3):200-214. Doi: https://dx.doi.org/10.21041/ra.v7i3.223

Rocha, J., Póvoas, Y., Silva, M., Monteiro, E. (2017), *Análise da Profundidade de Fissuras em Concreto com Termografia Infravermelha*. Revista de Engenharia e Pesquisa Aplicada, 2(3): 58-65. Doi: https://doi.org/10.25286/repa.v2i3.688

Solla, M., Lagüela, S., González-Jorge, H., Arias, P. (2014), *Approach to identify cracking in asphalt pavement using GPR and infrared thermographic methods: Preliminary findings*. Ndt & E International, 62:55-65. Doi: https://doi.org/10.1016/j.ndteint.2013.11.006

Tosti, F., Ciampoli, L. B., D'Amico, F., Alani, A. M., Benedetto, A. (2018), *An experimental-based model for the assessment of the mechanical properties of road pavements using ground-penetrating radar*. Construction and Building Materials, 165: 966-974. Doi: https://doi.org/10.1016/j.conbuildmat.2018.01.179

Vyas, V., Patil, V. J., Singh, A. P., Srivastava, A. (2019), *Application of infrared thermography for debonding detection in asphalt pavements*. Journal of Civil Structural Health Monitoring, 9:325-337. Doi: https://doi.org/10.1007/s13349-019-00337-8

Washer, G., Fenwick, R., Bolleni, N. (2010), *Effects of Solar Loading on Infrared Imaging of Subsurface Features in Concrete*. Journal of Bridge Engineering, 15(4): 384-390. Doi: https://doi.org/10.1061/(ASCE)BE.1943-5592.0000117

Critical analysis and innovation proposals to the heat and thermal shock test method of the Brazilian Standard NBR 15575 (2013)

L. S. Lorenzi[1] * , K. J. Stein[1] , L. C. P. Silva Filho[1]

*Contact author: luciani.lorenzi@ufrgs.br

ABSTRACT

The tests of Brazilian Standard NBR 15575: 2013 are part of the knowledge of the civil construction industry, but the heat and thermal shock test is innovative and does not have a consolidated history. The research objective is to analyze the testing critically and present proposals based on data meta-analysis. Results showed that the test is very inaccurate in describing the procedure and equipment. This study proposed adjustments and innovations in the test to provide more reliable results, but it does not make propositions regarding visual inspection and the number of cycles. The study concluded that the lack of information on the testing has direct responsibility for the results and that the suggested proposals have the potential to be incorporated.

Keywords: heat action and thermal shock; durability; evaluation of building performance.

_____

[1] Civil Engineering Department, School of Civil Engineering, Federal University of Rio Grande do Sul (UFRGS), Porto Alegre, Brazil.

Análise crítica e proposições de inovação ao método de ensaio de ação de calor e choque térmico à luz da ABNT NBR 15575 (2013).

RESUMO

Os ensaios da ABNT NBR 15575:2013 fazem parte do conhecimento do setor da construção civil, mas o ensaio de ação de calor e choque térmico é inovador e não possui um histórico consolidado. O objetivo da pesquisa é analisar o ensaio criticamente e apresentar proposições. O método de pesquisa é a meta-análise de dados. Os resultados demonstraram que o ensaio é bastante impreciso na descrição do procedimento e do equipamento. Foram propostos ajustes e inovações no ensaio para proporcionar resultados mais fidedignos, porém não foram realizadas proposições quanto à inspeção visual e aos números de ciclos. Conclui-se que a falta de informação do ensaio tem responsabilidade direta nos resultados e que as proposições sugeridas têm potencial para serem incorporadas.
Palavras-chave: ação de calor e choque térmico; durabilidade; avaliação de desempenho de edificação.

Análisis crítico y propuestas de innovación al método de ensayo de acción de calor y choque térmico a luz de la ABNT NBR 15575 (2013)

RESUMEN

Los ensayos de la ABNT NBR 15575:2013 hacen parte del conocimiento del sector de la construcción civil, pero el ensayo de acción de calor y choque térmico es innovador, y no posee un histórico consolidado. El objetivo de la pesquisa es analizar el ensayo críticamente y presentar propuestas. El método de pesquisa es meta-análisis de datos. Los resultados demostraron que el ensayo es bastante impreciso en la descripción del procedimiento y equipos. Fueron propuestos ajustes e innovaciones al ensayo para proporcionar resultados más fidedignos, sin embargo, no fueron realizadas propuestas en cuanto a la inspección visual y a los números de ciclos. Se concluye que la falta de información del ensayo tiene responsabilidad directa en los resultados y que las propuestas sugeridas tienen potencial para ser incorporadas.
Palabras clave: acción de calor y choque térmico; durabilidad; evaluación de desempeño de edificación.

Critical analysis and innovation proposals to the heat and thermal shock test method of the Brazilian Standard NBR 15575 (2013)

Lorenzi, L. S., Stein, K. J., Silva Filho, L. C. P.

1. INTRODUCTION

The Brazilian civil construction industry is in a period of great transformation in the technological area. The increase in the use of new materials, especially in residential buildings, and ABNT NBR 15575 (2013), henceforth NBR 15575, are promoting positive and significant changes in the sector. There is an increase in the interest of the civil construction market in knowing the behavior of the construction systems of buildings in use. This period provides a demand for testing and analysis of results. It also reflects an increase in the laboratory demand for services and technical assessment institutions, as well as the involved standard analysis.

Standards are not absolute nor perfect, so they need updates to keep up with the speed of technological changes (Borges, 2012). The evaluation methods and parameters established in standards, mainly in NBR 15575, must be adjusted over time (Thomaz, 2012 and 2013). Due to the little national experience in experimental performance tests to characterize the behavior of construction systems, the methods from countries with more experience in this type of research served as a basis for the Brazilian standard. It is noteworthy that, although the method is adequate, the conditions of these countries are different from the Brazilian reality, in which there is a lack of infrastructure for conducting tests. This fact was already alerted by Mitidieri Filho (1998) when he explained that methodologies for performance evaluation were brought from experiences by developed countries, where conditions are very different, giving rise to strict criteria for the existing reality. Another factor that the author draws attention to is related to the tests and parameters established in Brazil in the 1980s, aimed at building systems with conventional technology, excluding, to a certain extent, innovative building systems.

 The use of conventional systems as a reference and by comparison to judge innovative systems is usual; however, it is not a correct practice (Mitidieri Filho, 2007). NBR 15575 has some parameters that may be dissociated from the Brazilian reality, and so adjustments to the standard are necessary. Nevertheless, it is essential to start implementing the standard, even if limiting parameters below the international minimums are used (Thomaz, 2013).

The lack of a significant volume of tests and studies on the representability of parameters as to the results obtained, the correlations between test procedures, and expected ranges of results are factors that call into question the tests and parameters established in NBR 15575. Brazil does not have enough tests to characterize construction systems, whether they are innovative or not. In this context, several institutions have developed or adapted test procedures for performance evaluation, specifically the Institute for Technological Research (IPT) and some university laboratories. This attitude is encouraged by Thomaz (2013) and Villas Boas (2013) when they express that there is much to be improved in the requirements, criteria, evaluation methods, and parameters established in NBR 15575 since many construction systems are not contemplated by the standard yet.

A critical analysis of the tests to assess the performance of buildings, based on NBR 15575, concluded tests in the area of safety regarding structural performance have a consistent history but still need improvement. The other performance tests regarding safety, fire performance, and use and operation are in a maturation phase, in which they are beginning to have the deserved prominence. Habitability tests, acoustic performance tests, and water tightness tests are carried out more often and provide valuable information about building performance. As for the other building performance tests recommended in NBR 15575, there is no significant history that stands out, mainly when used to evaluate the elements that make up the construction systems. Among these tests, the heat and thermal shock test is considered new and, therefore, has no consolidated history (Lorenzi, 2013).

Intending to take advantage of the experience related to building performance tests, accumulated over the years by LEME / UFRGS (Laboratory of Testing and Structural Models at the Federal University of Rio Grande do Sul), this work carried out an evaluation of the procedure and the

Critical analysis and innovation proposals to the heat and thermal shock test method
of the Brazilian Standard NBR 15575 (2013)
Lorenzi, L. S., Stein, K. J., Silva Filho, L. C. P.

parameters of the heat and thermal shock test for external vertical sealing systems (EVSS).

The intention was to identify possible adjustments and innovations that could be applied to the testing, incorporating advances in procedures and allowing more accurate results regarding the behavior in the use of buildings. The adjustment of some acceptability parameters also provided a more coherent and fair assessment of the systems.

So, the main objective of this work was to perform a critical analysis of the heat action and thermal shock test, established and recommended in NBR 15575 for EVSS to evaluate the behavior regarding durability during the useful life and to present advancement proposals procedure and acceptability parameters.

2. BUILDING PERFORMANCE ASSESSMENT

A set of different instruments, such as theoretical analyses, simulations, experimental tests, and technical inspections, is the basis for the performance evaluation proposal of NBR 15575. Each of them contributes some way to assess whether the testing meets the requirements established for each performance criterion.

The culture change in the civil construction chain in using evaluation methods, more precisely tests to characterize the behavior of construction systems, can occur at two different times: the first concerns the use of tests in buildings ready to solve conflict situations between developer/builder and user. The second refers to the tests performed to characterize the behavior of the construction systems in use that are or will be applied in buildings (Borges, 2008). The European experience in the area indicates the culture related to the concept of building performance increases the carrying out tests, and this scenario is projected for Brazil in the coming years, increasing the demand for this type of testing. However, there may be significant delays in this scenario due to the limited laboratory capacity installed in the country (Lorenzi, 2013).

The performance assessment of a construction system aims to identify if the building production can use these systems and if they are capable of meeting performance requirements. This evaluation is only possible when working with a multidisciplinary team, experienced in the area, and if the structure to carry out this assessment is available. These conditions make possible to adjust or create new performance standards for construction systems, if necessary (Becker, 2001).

The standardized methods and procedures that allow reproducibility and verification regarding the fulfillment of building performance requirements should also be highlighted. This step is very relevant when it comes to analyzing the feasibility of using a construction system (Mitidieri Filho, 2007).

Brazil is in the expectation phase regarding the evolution and improvement of the tests recommended in NBR 15575, and to assist in this task, it is necessary to carry out critical analyzes on their practice, identifying gaps, and promoting adjustments that allow advances in testing methods and procedures. The moment is for consolidating practices and discussing methods and procedures to assess building performance, with attention to tests and acceptability parameters.

2.1 Heat and thermal shock test

The heat and thermal shock test to assess the durability requirement is presented in NBR 15575-4, internal and external vertical sealing systems (IEVSS) for residential buildings. The purpose of this test is to analyze the behavior of the EVSS when subjected to successive cycles of heating by heat source and cooling by water jets. The idea is to simulate the stress that buildings suffer during their useful life through the variation in temperature and humidity associated with the action of rain on the heated element (wall). The heat and thermal shock test is one of the accelerated aging tests used to assess the potential behavior of the EVSS in use. The test promotes an increase in the frequency of the occurrence of agents that induce deterioration. In this case, the deteriorating agent is the

Critical analysis and innovation proposals to the heat and thermal shock test
method of the Brazilian Standard NBR 15575 (2013)
Lorenzi, L. S., Stein, K. J., Silva Filho, L. C. P.
367

abrupt change in temperature on the surface of the element, when subjected to thermal shock. This situation occurs when, for example, the building's façade is hit by rain suddenly, after a day of much sunlight (Fontenelle, 2012).

A notorious aspect of the study of façade durability is its behavior when facing sudden heating and cooling cycles. The temperature difference between the surface and its interior can cause stresses of high magnitude, deteriorating facade system, in particular, light systems (with little thermal inertia) and those composed of several layers with non-homogeneous elements (Oliveira et al., 2014). When the temperature variation is sudden, the load rate on the element is high. However, the propagation of thermal deformations on the same element depends on its response speed until it reaches balance (Esquivel, 2009).

The heat and thermal shock test established in NBR 15575-4 consists of applying ten successive heating and cooling cycles for each specimen representative of the EVSS. The surface exposed to the heat must remain at temperatures between 80 ± 3 ° C, for one hour. After this period, water is sprayed on the heated surface until it reaches temperatures in the range of 20 ± 5 ° C. The test procedure requires a specimen with a variable extension (width) between 1 meter to 1.40 meters and the height of a wall. The specimen is placed on a fixing device by the lower and upper edge.

The recommendations of NBR 15575 regarding the performance evaluation of EVSS take into account the degradation caused by thermal shocks, such as cracks, failures, detachment, blistering, deterioration, among others, resulting from thermal expansion, retraction, and expansion. Also considered in this evaluation is the maximum horizontal displacement parameter (h /300), where h is the height of the element. A deflectometer is positioned on the opposite side in the center of the element to measure the horizontal displacement.

Among the national and international standards related to the thermal shock in EVSS, there are some divergences regarding categories and parameters. For example, the heating temperature for the exposed surface of the EVSS recommended by NBR 15575-4 differs from the ETAG 0004 (2008), which establishes a temperature of 70 ± 5 ° C and ISO 8336 (2009) and ASTM C1185-8 (2012) standards which establish a temperature of 60 ± 5 ° C. The measurement of surface temperatures is another divergent point. In the Brazilian standard (NBR 15575), the measurement is performed by thermocouples, which are coupled directly on the surface of the specimen. On the other hand, in the American standard (ASTM C1185-8), the thermocouples are not fixed directly on the specimen. They are attached to small metallic plates, painted in black, which are fixed on the surface of the specimen (Oliveira et al., 2014).

Table 1 summarizes the differences in parameters adopted in Brazilian standards and other testing methods concerning some of these aspects previously explained.

Table 1. Differences in parameters adopted among Brazilian standards and international testing methods.

Category	Parameters	Detalhamento dos parâmetros		
		NBR 15575-4 (ABNT, 2013b)	C1185-8 (ASTM, 2012) and ISO 8336 (ISO, 2009)	ETAG 004 (ETAG, 2008)
Heating	Test temperature measurement method	Direct measurement, using thermocouples positioned on the heated specimen surface	Indirect measurement, measured on the reference specimen/black metal plate	Direct measurement, using thermocouples positioned on the heated specimen surface

	Time to reach maximum heating temperature	Not established	Not established	1 h
	Maximum test temperature	80 ± 3 ° C	60 ± 5 °C	70 ± 5 °C
	Dwell time in the heated phase	1 h	2 h 55 min	2 h
	Admitted temperature variation between center and specimen edges	± 3 °C	Not established	Not established
Cooling	Water temperature	Until reaching the surface temperature of 20 ± 5 ° C	≤ 30 °C	15 ± 5 °C
	Amount of water	Not established	3.79 l/min	≥ 1.0 l / m² min, which is equivalent to approximately 6.0 l / min
	Sprinkling time	Until reaching the surface temperature of 20 ± 5 ° C	2 h 55 min	1 h
	Distribution over the surface	Uniform	Uniform	Uniform
	Temperature after specimen cooling	20 ± 5 °C	Not established	Not established
Cycles	Time of each cycle	Approximately 6 h, depending on the composition of the wall	6 h	6 h
	Number of cycles	10	25	80
	Interval between cycles	Not established	5 min	2 h
Specimen	Dimension	≥ 3.0 m² (1.2 m x 2.5 m)	≥ 3.5 m²	≥ 6.0 m²
	Restriction of edge movement	No restriction	Restricted	No restriction
	Surface color	Not established	Not established	Not established

Source: Oliveira et.al. (2014)

The interpretive analysis of the building performance tests established in NBR 15575 carried out by Lorenzi (2013) originated a mapping containing tests x buildings x interpretive analysis criteria, serving as a basis to identify the tests to be critically analyzed, concerning the interpretation, procedures, equipment, and parameters. This mapping identified the test that needs to be improved is the heat and thermal shock test.

Critical analysis and innovation proposals to the heat and thermal shock test
method of the Brazilian Standard NBR 15575 (2013)
369
Lorenzi, L. S., Stein, K. J., Silva Filho, L. C. P.

Oliveira et al. (2014) also proposed improvements for the heat and thermal shock test. These changes should be applied to SVVE consisting of light elements ($\leq$ 60kg / m²), considering new parameters, procedures, or conditions for carrying out the test. Table 2 presents a summary of the advanced proposals for the heat and thermal shock test.

Table 2. Advanced proposals for the heat and thermal shock test.

Category	Lorenzi (2013)	(Oliveira et.al., 2014)
Heating	-	80 ± 3 ºC EVSS in a usual situation 60 ± 3 ºC EVSS in a particular situation
	Variable time according to EVSS composition	At least 1 hour for the EVSS to reach the maximum temperature
	-	Heating exposure increased from 1 h to 2 h
	The heat must warm the entire surface of the specimen	Identify distortions between the center and the edges of the specimen
	The specimen must have a homogeneous temperature	W / m² control
Cooling	Keep the water cooled to the temperature of 20 ± 5 ºC	Control the temperature of the cooling water
	Cooling time, sprinkling, and speed with which the temperature variation occurs	Cooling time, sprinkling, and speed with which the temperature variation occurs.
	Cooling water at a constant temperature	The temperature control method according to the standardized temperature
	Constant and uniform water sprinkling on the specimen, controlling the water pressure	Surface distribution
	Reuse of the water	-
Cycles	Successive cycles (no interval)	There must be an interval between cycles
Specimen	Minimum width 1.0 m to 1.40 m	Minimum width 2.40 m
	Height 2.50 m	Height 2.50 m
	All the details of the EVSS	All the details of the EVSS
	Side constraint	Side joining
	Supported on the bottom and restricted on the top	Supported at the bottom and articulated at the top
	-	External face color: absorbance $\geq$ 0.5 to reach 80 ºC faster
Radiant panel and water spray equipment	Electrical resistance radiation	Electrical resistance radiation and ultraviolet lamps
	The radiant panel area should be the same as the specimen area	-
	Possibility of inspection at each cycle	-

Critical analysis and innovation proposals to the heat and thermal shock test method of the Brazilian Standard NBR 15575 (2013)

370

Lorenzi, L. S., Stein, K. J., Silva Filho, L. C. P.

Horizontal displacement parameter	Decrease the limit for horizontal displacement by 50%	-
	Add the residual horizontal displacement	-
Rainwater tightness test	Before and after the heat and thermal shock test	Before and after the heat and thermal shock test

The fixation of the specimen during the test is one of the relevant points to be incorporated into the testing. The containment of the specimen must restrict the expansion or contraction of it in the length direction, allowing free vertical movement and transverse displacement, and offering no restriction on the formation of the arrow due to the temperature gradient in the wall section. These considerations should be applied by systems that present significant displacements due to dimensional variations, caused by the effect of temperature and humidity. In cases such as these, Fontenelle and Meditidieri Filho (2016) indicated the contention of the specimen.
The heat and thermal shock test does not present a single result for all construction systems. Its boundary conditions control the element's response to thermal shock. That is why the external restrictions on the free deformation of the specimen can aggravate the stress state. If the exposure to the heat flow is symmetrical over the entire surface of the specimen, the heat transfer will occur until it reaches thermal equilibrium, in other words, the temperature will be the same throughout the solid (Esquivel, 2009).

3. METODOLOGY

The experimental strategy was carried out based on the advance propositions recommended by Lorenzi (2013). Altogether, the study subjected the samples to a total of 280 cycles. Ten out of 12 specimens were exposed to 220 thermal cycles. On the other two, only 60 thermal cycles were applied. The strategy focused on critically analyze the advancement proposals to improve the test results.
The advancement propositions incorporated were:
- Heating time according to the construction system;
- The water used during the test should be kept in a reservoir at 15 to 25ºC;
- Cooling time according to the construction system;
- Cooling water always in the temperature range between 15 to 25ºC;
- Uniform and constant water spray (3 l/m²/min), the water spray pressure should have no interference in the construction system;
- Reuse of test water;
- Successive cycles, no interval;
- Visual inspection at each cycle;
- Width of the specimen 1.20 m;
- Height of the specimen 2.50 m;
- Radiation by electrical resistances;
- Execution of the rainwater tightness test before and after the thermal shock test.

The following criteria was the basis for the analysis of the propositions:
- **Applicability**: This criterion concerns the applicability of the test in terms of the minimum dimensions and position of the specimen and its instrumentation;
- **Feasibility**: This criterion concerns the execution of the test and the possibility of reproducing the proposals;

- **Reliability and representability of the results**: This criterion has the precept to recognize that the propositions reproduce in the best way the real situation to which the systems are subject;
- **Suitability**: This criterion is associated with the suitability of the test method to the different construction systems.

4. RESULTS

The results are presented in Table 3, which shows how each advanced proposal for the heat and thermal shock test was incorporated into it, thus reaching expectations.

Table 3. Results of the incorporation of the proposals to improve the heat and thermal shock test.

Category	Proposals	Applicability	Feasibility	Reliability and representability of the results	Suitability
Heating	Heating time according to the construction system	OK	OK	1*	1*
Cooling	Keep the temperature of the water stored in the reservoir between 10 to 20ºC	OK	OK	OK	OK
	Cooling time according to the construction system	OK	OK	2*	2*
	Keep the temperature of the cooling water between 10 to 20ºC	OK	OK	OK	OK
	Uniform water spray (3 l/m²/min) Constant and with pressure without interference in the construction system	OK	OK	OK	OK
	Reuse of the water	OK	OK	OK	OK
Cycles	Successive cycles (no interval)	OK	OK	OK	OK
	Visual inspection at each cycle	3*	3*	3*	3*
Specimen	Specimen width 1.20 m	OK	OK	OK	OK
	Specimen height 2.50 m	OK	OK	OK	OK
Equipment	Electrical resistance radiation	OK	OK	OK	OK
Tightness	Application of the rainwater tightness test before and after the thermal shock test	OK	OK	OK	OK

1*, 2*, and 3* - New advances propositions to the test.

Based on the accumulated experience in the application of the heat and thermal shock test carried out with radiant panel equipment, this study observed that the hot air convection printed very high temperatures at the top of the sealing system.
The air convection helped to homogenize the temperatures in the specimen, spreading the radiation that was only at the bottom, as shown in Figure 1.

Critical analysis and innovation proposals to the heat and thermal shock test method of the Brazilian Standard NBR 15575 (2013)
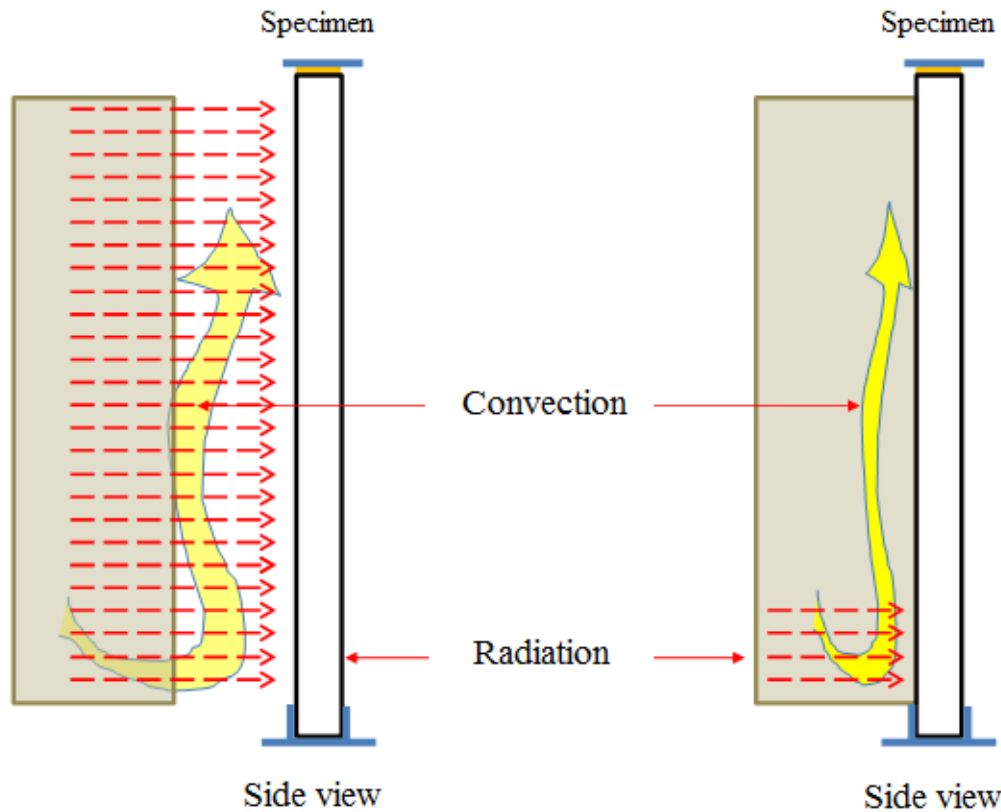Lorenzi, L. S., Stein, K. J., Silva Filho, L. C. P.

Figure 1. Examples of radiation and convection for heat and thermal shock test in EVSS.

The study observed that depending on the different compositions of the EVSS and the thickness of the specimen, heating and cooling present different behaviors to reach both the surface temperature (80 $\pm$ 3 ° C) and the temperature of the thermal shock (25 $\pm$ 5 ° C), requiring adjustment of the heat source. The water sprays were standardized by this study to provide a simulation of heavy and constant rain. They had a pressure that did not influence the horizontal displacement of the specimen.

The water used was maintained in a temperature range between 10 to 20° C. The controlled water temperature allowed the sprays to have the same temperature range when reaching the heated surface. These sprays reduced the temperature of specimens to 20 $\pm$ 5 ° C.

The reuse of the water during the test was important for water conservation. Each test consisted of 10 heating and cooling cycles, with an estimated consumption of 300 liters of water/cycle/specimen, the vertical system was 1.20 $\pm$ 0.20m wide by 2.50m high, totaling consumption of 3,000 liters of water per test. Figure 2 shows the water flow diagram for cooling the specimen, using a booster pump and filter, used to prevent clogging of the water spray nozzles.

Critical analysis and innovation proposals to the heat and thermal shock test method of the Brazilian Standard NBR 15575 (2013)

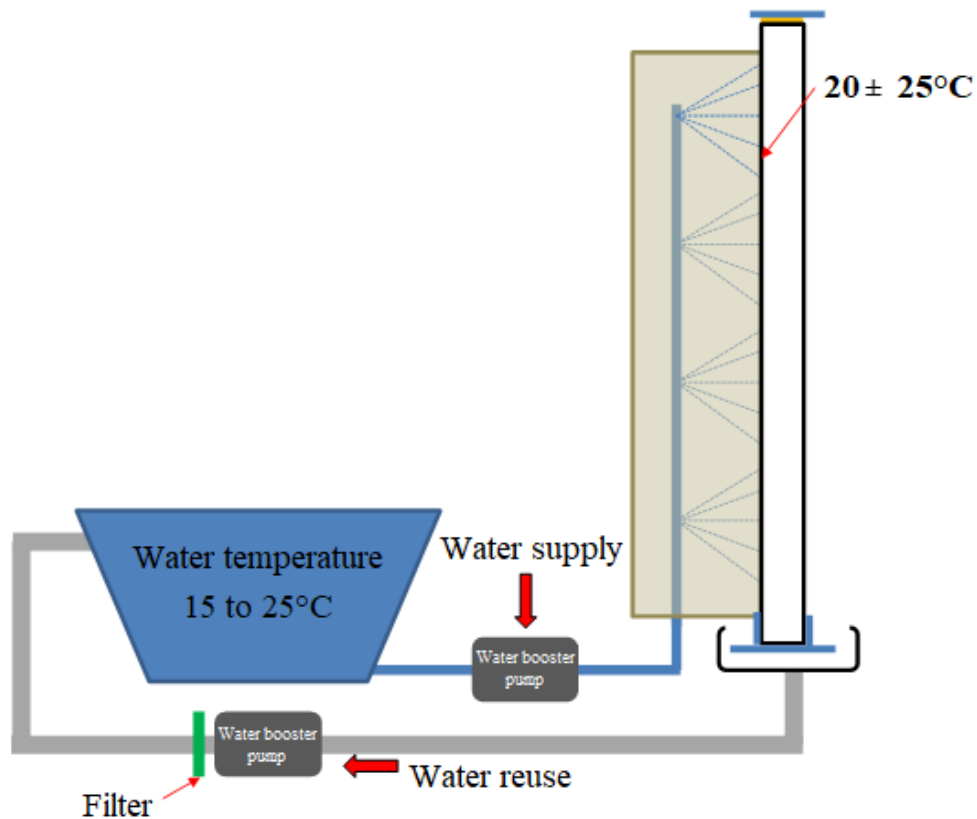Lorenzi, L. S., Stein, K. J., Silva Filho, L. C. P.

373

Figure 2. Schematic drawing of water reuse; schematic drawing of the confinement of the specimen with the aid of a support frame and the fixation of the deflectometer support for testing the action of heat and thermal shock in SVVE.

Visual inspection is not always sufficient for an accurate assessment of the degradation suffered by the specimen. All of the rainwater tightness tests happened before and after the heat and thermal shock tests. The second rainwater tightness test was performed again after ten thermal cycles. This test followed the established in NBR 15575-4 (2013).

This study identified the need for adjustments and innovations in the procedure that promote the reproducibility of the exposure conditions, to allow and provide more reliable results with the real behavior in the use of the systems. Table 4 presents new proposals for the heat and thermal shock test.

Table 4. New advances in the heat and thermal shock test.

Testing	New Proposals
Specimen	Restrict the upper part to represent the building system in use
Heating	The heating time between 15 - 20 min for the light and flexible EVSS
	The heating time between 35 - 40 min for the heavy and rigid EVSS
Water cooling	3min cooling time for light and flexible EVSS
	6min cooling time for heavy and rigid EVSS
	Keep the temperature of the water between 10 to 20ºC
Cycles	Apply successive cycles
Radiant panel and water spray equipment	Electrical resistance radiation and ultraviolet lamps

Critical analysis and innovation proposals to the heat and thermal shock test method of the Brazilian Standard NBR 15575 (2013)

Lorenzi, L. S., Stein, K. J., Silva Filho, L. C. P.

5. CONCLUSIONS

The consolidation of the performance concept, the establishment of clear, objective, and well-defined requirements, and the incorporation of tests to understand the potential performance of systems are examples of a revolution in the construction industry, which directly impacts the design of buildings. Building performance tests are fast, accurate, and reliable means of predicting the potential behavior in the use of EVSS and are relevant for the assessment of building performance. The results obtained by the testing improved the understanding of what to expect as a result of the behavior of construction systems in use, innovative or not, subjected to environmental temperatures and sudden temperature cooling. As expected, the lack of a consolidated history of use and result dissemination prejudices the description of the test procedure and the details of the equipment.
This study did not make any proposal regarding the visual inspection and the number of cycles to which a specimen is subjected when tested, there is a need for criteria, parameters, and limits, to achieve a better assessment and avoid the subjectivity of the visual inspection. About the advances in the method of testing heat action and thermal shock, it was possible to prove that they are relevant and contribute significantly to a better estimate of behavior in the use of EVSS, innovative or not. Thus, the study concluded that the presented proposals have the potential to be incorporated into the procedure of the heat and thermal shock test, promoting a result closer to the real situation.

6. ACKNOWLEDGMENTS

7. REFERENCES

ASTM International. (2012). *ASTM C 1185-8 Standard test methods for sampling and testing non-asbestos fiber-cement flat sheet, roofing and siding shingles, and clapboards.* https://doi.org/10.1520/C1185-99
Associação Brasileira De Normas Técnicas. (2013). *NBR 15575: Edifícios Habitacionais – Desempenho – Parte 1: Requisitos Gerais.* Rio de Janeiro.
Associação Brasileira De Normas Técnicas. (2013). *NBR 15575: edifícios habitacionais – desempenho – parte 2: requisitos para os sistemas de estruturais.* Rio de Janeiro.
Associação Brasileira De Normas Técnicas. (2013). *NBR 15575: edifícios habitacionais – desempenho – parte 4: requisitos para os sistemas de vedação verticais Internas e Externas – SVVIE.* Rio de Janeiro.
Becker, R. (2001), *An Integrated Approach to the Development of Performance Test Methods and their Application to Evaluation and Design.* The RILEM Journal Materials and Structures. 34:467 – 474.
Borges, C. A. (2012), *Desempenho Revisado.* Revista Téchne, 192:42 – 49.
Borges, C. A. M. (2008), "*O conceito de desempenho de edificações e a sua importância para o setor da construção civil no Brasil*", Masters Thesis, Universidade de São Paulo. https://doi.org/10.11606/D.3.2008.tde-25092008-094741
Esquivel, J. F. T. (2009), *"Avaliação da Influência do Choque Térmico na Aderência dos Revestimentos de Argamassa",* Doctural Thesis, Universidade de São Paulo, p. 262.
European Organization for Technical Approvals. (2008) *ETAG 004: Guideline for European Technical Approval of External Thermal Insulation Composite Systems With Rendering.* Brussels.

Fontenelle, J. H. (2012), *"Sistema de fixação e juntas em vedações verticais constituídas por placas cimentícias: estado da arte, desenvolvimento de um sistema e avaliação experimental",* Masters Thesis, Universidade de São Paulo, p. 219.

Fontenelle, J. H. e Mitidieri Filho, C. V. (2016), "*Condições de contorno lateral dos corpos de prova submetidos ao ensaio de ação de calor e choque térmico*". In: XVI Encontro Nacional de Tecnologia do Ambiente Construído, São Paulo.

International Organization for Standardization (2009). ISO 8336: *Fibre-cement flat sheets.* Geneva.

Lorenzi, L. S. (2013), *"Análise Crítica e Proposições de Avanço nas Metodologias de Ensaios Experimentais de Desempenho à Luz da ABNT NBR 15575 (2013) para Edificações Habitacionais de Interesse Social Térreas",* Doctural Thesis, Universidade Federal do Rio Grande do Sul, p. 222.

Mitidieri Filho, C. V. (1998), *"Avaliação de desempenho de componentes e elementos construtivos inovadores destinados a habitações: proposições específicas à avaliação do desempenho estrutural"*, Doctural Thesis, Universidade de São Paulo.

Mitidieri Filho, C. V. (2007), Qualidade e Desempenho na Construção Civil. In: Isaia, G. C. "*Materiais de Construção Civil e os Princípios de Ciência e Engenharia dos Materiais"*, São Paulo, IBRACON, cap. 23, pp. 37 – 73.

Oliveira, L. A.; Fontenelle, J. H. e Mitidieri Filho, C. V. (2014), *Durabilidade de fachadas: método de ensaio para verificação da resistência à ação de calor e choque térmico.* Ambiente Construído. 14(4):53- 67. https://doi.org/10.1590/S1678-86212014000400005

Silva, M. A. C. (2001), *"Desafios da Aplicação Prática do Conceito de Desempenho e seu Impacto na Qualidade das construções".* In: 4º Seminário de Patologia das Construções, São Leopoldo.

Silva, M. A. C. (2013) "*Especificação por desempenho e os dados de caracterização de desempenho disponibilizados pelos fabricantes*". In: Seminário: Projeto, Especificações e Controle de Execução para Atender a Norma de Desempenho, São Paulo.

Thomaz, E. (2012) *"Tendências de Materiais, Tecnologias e Processos de Construção de Edifícios".* In: Seminário: Tecnologia, Desempenho e Sustentabilidade na Construção Civil, Manaus.

Thomaz, E. (2013) "*O que é preciso fazer para atender a norma quanto ao desempenho de pisos".* In: Seminário: Projeto, Especificações e Controle de Execução para Atender a Norma de Desempenho, São Paulo.

376

Critical analysis and innovation proposals to the heat and thermal shock test method
of the Brazilian Standard NBR 15575 (2013)
Lorenzi, L. S., Stein, K. J., Silva Filho, L. C. P.

The pathological manifestations and risks of the protectors of air conditioners in buildings

W. W. Silva[1]* ⓘD, E. C. B. Monteiro[1] ⓘD

*Contact author: wildsonws@gmail.com

DOI: https://doi.org/10.21041/ra.v10i3.410

ABSTRACT

Faced with the large number of partial or total collapses in buildings, the objective of this study is the identification of the pathological manifestations and the risks of the supports for air conditioners of reinforced concrete in the buildings. The data were collected by 3D software and consolidated in the field. Of the 61 buildings analyzed, 48% are of the window model which, in a situation of degradation and fall, can reach the ground with an impact of the order of tons. In coastal regions, we add the accelerating effects of the corrosion of the reinforcement, such as high humidity, pollution by automotive vehicles and marine region. It was concluded that these supports do not have adequate structural designs, allied to the low quality and accelerating effects of the reinforcement corrosion, rendering them not recoverable.

Keywords: pathology; corrosion; air conditioning; concrete; risks.

_____

[1] Universidade de Pernambuco, Recife, Brasil.

Responsible Associate Editor for this paper: Andrés Antonio Torres Acosta

Contribution of each author

In this paper, the author Wildson Wellington Silva contributed to the activity of drawing the manuscript, collecting data, analyzing and interpreting the data, critical review of the content and discussing the results, the author B contributed to the activity of drawing the manuscript, analysis and interpretation of data, critical review of content and discussion of results.

Discussions and subsequent corrections to the publication

Any dispute, including the replies of the authors, will be published in the second issue of 2021 provided that the information is received before the closing of the first issue of 2021.

As manifestações patológicas e os riscos dos protetores de aparelhos de ar condicionado em edificações

RESUMO

Diante do grande número de colapsos parciais ou totais em edificações, tem-se neste estudo a identificação das manifestações patológicas e os riscos dos suportes para aparelhos de ar condicionado de concreto armado nas edificações, os dados foram coletados por software 3D e consolidados em campo. Das 61 edificações analisadas, 48% são do modelo tipo janela, que em uma situação de degradação e queda, podem chegar ao solo com um impacto da ordem de toneladas. Em regiões litorâneas, somam-se os efeitos aceleradores da corrosão da armadura, como umidade elevada, poluição por veículos automotores e região marinha. Conclui-se que esses suportes não possuem projetos estruturais adequados, aliados a baixa qualidade e efeitos aceleradores da corrosão da armadura, tornando-os não passíveis de recuperação.
Palabras clave: patologia; corrosão; ar condicionado; concreto, riscos.

Las manifestaciones patológicas y los riesgos de los protectores de aparatos de aire acondicionado en edificaciones

RESUMEN

Ante el gran número de colapsos parciales o totales en edificaciones, el objetivo de este estudio es la identificación de las manifestaciones patológicas y los riesgos de los soportes para aparatos de aire acondicionado de hormigón armado en las edificaciones. Los datos fueron recolectados por software 3D y consolidados en campo. De las 61 edificaciones analizadas, 48% son del modelo tipo ventana que, en una situación de degradación y caída, pueden llegar al suelo con un impacto del orden de toneladas. En regiones costeras, se suman los efectos aceleradores de la corrosión de la armadura, como humedad elevada, contaminación por vehículos automotores y región marina. Se concluye que estos soportes no poseen proyectos estructurales adecuados, aliados a baja calidad y efectos aceleradores de la corrosión de la armadura, haciéndolos no posibles de recuperación.
Palabras clave: patología; corrosión; aire acondicionado; concreto, riesgos.

The pathological manifestations and risks of the protectors of air conditioners in buildings
Silva, W. W., Monteiro, E. C. B.

1. INTRODUCTION

Technological advances in air conditioners favored energy efficiency, associated with the improvement of technical standards for building design and construction and the constant need for lower energy consumption refrigeration systems (Larsena, et.al., 2015) and greater environmental awareness (Perinia, et.al., 2017).

There is currently a liability for cooling systems that have not proven efficient over the years, as they have been neglected as part of the final stages of construction, where the financial cash flow of construction companies no longer carry excessive expenses in this phase of delivery of buildings, therefore, adopting low quality materials, despite being exposed and external structures, as is the case of facades.

These supports can be of various models and materials, which can be reinforced concrete, very common in Brazil, metallic such as the USA (United States of America), United Kingdom and Spain, not being restricted only in places where there is adequate urban control, as in poor neighborhoods, in countries in Africa, Asia and Latin America (Desai and Potter, 2014), but in middle-class and even upscale neighborhoods, it can be concluded that it is part of a very large global scenario.

In building maintenance services, it is very common to change reinforced concrete supports, due to the deterioration of the structure of the support or to incidents that have already occurred in the common area of the building, which raises the need to study the subject. If the presence of pathological manifestations is so intense, added to the aggravation of these supports being in an outdoor environment and at high heights, what would be the impacts of these supports and / or equipment on the ground? What is the degree of risk to impacted people, vehicles and structures?

During the research phase of bibliographic references, it was not possible to identify similar studies on the support for air conditioning in buildings, which could serve as a basis for this work, which further broadened the interest in the subject, but all were used. the aspects inherent in pathological manifestations, environmental and climatic conditions, statistics and techniques.

Corrosion mechanisms are not simple or new, since the range of possibilities for their occurrence, according to (Johnson, 1965) there is an expansion effect on the concrete mass, causing cracks and consequent concrete fragmentation, corrosion is linked preponderantly to the electrochemical process, linked to the humid environment and being aggravated by the aggressive environment, variations in the thickness of the concrete cover, as commented by (Cánovas, 1984), design errors, as well as the adoption of inappropriate materials, are procedures that favor largely the appearance of pathological manifestations. In ABNT NBR 6118: 2014, it defines durability as the ability of the structure to withstand design requirements while retaining safety and stability over the life of its lifetime, a very important point, since even structures are not forever durable and need to be constantly reviewed and repaired.

According to ABNT NBR 6118: 2014, and in order to have a longer service life, it is necessary to comply with some guidelines to retard the mechanisms of concrete deterioration caused by leaching, sulphate expansion, alkali-aggregate reaction, deterioration of the reinforcement with respect to carbonation, chloride action, and the mechanisms of the structure itself For these conditioners, there is a relationship regarding the environmental aggressiveness classes (CAA), which were classified according to the region and microclimate conditions. According to (Bertolini, 2010) and (Almeida and Sales, 2018), there are some aspects related to atmosphere types and exposure and they were analyzed in three main parts: relative humidity critical air (over 65% and up to 85%); marine atmosphere, attack by chloride and sulfate ions (proximity to seawater); and larger population centers (aggressive agents). In addition, the influence of winds on a building was studied, taken one as an example, as some aspects inherent to the corrosion of reinforcement are influenced by the action of rain and wind.

This study aims to identify: the models of air conditioner brackets of the buildings surveyed; the types of pathological manifestations most commonly found, as well as accelerating factors; the risks they pose to people, cars and structures, in the situation of partial or total fall of the building and/or the air conditioner itself ; and whether there is a definite possibility of restoring them.

2. METHODOLOGY

This research is a Case Study, delimited in the city of Recife, capital of the state of Pernambuco, Brazil, with the geographical coordinates of latitude: -8.05428, longitude: -34.8813, which has a territorial area of 218.843 km² and population estimated at 1,637,834 people (IBGE, 2018), with a population density of 7,039.64 inhabitants per square kilometer and MHDI - Human Development Index of 0.772 (IBGE, 2010), GDP per capita of US$ 7,916.29 (IBGE, 2016), of tropical climate, hot and humid, with 3 dry months and average temperature above 18ºC in all months of the year (IBGE, 2002).

It was adopted the region of northern Recife, between the neighborhoods of Parnamirim, Tamarineira and Casa Amarela, according to dividing lines in yellow, defined a blue circle of radius = 300m green, using the Google Earth Pro computer program, Figure 1.
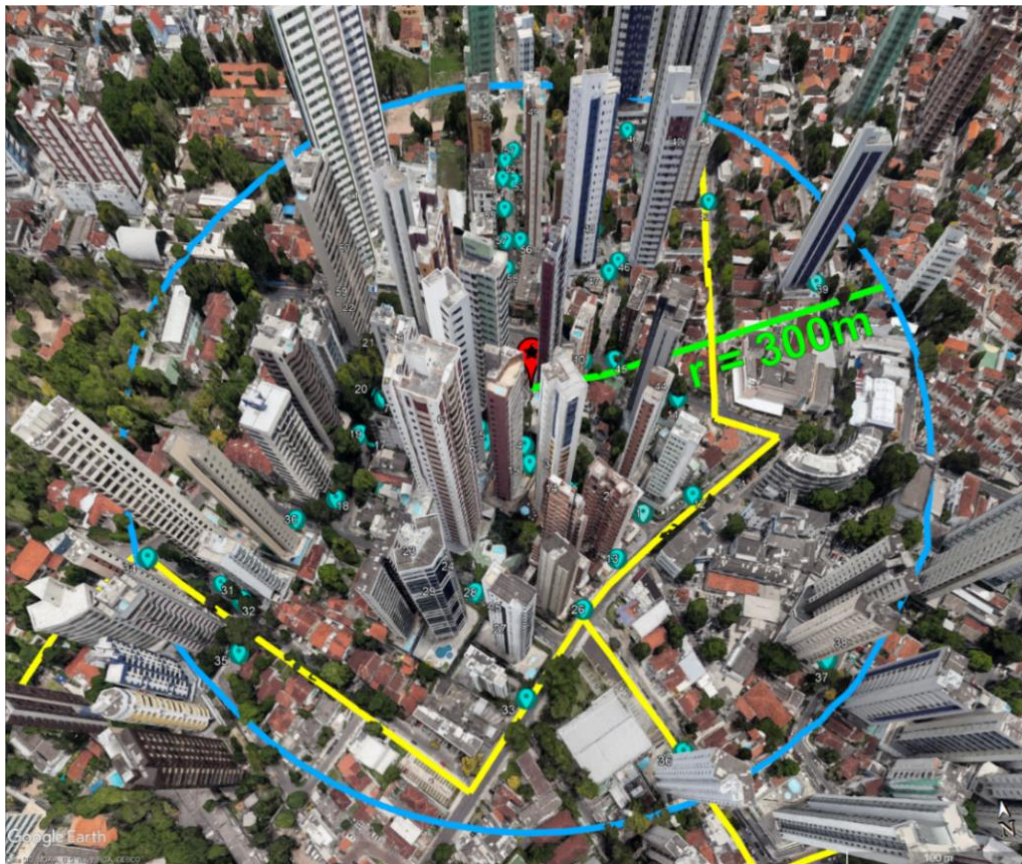

Figure 1. Location of the buildings researched.

An MS-Excel spreadsheet was initially created, with the information to be collected: building name and address, geographic coordinates, elevation between the base and top of the building, number of floors, estimated height, type of air support conditioning, condition of the supports (inspection), as the pathological manifestations (bad, regular and good) and the box model whether it is open or closed type and if they have already been replaced.

It was then defined to include only buildings above 3 floors, as low houses and buildings are more difficult to verify due to the high walls, not including public buildings, which were represented by dots and a blue numbering in order to be For easier cataloging of the information, these samples were collected over a period of 4 months by the computer and after this phase, a field visit was performed to verify some data not clarified during the first phase of collection and consequently to complete the worksheet. with the data of pathological manifestations identified and if after the construction of the building there were already replacements.

3. ANALYSIS OF THE BUILDINGS

3.1. Types of air conditioning brackets
After gathering information, it was possible to identify 3 types of support systems for refrigeration appliances, which are: reinforced concrete protective boxes (window type), others supported by windows or spans (adopted as a hidden model) and the use of structures already incorporated into the building (split model), thus reaching a total of 61 buildings analyzed, Figure 2.
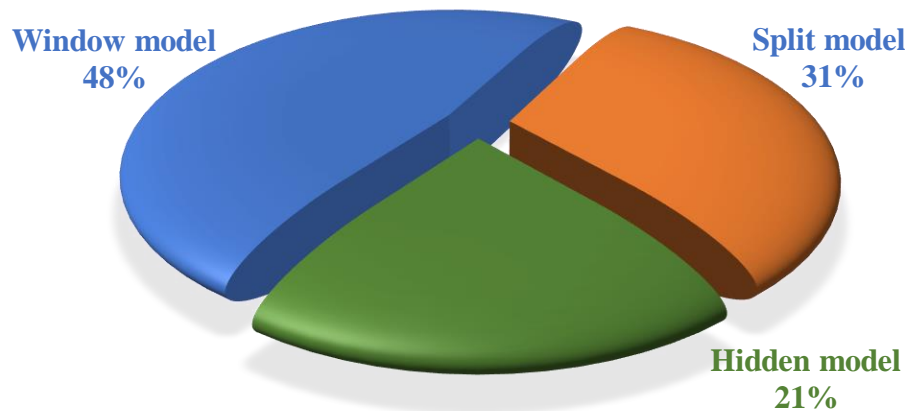

Figure 2. Building cooling system support systems.

Thus, it was found that 48% of buildings use window type models, 21% with the hidden model and finally, with only 31% the models that integrate the structures of buildings (split appliances), by the way come from latest projects.
What can be highlighted from the collected data is the existence of two models of window-type reinforced concrete protectors, out of a total of 29, 20 for the open model and 9 for the closed model, for their characteristics and dimensions, one can consider the most open model fragile, that is, almost 70% of the buildings that have window-type reinforced concrete protector have the simplest model and therefore generate a higher risk of premature wear. Below are the models represented in Figures 3 and 4.
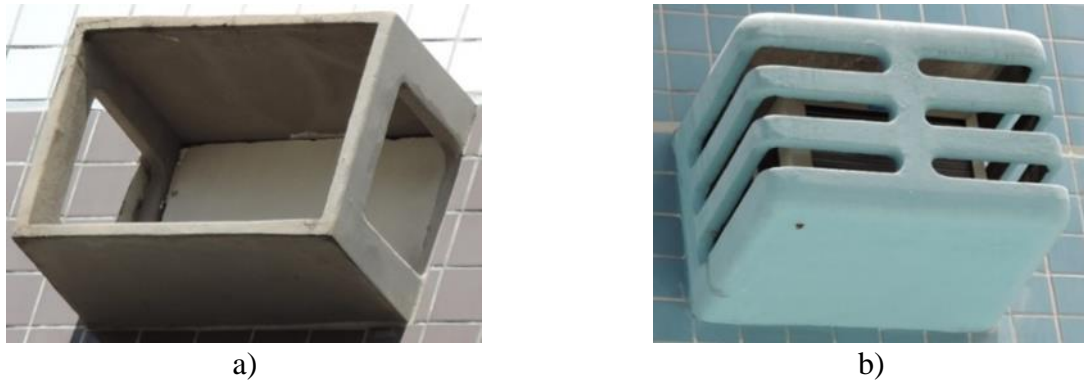
a)   b)

Figure 3. Reinforced concrete support, window type: a) open model; b) closed model.

c)   d)
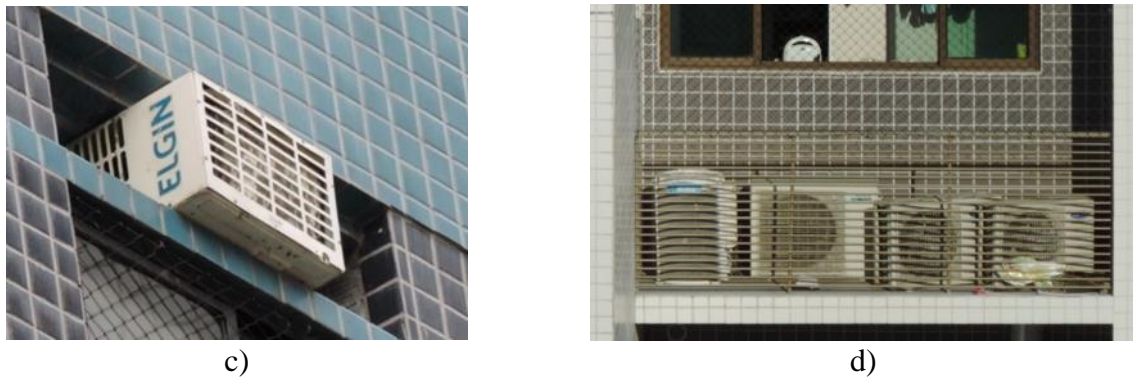
Figure 4. Other support models: c) hidden model; d) split model.

3.2. Structural design of window brackets

Below is the schematic representation of the open and closed models, Figure 5.

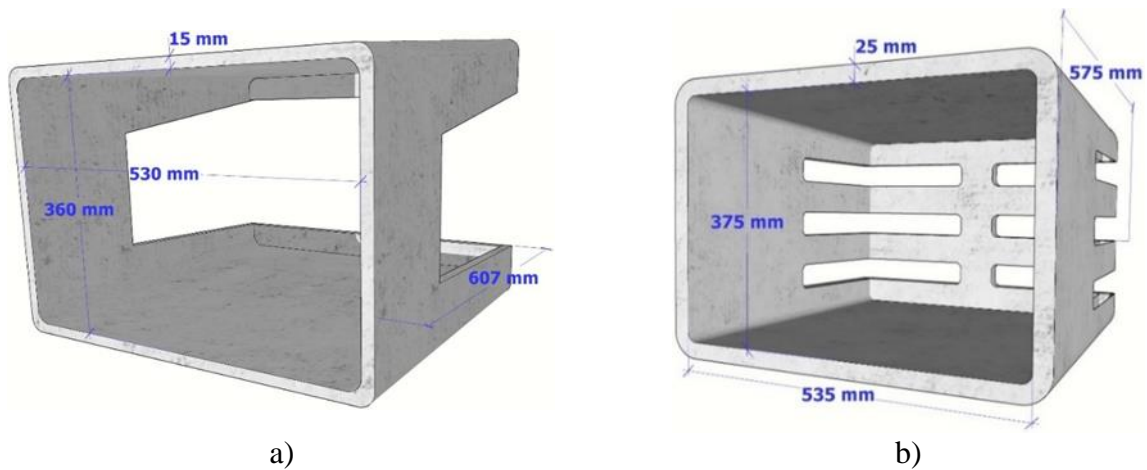a)   b)

Figure 5. Structure of window type templates: a) open; b) closed.

Because the dimensions of the open model are quite simple, the manufacturing becomes easier, but the fragility of the structural model becomes visible.

There is the detail of a section of this model, which will identify the position of the reinforcement, in bracket wall, which in this case uses the 4.2 mm CA-60 reinforcing bar, this consideration, as stated in ABNT NBR 7480: 2007. According to (Oswaldo and Helene, 2001), CA-60 steel has a higher corrosion resistance than CA-50 steel due to its higher carbon and manganese content, associated with lower internal stresses of the structure, detail section can be seen on Figure 6.
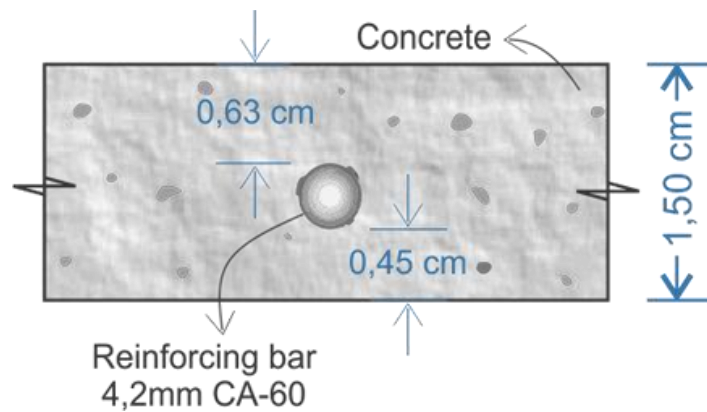
Figure 6. Reinforcing bar detail of open window model.

4. RESULTS AND DISCUSSION

4.1. Relative humidity / Atmospheric conditions

For this analysis it was collected through INMET - National Institute of Meteorology, Brazilian Climatological Normal 1981-2010 (INMET, 2018) and the city of Recife was separated during this period, based on the Relative Humidity Map of Compensated Air and the In two monthly and Annual Compensated Relative Air Humidity Spreadsheets, it was found that, based on the average, humidity ranged from 65% to 85% throughout the year, indicating humidity within the standards that accelerate corrosion processes, Figure 7.
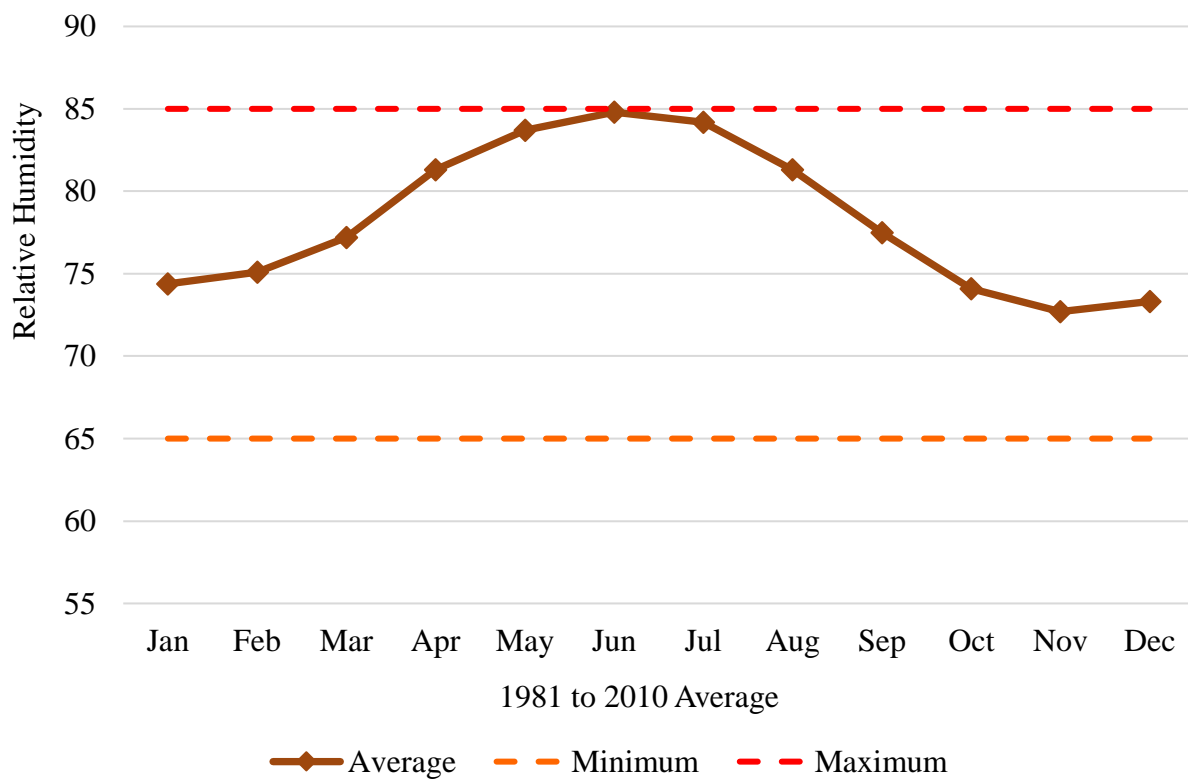

Figure 7. Relative humidity range (1981-2010), source: INMET.

According to the Brazilian Climatological Normal 1981-2010 (INMET, 2018), based on the Predominant Wind Direction Map (Cardinal and Collateral Points), there is a prevailing wind direction for the city of Recife, towards SE (southeast) in virtually every month of the year, except for November in the E (east) direction and July for the S (south) direction.

Using a residential building as an example, we used the Commander Compass Go 3.9.9 smartphone GPS app, using the gyro compass and the direction of the geographic coordinate inserted on the Google map, it was possible to visualize the direction of the windswept on the facades, year-round, Figure 8a.

This building has closed-model reinforced concrete protectors on all facades, but it can be seen that in the North (N) and West (W) facades, these structures tend to show more degradation, Figure 8b.

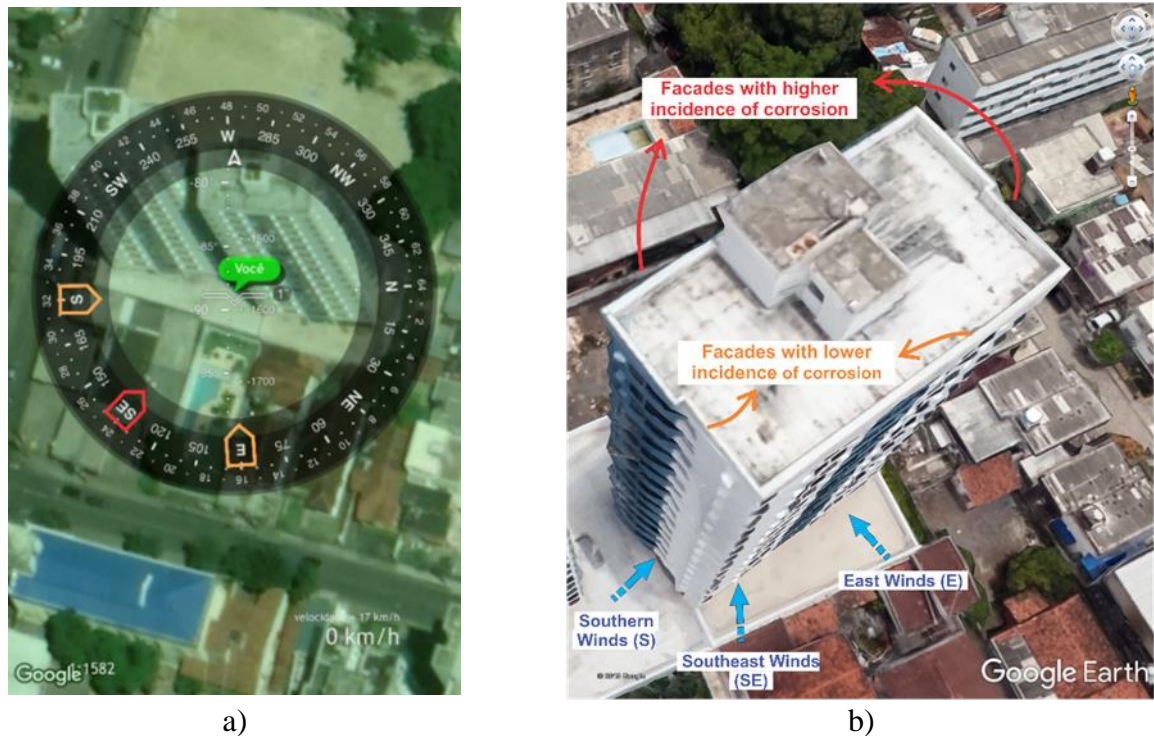a)   b)

Figure 8. Wind direction building: a) wind direction in the year; b) winds in the building.

Some studies indicate that the wind speed, being higher than 3m/s, can distribute the chloride ions to regions farther from the coast, being also influenced by the altitude, with a higher concentration of chloride ions at lower altitudes, up to 10m, but in some regions, such as Hawaii, in the USA, can reach up to 30m., There are drastic reduction of these saline materials, (Meira, 2017) above these altitudes even in places where sea waves break. It has been identified that the wind presents a more decisive factor in the transport of chlorides into the concrete than the altitude, (Balestra, 2019) and which is larger up to 100m from the coast (Moreno, et.al., 2018).

Based on data from the BDMEP - Teaching and Research Weather Database, INMET, Average Wind Speed (mps) (INMET, 2018), it can be seen that over 5 years, the wind speed in Recife has not exceeded 2.75m/s, as a location of milder winds, Figure 9.
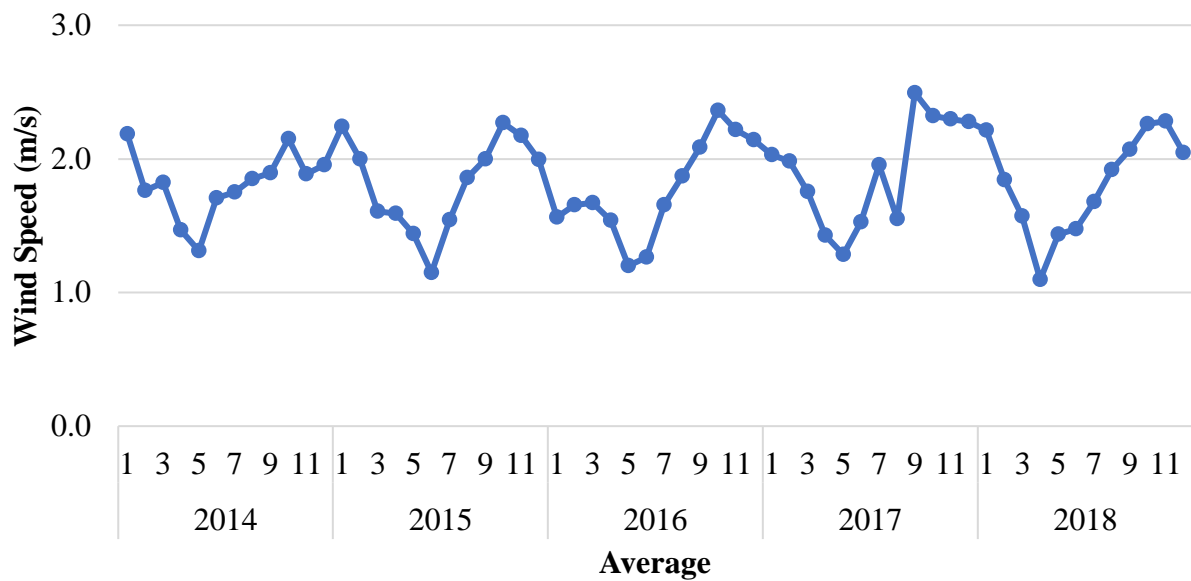
Figure 9. Wind speed (average), source: INMET.

4.2. Marine atmosphere

Because Recife is in a coastal region, close to the sea, the distance between the surveyed region and the breaking of the sea waves may indicate an attack of chloride ions (sea mist), Figure 10.
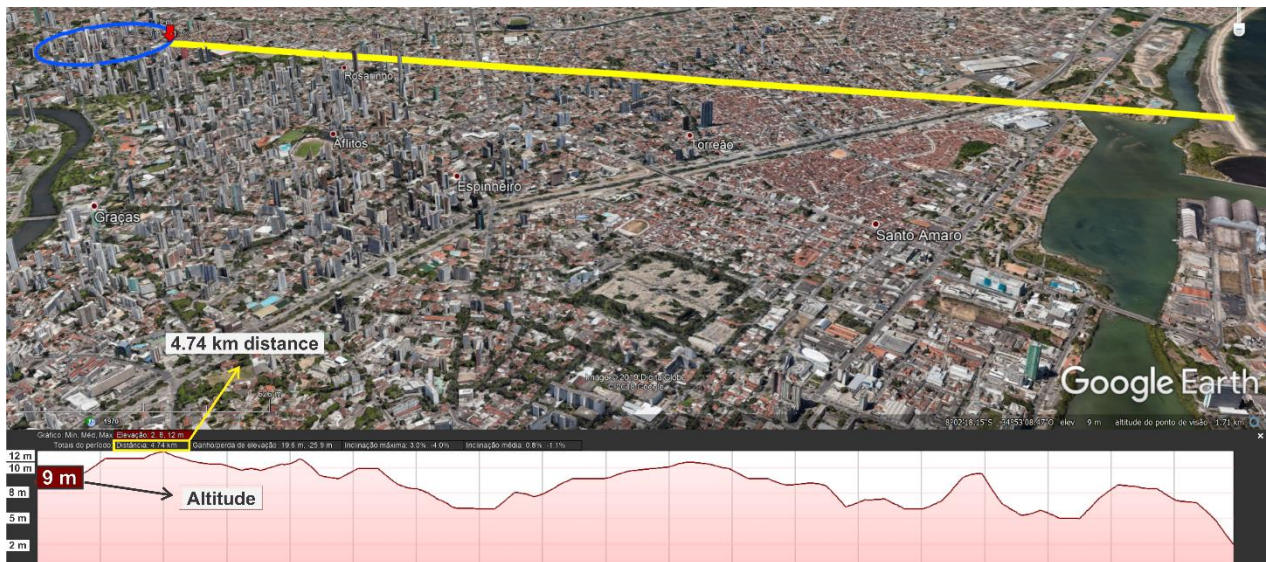

Figure 10. Distance from the analyzed region to the sea.

As can be seen, the distance from the breaking of the sea waves to the point under study, is around 4.74 km, according to (Pontes, 2006). After analyzing the seaside of the neighborhood of Boa Viagem in Recife, with measurements by the wet sail apparatus method for distances from 7 m to 320 m from the coast, where it was verified by an adopted model, that from 400 m there is a significant reduction in chloride deposition and boils down to tiny values at 700 m.

In another study by (Luna, 2008), on the Mapping of Atmospheric Corrosivity of the State of Ceará, it was concluded that this influence reaches distances of up to 30 km from the coast, that is, there are places with greater or lesser attack of chloride ions that can be very aggressive and with different morphologies (Moreno, et.al., 2015).

In a field analysis performed by (Meira, et.al., 2014), it was shown that the increase of concrete porosity, caused by the w/c ratio, causes a decrease in the amount of chloride ions inside the reinforced concrete.

4.3. Large population centers (pollution by aggressive agents)

The city of Recife concentrates a high population density, according to the 2010 Demographic Census of IBGE - Brazilian Institute of Geography and Statistics (IBGE, 2010), above 500 inhabitants per square kilometer, Figure 11, thus having one of the problems of the metropolises around the world: $PM_{2.5}$ fine particulate matter pollution, formed by airborne solid or liquid particles (Ventura, et.al., 2017).

This was found to be within the appropriate WHO - World Health Organization parameters, which would be up to 400 ppm of carbon dioxide in the open environment, probably because it is related to the coastal region meteorological system, favoring the dispersion of these particles by air, according to (Santos, et.al., 2014), and having only a higher concentration in the rainy season.
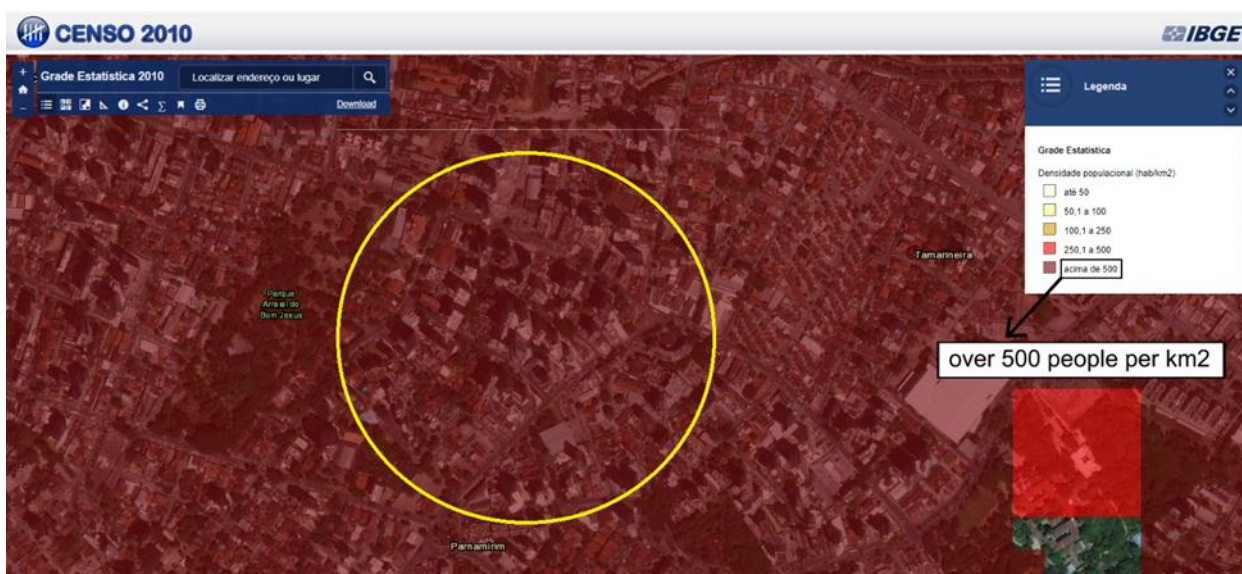

Figure11. Urbanization intensity, population density in Recife, PE.

5. IDENTIFICATION OF PATHOLOGICAL MANIFESTATIONS

After visiting cement artifact suppliers, it was found that the concrete traces were empirically performed, thus having no quality control over the water-cement ratio and consequently influencing the total void volume and pore size, facilitating the transport of water, chloride ions and CO_2 in concrete.

A field visit was carried out to identify the most recurrent pathological manifestations through a survey and recording through images and data.

In the first analysis, there is the visualization of cracks and reinforcement corrosion, possibly caused by carbonation or chloride attacks, Figure 12, as well as the most advanced state of degradation, when the structure stood out, due to the expansion caused by the volume increase of reinforcement and consequent expulsion of concrete by tensile force (Choi, et.al., 2014), Figure 13.

a) b)

Figure 12. Reinforcement corrosion in window type model: a) fissures; b) concrete detachment.

a) b)

Figure 13. Partial break in open window model: a) absence of lower slab; b) absence of upper slab.

Another point to highlight and no less aggravating, is the improper use of these supports, situations created by the users or refrigeration technicians who, due to lack of knowledge or inability, make use of these supports to make modifications with the addition of another cooling system, which generate undersized efforts, favoring the infiltrations in the façade, overloading the existing supports, already in the process of intense degradation, Figure 14.

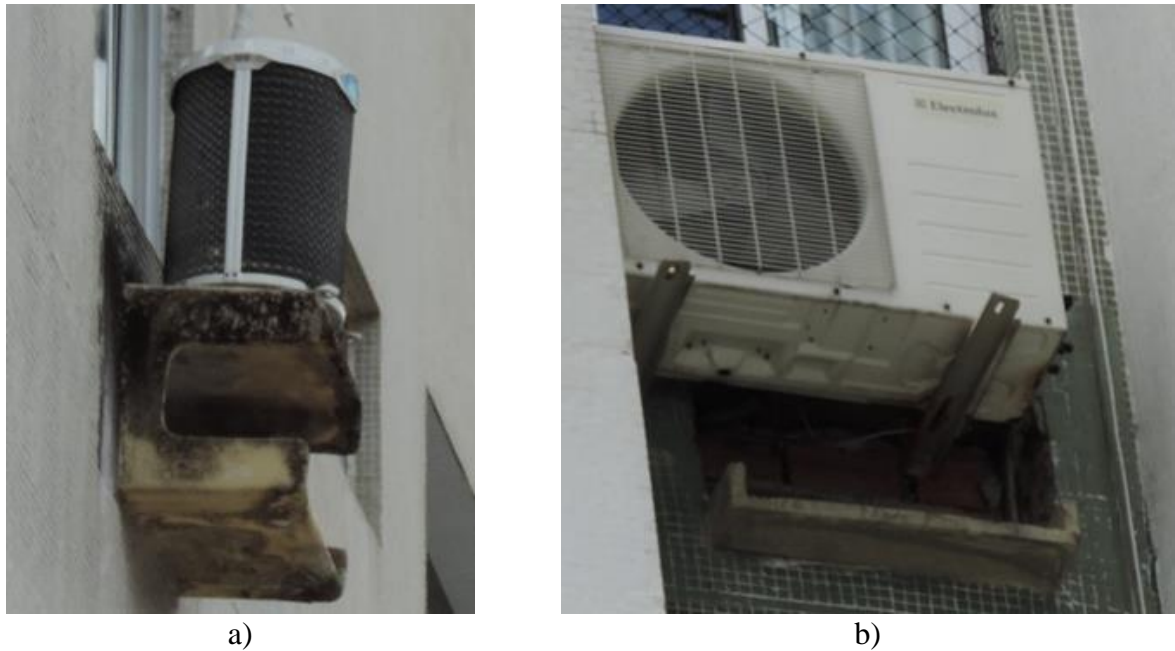a)   b)

Figure 14. Improper Use: a) non-dimensioned efforts; b) facade infiltration.

For the buildings that have reinforced concrete supports, the main pathological manifestations were visually identified in the field, such as: mold, efflorescence, reinforcement corrosion and concrete detachment, Figure 15. From the 29 surveyed buildings, 11 had a history of replacement of these supports, of which 9 already had recurrence of some pathological manifestations, including detachment of the concrete.
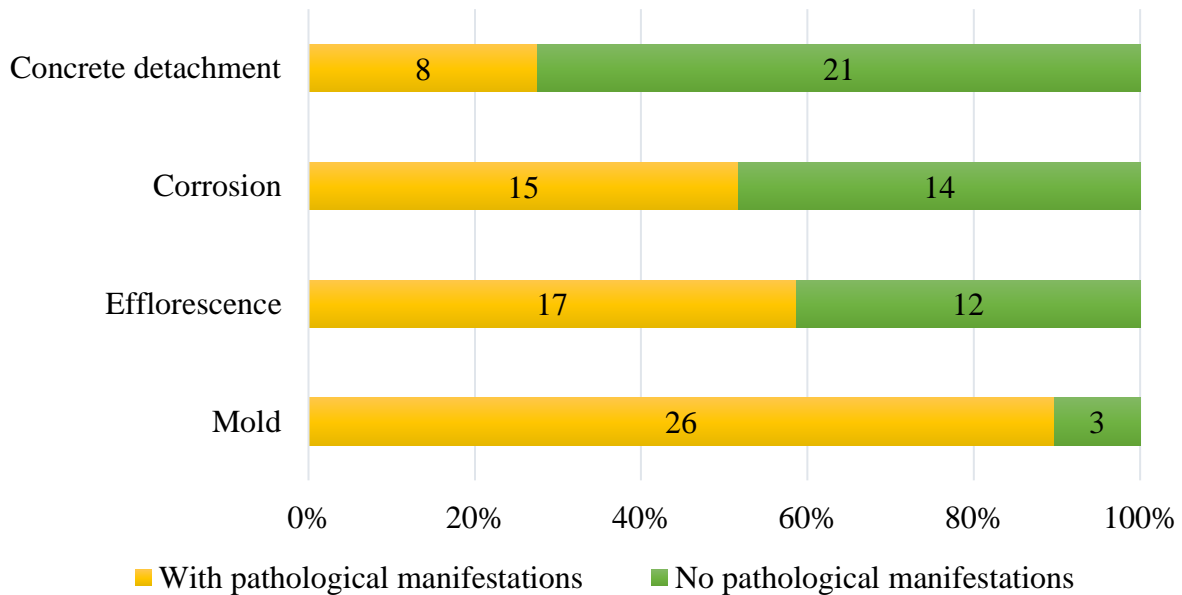

Figure 15. Pathological manifestations of reinforced concrete supports.

When analyzing closed-type models, their state of degradation is not easy to identify from the outside of the facades, since pathological manifestations tend to be more favorable on their internal face, leaving a margin of doubt as to their actual condition.

6. RISK ANALYSIS

After all the aggravating factors that accelerate the pathological manifestations, the questions inherent to the risk of this type of protector were analyzed, because in the face of the fragility generated by the degradations, the detachment of the façade (all or in part) may have a highly destructive impact in the soil.

Taking advantage of the calculation demonstrated by (Silveira, 2011), it was adopted for a 1kg object, considering the partial breakage of one support and another estimated weight of 25kg for a complete one, in a situation of detachment of the facades of the surveyed buildings and their respective heights.

Adopting Equation (1):

$$F = \frac{M.g.H}{D}$$ (1)

Which one has: F - force; M - body mass; g - acceleration of gravity; H - height; D - hardness of a concrete floor.

Figure 16 illustrates the information for the 1kg object in blue and 25kg in orange.
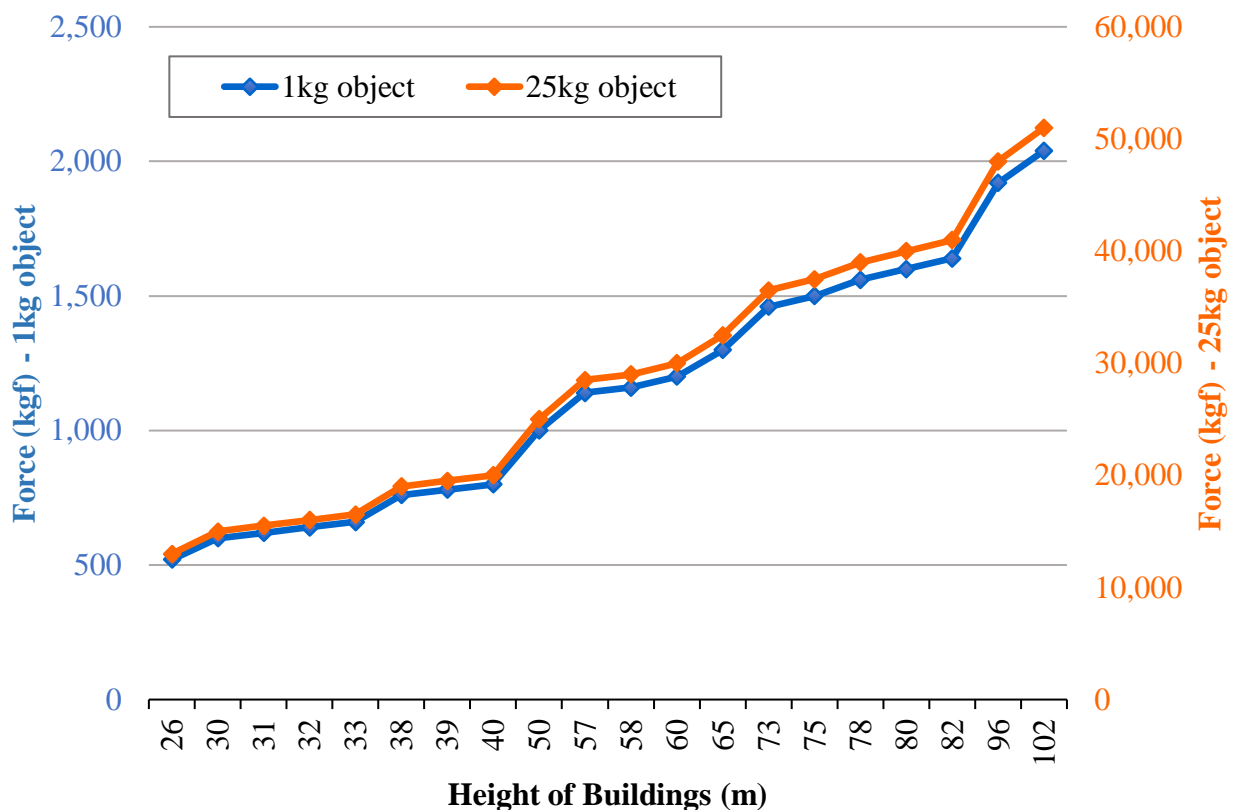

Figure 16. Force applied by the object in contact with the ground.

7. RECOVERY

This analysis aims to verify the viability of recovery of these supports, in order to increase their useful life, mainly related to the cases of corrosion of the reinforcement, since they have greater destructive power, not neglecting the other pathological manifestations of: mold, growth of vegetation, efflorescence, starting from the premise that resources will not be spent without a more robust justification, that is, there should be no maintenance of the facade just for cleaning and painting these supports.

For the recovery to be performed correctly, according to (Souza and Ripper, 1998), the need to remove the concrete that surrounds the reinforcement is considered, being considered thicknesses of 2 cm beyond the reinforcement, in order to ensure the total removal of the degraded concrete and return the reinforcement bars to alkaline condition, so that the cleaning and subsequent application of the grout are performed.

It is noteworthy that the wall thickness of the open model box prevents this execution, since the wall itself is only 1.5 cm thick, leaving this possibility of unfeasible recovery for the closed model box, although the dimensions are larger, neither allow a proper recovery, even if the condition is to remove only 1 cm from the concrete (without minimum standards and recommendations and with difficulty of execution), the possibility of cracking and breaking of the top are very large, because the structure itself is compromised, that is, in the case of this model, the possibility of recovery is also considered unfeasible, as shown in Figure 17.

It is noteworthy that in the market there are models with much more robust thicknesses of 4.5 cm to 6 cm of wall thickness, thus having a tighter control of concrete, these could be meeting the recommendations for greater durability.

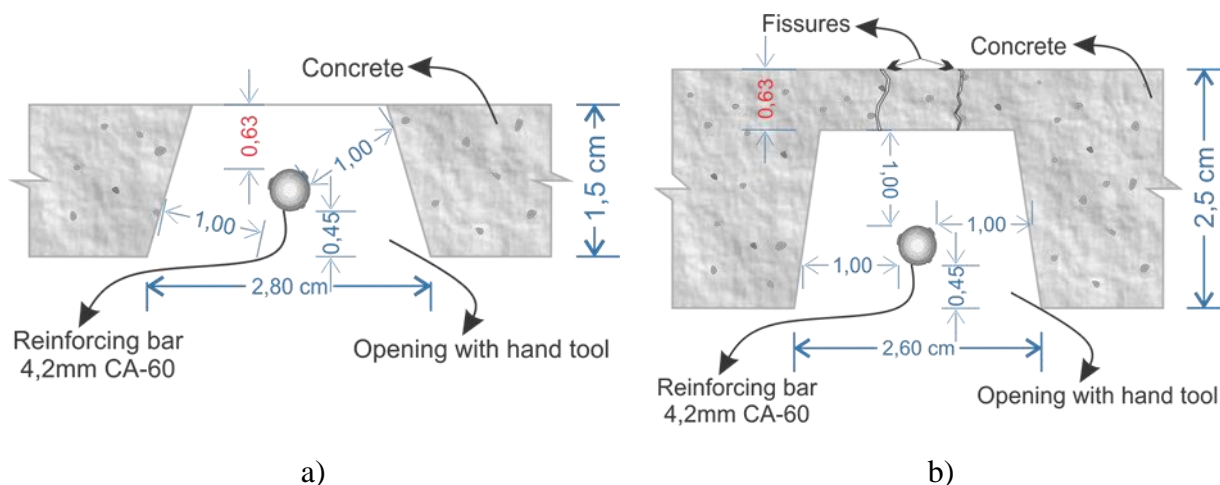a)   b)

Figure 17. Detail of possible recovery: a) open model; b) model closed

8. CONCLUSIONS

Considering what has been observed, it is understood that the number of buildings with reinforced concrete supports are high, around almost 50%, and that they present pathological manifestations in almost all.

Some factors were more impacting on the degradation aspects, such as the low concrete quality, the high humidity throughout the year and the low concrete coating, favoring the acceleration of carbonation, in the case of carbon dioxide, which was within acceptable standards. open environment.

390

The pathological manifestations and risks of the protectors of air conditioners in buildings
Silva, W. W., Monteiro, E. C. B.

Although the attack by chloride ions is quite aggressive, it proved to be non-contributory, since the distance to the sea is over 100 m and the winds below 3 m/s.

The most common pathological manifestations were: mold, efflorescence, reinforcement corrosion and concrete detachment, respectively.

Replacements of reinforced concrete supports were identified in 38% of buildings that use this model and that in the survey, 27% show signs of concrete detachment, this is a decisive factor, since the impact of objects at high heights may impact to the ground in the order of tonnes of force. Regarding the possibility of recovery, it was found that the supports do not offer the minimum acceptable repair conditions, as they do not have their own dimensions for such procedure.

9. ACKNOWLEDGEMENTS

10. REFERENCES

Almeida, F. C. R., Sales A. (2018), Ação do meio ambiente sobre as estruturas de concreto. In: Ribeiro D. V. et. al. *"Corrosão e degradação em estruturas de concreto: teoria, controle e técnicas de análise e intervenção"*. 2. ed. Elsevier, Rio de Janeiro, Brasil.

Associação Brasileira de Normas Técnicas (2007), *NBR 7480: Aço destinado a armaduras para estruturas de concreto armado - Especificação*. Rio de Janeiro, Brasil.

Associação Brasileira de Normas Técnicas (2014), *NBR 6118: Projeto de estruturas de concreto – Procedimento*. Rio de Janeiro, Brasil.

Balestra, C. E. T., et.al. (2019), *"Contribution for durability studies based on chloride profiles analysis of real marine structures in different marine aggressive zones"*. Construction and Building Materials 206:140–150. Elsevier. https://doi.org/10.1016/j.conbuildmat.2019.02.067

Bertolini, L. (2010), *"Materiais de construção: patologia, reabilitação e prevenção"*. Oficina de Textos, São Paulo, Brasil.

Fernández Cánovas, M. (1984), *"Patología y terapéutica del hormigón armado"*. Editorial Dossat, Madrid, España.

Choi, Y. S., et.al. (2014), *"Effect of corrosion method of the reinforcing bar on bond characteristics in reinforced concrete specimens"*. Construction and Building Materials 54:180–189. Elsevier. http://dx.doi.org/10.1016/j.conbuildmat.2013.12.065

Meira, G. R., et.al. (2014), *"Analysis of chloride threshold from laboratory and field experiments in marine atmosphere zone"*. Construction and Building Materials 55:289–298. Elsevier. http://dx.doi.org/10.1016/j.conbuildmat.2014.01.052

Meira, G. R., et.al. (2017), *"Vertical distribution of marine aerosol salinity in a Brazilian coastal area – The influence of wind speed and the impact on chloride accumulation into concrete"*. Construction and Building Materials 135:287–296. Elsevier. http://dx.doi.org/10.1016/j.conbuildmat.2016.12.181

Moreno, J. D., et.al. (2015), *"Determining corrosion levels in the reinforcement rebars of buildings in coastal areas. A case study in the Mediterranean coastline"*. Building Engineering 15:109–121. Elsevier. http://dx.doi.org/10.1016/j.conbuildmat.2015.09.059

Moreno, J. D., et.al. (2018), *"Exposure of RC building structures to the marine environment of the Valencia coast"*. Construction and Building Materials 100:11–21. Elsevier. https://doi.org/10.1016/j.jobe.2017.11.016

IBGE - Instituto Brasileiro de Geografia e Estatística (2018). *"Cidades e Estados: Recife (PE)"*. Brasília, Brasil. Disponível em: https://www.ibge.gov.br/cidades-e-estados/pe/recife.html. Acesso em: 13/06/2019.

IBGE - Instituto Brasileiro de Geografia e Estatística (2016). *"Cidades e Estados: Recife (PE)"*. Brasília, Brasil. Disponível em: https://www.ibge.gov.br/cidades-e-estados/pe/recife.html. Acesso em: 13/06/2019.

IBGE - Instituto Brasileiro de Geografia e Estatística (2010). *"Cidades e Estados: Recife (PE)"*. Brasília, Brasil. Disponível em: https://www.ibge.gov.br/cidades-e-estados/pe/recife.html. Acesso em: 13/06/2019.

IBGE - Instituto Brasileiro de Geografia e Estatística (2010). *"Censo Demográfico 2010, Grade Estatística 2010"*. Brasília, Brasil. Disponível em: http://mapasinterativos.ibge.gov.br/grade/default.html. Acesso em: 20/03/2019.

IBGE - Instituto Brasileiro de Geografia e Estatística (2002). *"Mapa de clima do Brasil 1:5 000 000"*. Brasília, Brasil. Disponível em: http://geoftp.ibge.gov.br/informacoes_ambientais/climatologia/mapas/brasil/Map_BR_clima_2002.pdf. Acesso em: 13/06/2019.

INMET - Instituto Nacional de Meteorologia (2018). *"Normais Climatológicas do Brasil (1981-2010) – Direção Predominante do Vento (Pontos cardeais e colaterais)"*. Brasília. Disponível em: http://www.inmet.gov.br/portal/index.php?r=clima/normaisclimatologicas. Acesso em: 18/06/2019.

INMET - Instituto Nacional de Meteorologia (2018). *"Normais Climatológicas do Brasil (1981-2010) – Umidade Relativa do Ar Compensada"*. Brasília. Disponível em: http://www.inmet.gov.br/portal/index.php?r=clima/normaisclimatologicas. Acesso em: 13/02/2019.

INMET - Instituto Nacional de Meteorologia (2018). *"BDMEP - Banco de Dados Meteorológicos para Ensino e Pesquisa - Série Histórica - Dados Mensais – Velocidade do Vento Média (mps)"*. Brasília. Disponível em: http://www.inmet.gov.br/portal/index.php?r=bdmep/bdmep. Acesso em: 24/06/2019.

Johnson, S. M. (1965), *"Deterioration, maintenance, and repair of structures"*. MCGraw-Hill, New York, USA.

Luna, A. M., et.al. (2008), *"Mapeamento da Corrosividade Atmosférica do Estado do Ceará"*. INTERCORR 2008. Recife, Brasil.

Cascudo, O., Helene P. R. L. (2001), *"Resistência à corrosão no concreto dos tipos de armaduras brasileiras para concreto armado"*. Boletim Técnico da Escola Politécnica da USP, Departamento de Engenharia de Construção Civil, EPUSP, São Paulo, Brasil.

Pontes, R. B. (2006), *"Disseminação de íons cloreto na orla marítima do Bairro de Boa Viagem, Recife/PE",* Dissertação Mestrado - Departamento de Engenharia Civil, Universidade Católica de Pernambuco, Recife, Brasil.

Santos, L. H. M., et.al. (2014), *"Analysis of atmospheric aerosol (PM$_{2.5}$) in Recife city, Brazil"*. Journal of the Air & Waste Management Association, 64:5, 519-528. https://doi.org/10.1080/10962247.2013.854282

Flores Larsena, S., Rengifob, L., Filippín, C. (2015), *"Double skin glazed fac, ades in sunny Mediterranean climates"*. Energy and Buildings 102:18–31. Elsevier. http://dx.doi.org/10.1016/j.enbuild.2015.05.019

Silveira, F. L. (2011), *"Qual o peso equivalente que uma pedra de massa igual a 1 kg chega ao solo, jogada do 6 andar de um edifício?"*. Centro de Referência para o Ensino de Física - CREF, UFRGS. 01 jun. 2011. Disponível em: https://www.if.ufrgs.br/novocref/?contact-pergunta=qual-o-peso-equivalente-que-uma-pedra-de-massa-igual-a-1-kg-chega-ao-solo-jogada-do-6-andar-de-um-edificio. Acesso em: 14 fev. 2019.

The pathological manifestations and risks of the protectors of air conditioners in buildings
Silva, W. W., Monteiro, E. C. B.

Souza, V. C., Ripper, T. (1998), *"Patologia, recuperação e reforço de estruturas de concreto"*. Pini, São Paulo, Brasil.

Perinia, K., Bazzocchib, F., Crocib, L., Maglioccoa, A., Cattaneo, E. (2017), *"The use of vertical greening systems to reduce the energy demand for air conditioning. Field monitoring in Mediterranean climate"*. Energy and Buildings 143:35–42. Elsevier. http://dx.doi.org/10.1016/j.enbuild.2017.03.036

Desai, V., Potter, R. (2014), *"The Companion to Development Studies"*. Routledge. Paignton. United Kingdom.

Ventura, L. M. B., et.al. (2017), *"Chemical composition of fine particles (PM2.5): water-soluble organic fraction and trace metals"*. Air Qual Atmos Health. Springer Science. http://dx.doi.org/10.1007/s11869-017-0474-z